

LA-UR-21-26450

Approved for public release; distribution is unlimited.

Title: COVID-19 Testing R&D Final Report

Author(s): Abergel, Rebecca J.; Adams, Parul; Antonopoulos, Dion; Babnigg, Gyorgy; Baker, Scott; Bedinger, Daniel; Borucki, Monica; Bradfute, Steven B.; Bunt, Thomas; Daum, Chris; Fitch, Joseph Patrick; Gerbasi, Vince; Gilna, Paul; Graham, David; Guarnieri, Michael; Hall, Sally; Hillson, Nathan; Hong-Geller, Elizabeth; Hura, Greg; Jaing, Crystal; Jha, Ramesh Kumar; et al.

Intended for: Report

Issued: 2021-07-08

Disclaimer:

Los Alamos National Laboratory, an affirmative action/equal opportunity employer, is operated by Triad National Security, LLC for the National Nuclear Security Administration of U.S. Department of Energy under contract 89233218CNA000001. By approving this article, the publisher recognizes that the U.S. Government retains nonexclusive, royalty-free license to publish or reproduce the published form of this contribution, or to allow others to do so, for U.S. Government purposes. Los Alamos National Laboratory requests that the publisher identify this article as work performed under the auspices of the U.S. Department of Energy. Los Alamos National Laboratory strongly supports academic freedom and a researcher's right to publish; as an institution, however, the Laboratory does not endorse the viewpoint of a publication or guarantee its technical correctness.

Department of Energy
National Virtual Biotechnology Laboratory
COVID-19 Testing R&D Final Report
July 6, 2021



Rebecca Abergel, LBNL	Greg Hura, LBNL	Lili Pasa-Tolic, PNNL
Paul Adams, LBNL	Crystal Jaing, LLNL	Christa Pennacchio, LBNL
Dion Antonopoulos, ANL	Ramesh Jha, LANL	Dave Rakestraw, LLNL
Gyorgy Babnigg, ANL	Andrzej Joachimiak, ANL	Scott Retterer, ORNL
Scott Baker, PNNL	Bishoy Kamel, LBNL	Marc Salit, SLAC
Daniel Bedinger, Carterra	Jeff Kimbrel, LLNL	Blake Simmons, LBNL
Monica Borucki, LLNL	Antionietta M. Lillo, LANL	Anup Singh, SNL, now LLNL
Steven B. Bradfute, UNM	Betty Mangadu, SNL	Jess Sustarich, SNL
Thomas Bunt, LLNL	Robert Meagher, SNL	James Thissen, LLNL
Chris Daum, LLNL	Joseph Moon, LLNL	Nileena Velappan, LANL
Pat Fitch, LANL, Team Lead	Nigel Mouncey, LBNL/JGI	Geoff Waldo, LANL
Vince Gerbasi, PNNL	Michael Morrison, LLNL	Kelly Williams, SNL
Paul Gilna, ORNL	Nisha Mulakken, LLNL	Jesse Wilson, PNNL
David Graham, ORNL	Hau Nguyen, LANL	Chunyan Ye, UNM
Michael Guarnieri, NREL	Marit Nilsen-Hamilton, Ames	Malin Young, PNNL
Sally Hall, LLNL	Kristin Omberg, PNNL	Yuko Yoshinaga, LBNL
Nathan Hillson, LBNL	Hugh O'Neal, ORNL	Mowei Zhou, PNNL
Elizabeth Hong-Geller, LANL	Jerry Parks, ORNL	

Research was supported by the DOE Office of Science through the National Virtual Biotechnology Laboratory, a consortium of DOE national laboratories focused on response to COVID-19, with funding provided by the Coronavirus CARES Act.



Ames	Ames Laboratory
ANL	Argonne National Laboratory
BNL	Brookhaven National Laboratory
LBL	Lawrence Berkeley National Laboratory
LLNL	Lawrence Livermore National Laboratory
LANL	Los Alamos National Laboratory

NREL	National Renewable Energy Laboratory
ORNL	Oak Ridge National Laboratory
PNNL	Pacific Northwest National Laboratory
SLAC	Stanford Linear Accelerator Center
SNL	Sandia National Laboratories

Cover Photo: Dan Judge via Los Alamos Science and Technology Magazine, 1963

Executive Summary

Eleven Labs within the US Department of Energy (DOE), National Virtual Biotechnology Laboratory (NVBL), came together as a team to address significant R&D gaps in COVID-19 testing. Beginning in March 2020, the NVBL COVID Testing Team developed an R&D agenda, worked with DOE and other agencies to set priorities, and collaborated to deliver timely results.

Priority was given to quick implementation as well as development of novel capabilities for immediate and evolving pandemic needs without placing additional burden on operational performers. Priority elements capitalized on DOE National Laboratory strengths and expertise. The Team delivered: testing and evaluation that enabled decisions on testing options, forward-leaning approaches to prepare for future scale-up needs, and models and experiments that supported prioritization of diagnostic and therapeutic candidates.

Highlights of the DOE NVBL COVID-19 Testing Team R&D include

- Collaborated with DoD, CDC, and FDA to provide experimental data that enabled national testing guidelines, assessed potential contamination in commercial kits, evaluated sample pooling approaches, examined viral transport media and protocols, and evaluated virus inactivation and extraction methods to assure test efficacy and safety for frontline health care workers. This R&D impacted millions of tests.
- Developed analysis tools to assess global evolution of the SARS-CoV-2 RNA genome, as it relates to nucleic acid-based assays. For example, an automatic *in silico* evaluation of diagnostic assays used around the world (<https://covid19.edgebioinformatics.org/#/home>) has been provided online for over a year.
- Identified distinguishing signatures in the SARS-CoV-2 RNA genome that can be used to rapidly detect this pathogen and other co-infecting pathogens in multiplexed assays. For example, this advance identified potentially significant relationships of co-infections with *Streptococcus pneumoniae* and *Streptococcus pyogenes* in positive COVID-19 samples; co-infections with other pathogens are being evaluated.
- Developed a small instrument to rapidly detect SARS-CoV-2 nucleic acid with high sensitivity. The Reveal-CoV instrument, which uses a one-step amplification process followed by heat inactivation and lysis, employs a colorimetric change for detection.
- Devised a “COVID Whistle” that incorporates sample collection media to simplify both collection of exhaled breath and extraction of virus. The device is being evaluated by a university collaborator.



The Testing Team and the NVBL were successful because of productive collaborations with multiple federal, state, and local governments, academia, and industry. We are proud of the contributions that we have made to COVID-19 pandemic response and would welcome the opportunity to continue contributing to our nation's preparedness and response to infectious diseases as well as broader opportunities to provide R&D and technology demonstrations that enable rapid response to future events.

Table of Contents

Executive Summary	3
Table of Tables	6
Table of Figures	6
Introduction	8
Task 1: Establish Alternative Instruments/Reagents and Reachback/Validation	10
1.1. Evaluation of Three Extraction Kits with a 2019-n-CoV Assay.....	10
1.2. Side-by-Side Evaluation of Abbott ID NOW and the CDC 2019-n-CoV Assay	12
1.3. Side-by-Side Evaluation of the ThermoFisher TaqPath COVID-19 Combo and the CDC 2019-n-CoV Assay	13
1.4. Testing assay efficacy of COVID-19 commercial kits.....	14
1.5. Testing clinical sample stability	14
1.6. Alternative virus inactivation protocols to enable diagnostic automation	15
1.7. Alternative RNA extraction technologies for commonly available extraction kits and instrumentation.....	16
1.8. Alternative RNA extraction technologies for saliva-based diagnostics.....	23
Task 2: Develop Affinity Reagents and Novel Platform Approaches	24
2.1 Objective	24
2.2 Diagnostic potential of antibodies	27
2.3 Conclusions	30
2.4 Supplementary information and graphics	31
Task 3: Droplet Digital Microfluidic Platforms for Detection of COVID-19	36
3.1 Disposable device	36
3.2 Current project status	36
Task 4: Integrated Data Science and Genomic-Guided Approaches	37
4.1 Integrated data science approach to support COVID selection and diagnosis	37
4.2 Using Genomics-guided approaches to improve testing effectiveness.....	39
Task 5: Structure-Based Protein Design for Diagnostics	43
5.1 Objective	43
5.2 Key findings	45
Task 6: Next-Generation Rapid Testing (Phase 2 – Next Gen Task 1)	56
6.1 Highlights	56
6.2 Inter-lab collaborations.....	56
6.3 Impacts and follow-on work	56
6.4 ORNL Breath Sampling “Whistle” (focus on Aim 1).....	57

6.5 LLNL Reveal-CoV instrument for point-of-care diagnostics (focus on Aim 2)	58
6.6 SNL stabilization of RT-LAMP reagents (Aim 2).....	60
6.7 ANL: Alternative molecular diagnostics and protein reagents (Aims 1 and 2).....	63
6.8 PNNL aptamer magnetic nanoparticle assay (Aims 1 and 2)	63
Manuscripts, Reports, and Presentations.....	67
Task 1: Establish Alternative Instruments/Reagents and Reachback/Validation.....	67
Task 2: Develop affinity reagents and novel platform approaches.....	67
Task 5: Structure-based protein design for diagnostics	67
Task 6: Next-Generation Rapid Testing (Phase 2 – Next Gen Task 1).....	69
Budget Summary	70

Table of Tables

Table 1. 1 Performance of the Norgen Biotek Total RNA Purification Kit, Bioneer AccuPrep Viral RNA Extraction Kit, Promega Maxwell HT Viral TNA Kit and Qiagen QIAamp Viral RNA Mini Kit.....	11
Table 1. 2 Points of failure for inactivation of SARS-CoV-2 by Norgen Buffer RL, Bioneer VB Buffer, Promega Lysis Buffer MC5018 and Qiagen Buffer AVL.....	12
Table 1. 3 Clinical samples from the California Department of Public Health.....	16
Table 1. 4 Mean synthetic SARS-CoV-2 and BCoV Ct increase.....	21
Table 1. 5 Mean clinical sample SARS-CoV-2 Ct increase.....	22
 Table 2S. 1 Affinity of all selected antibodies	34

Table of Figures

Figure 1. 1 Results of LANL study to test SARS-CoV2 in different VTMs and storage temperatures.....	15
Figure 1. 2 RT-qPCR of Bovine coronavirus extraction methods	18
Figure 1. 3 RT-qPCR of SARS-CoV-2 synthetic RNA buffer B extractions	19
Figure 1. 4 RT-qPCR of SARS-CoV-2 synthetic RNA magnetic bead extraction	19
Figure 1. 5 RT-qPCR of SARS-CoV-2 synthetic RNA Zymo column extraction	20
Figure 1. 6 N1 assay RT-qPCR of SARS-CoV-2 clinical samples	22
Figure 1. 7 N2 assay RT-qPCR of SARS-CoV-2 clinical samples	22
 Figure 2. 1 Selection of monoclonal antibodies by in vitro evolution of display libraries.....	25
Figure 2. 2 Affinity and specificity of selected antibodies.....	26
Figure 2. 3 Antibody epitope binning by surface plasmon resonance (SPR).....	27
Figure 2. 4 Limit of detection of trimeric spike by whole SARS-CoV 2.	28
Figure 2. 5 Antibody interference with binding SARS-CoV 2 spike protein's receptor-binding domain (RBD2) to ACE2.	29
Figure 2. 6 Antibody neutralization of SARS-CoV2 infection HEK cells	30
 Figure 2S. 1 Sequences of unique antibodies derived from all selections.....	32
Figure 2S. 2 Kinetic data	32
Figure 2S. 3 Affinity variations depending on antibody format	33
Figure 2S. 4 Specificity of IgG interactions	33

Figure 2S. 5 Epitope binning by sandwich ELISA.....	35
Figure 3. 1 Disposable digital microfluidic device (DMF)	36
Figure 4. 1 Residues in drug binding pocket of interest in protein Nsp5 and corresponding amino acid counts in GISAID sequences for Nsp5.	38
Figure 4. 2 Microarray probes distributed across the SARS-CoV2 genome, reference sequence NC_045512.2) shown using Integrative Genomics Viewer (IGV) from the Broad Institute	39
Figure 5. 1 mAbs' flexibility and how this flexibility affects the assembly of multiple mAbs	46
Figure 5. 2 Chemical diagrams of possible oxidation states of a cysteine sidechain.....	48
Figure 5. 3 Binding inhibitors to PLpro.....	49
Figure 5. 4 Binding of Tipiracil to Nsp15.....	50
Figure 5. 5 RNA stabilized Nsp7/8/12 complex.....	51
Figure 5. 6 Methylation of the 2'-O-ribose of the m7GpppA catalyzed by Nsp10/16 from SARS-CoV-2.....	52
Figure 5. 7 Probability of aligned pairs of residues	53
Figure 5. 8 ACE2 derived peptide redesigned for stability and binding affinity	54
Figure 5. 9 Clustering of conformational macrostates of the simulated peptides in a transformed space obtained from variational approaches for Markovian processes (VAMP).....	55
Figure 6. 1 3D CAD rendering of the 'whistle'	57
Figure 6. 2 Lattice structures of printed hydrogels	57
Figure 6. 3 Laboratory testing using an atomizer was initiated to visualize flow and particle capture was initiated and is still underway..	58
Figure 6. 4 Reveal-CoV instrument development..	59
Figure 6. 5 Reveal-CoV test parameter development..	60
Figure 6. 6 Storage of lyophilized reagents for one month	62
Figure 6. 7 Mechanism behind aptamer-functionalized MNP capture of SARS-CoV-2	64
Figure 6. 8 Schematic describing theory behind colorimetric detection assay	65

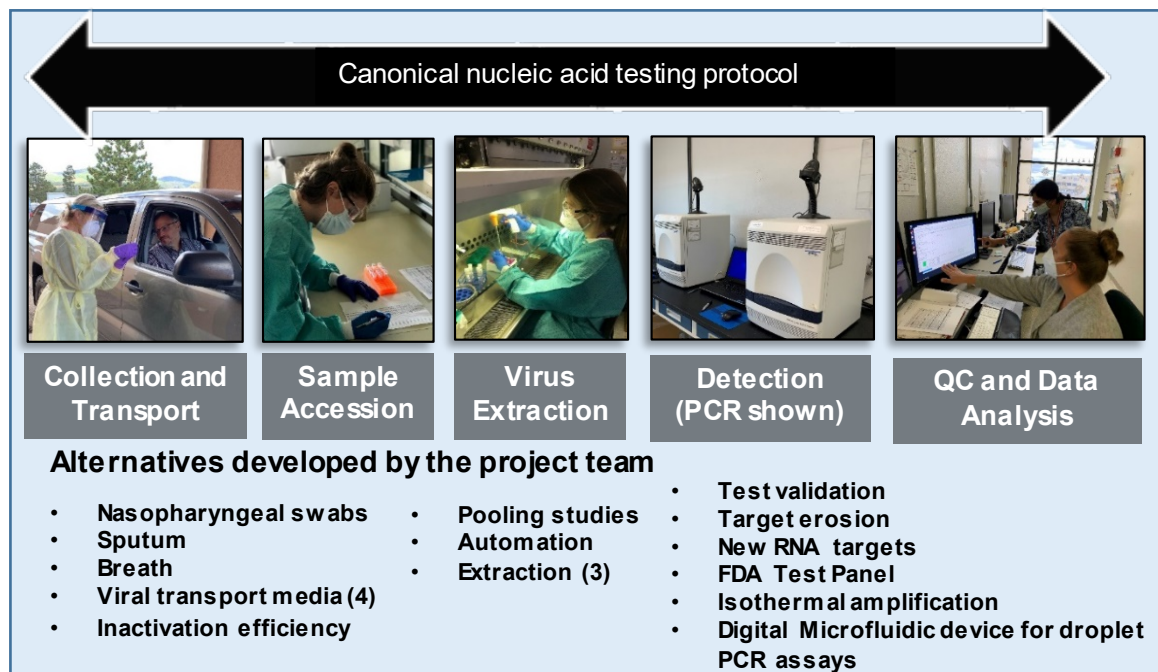
Introduction

The Department of Energy (DOE) National Virtual Biotechnology Laboratory (NVBL) has proven to be an exceptionally effective contributor to the nation's COVID response, quickly marshaling unique national laboratory expertise and capabilities to meet critical needs. For example, the NVBL supported manufacturers to address key shortages in medical supply chains, creating nearly 1,000 new medical manufacturing jobs. Working closely with other federal agencies and state and regional decision-makers, the NVBL provided solutions across a range of COVID challenges. These accomplishments demonstrate the game-changing resource represented by DOE's 17 national laboratories working together within the integrated NVBL framework. Going forward, the NVBL can bring these resources to bear on future national and international needs and emergencies.

In March and April 2020 as part of the NVBL, eight laboratories (ANL, LBNL, LLNL, LANL, ORNL, PNNL, SNL, and SLAC) and two user facilities (EMSL—Environmental Molecular Sciences Laboratory and JGI—Joint Genome Institute) came together and jointly submitted to DOE a concept paper "Scientific data to enhance situational awareness and decision making."

Since its beginning, the NVBL COVID-19 Testing Team has benefited from close connections with operational testing. In March 2020, two critical collaborations were launched with 1) DOE Labs standing-up and conducting operational tests and 2) a subcommittee of the Diagnostic Task Force that included the Centers for Disease Control and Prevention (CDC), Food and Drug Administration (FDA), and Department of Defense (DoD). The DOE Office of Science arranged our connection with the Task Force through the Federal Emergency Management Administration (FEMA) chair. The subcommittee was initially chaired by DoD.

By the end of the first week in April 2020, DOE had approved a project and account codes were open at several labs. At the end of May 2020, the NVBL COVID-19 Testing Team with ten Labs responded to a DOE request with a proposed Phase 2 for the project. The project goals, now accomplishments, are summarized in the below figure together with a canonical test protocol.



The funded tasks integrated across both investment Phases are reported in six projectTasks:

1. Establish alternative instruments/reagents (Phase 1) and reachback/validation (Phase 2);
2. Develop affinity reagents and novel platform approaches;
3. Droplet digital microfluidic platform;
4. Integrated data science (Phase 1) and genomic-guided approaches (Phase 2); and
5. Structure-based protein design for diagnostics.
6. Next-generation rapid testing (Phase 2 – Next Gen Task 1)

The NVBL COVID-19 Testing Team is proud of our contributions. These are summarized in the Task sections as well as a publication and presentation section. At several different times the Team has captured potential next phases for Testing and provided to DOE and other Agencies.

Task 1: Establish Alternative Instruments/Reagents and Reachback/Validation

Institutions: LBNL, ANL, LLNL, ORNL, PNNL, SNL, LANL

Rebecca Abergel, Gyorgy Babnigg, Crystal Jaing, Thomas Bunt, David Graham, Elizabeth Hong-Geller, Kristin Omberg

Phase 1 of this task addressed the need to provide validated alternatives to the instruments and reagents used for the currently approved diagnostics. The main goal of this task was to normalize sample testing across available RNA extraction kits, instrumentation, and other high impact test protocols using a common RNA standard across the labs.

Phase 2 of this task addressed the need to continue reach-back and validation capabilities to support priorities of the FDA, CDC, and DoD representatives of the national (HHS/FEMA) Task Force on Diagnostics. The Task performed analysis of clinical sample stability and alternatives to RNA extraction methods, RT-PCR assays, and other test protocols compared to the CDC-approved diagnostics that were in use at the time.

1.1. Evaluation of Three Extraction Kits with a 2019-n-CoV Assay

The COVID-19 pandemic and associated increase in clinical testing produced a sharp rise in demand for RNA extraction kits. Laboratories reported issues receiving extraction kits in a timely manner, resulting in subsequent delays in test results. To help alleviate these issues, PNNL assisted the HHS/FEMA COVID-19 Diagnostics Task Force by evaluating the following characteristics of three RNA extraction kits (the Norgen Biotek Total RNA Purification Kit; Bioneer AccuPrep Viral RNA Extraction Kit; and Promega Maxwell HT Viral TNA Kit) identified by the Task Force:

- Limits of detection for quantitative synthetic RNA using the Centers for Disease Control and Prevention's (CDC) 2019-Novel Coronavirus (2019-nCoV) Real-Time RT-PCR Diagnostic Panel and the Applied Biosystems 7500 Fast Dx system;
- Limits of detection for positive clinical specimen using the Centers for Disease Control and Prevention's (CDC) 2019-Novel Coronavirus (2019-nCoV) Real-Time RT-PCR Diagnostic Panel and the Applied Biosystems 7500 Fast Dx system; and
- Ability to inactivate the virus as measured by a cell-based infectivity assay.

The three kits evaluated were selected by the Diagnostics Task Force based on commercial availability. The QIAGEN QIAamp Viral RNA Mini Kit, which was already approved for use with the CDC 2019-nCoV assay, was used as reference. All kits were run using the manufacturer's instructions.

To evaluate limits of detection, first, quantitative synthetic RNA from SARS-Related Coronavirus 2 was spiked into a diluent consisting of a suspension of human A549 cells and viral transport medium (VTM).¹ The limit of detection of the CDC assay was evaluated by performing 20 extraction replicates using each kit.

¹ VTM was prepared using the Center for Disease Control and Prevention Standard Operating Procedure, "Preparation of Viral Transport Medium," #DSR-052-03.

Next, positive clinical specimen was diluted to concentrations that approximated the Ct values obtained with synthetic RNA at 3, 1 and (estimated) 0.3 genome copies per microliter. The limit of detection of the CDC assay was evaluated by performing 20 extraction replicates with each kit.

To evaluate inactivation efficiency, the lysis buffers from each kit were mixed with SARS-CoV-2 USA-WA1/2020 at various ratios in serum-free media. Suspensions were incubated at room temperature for 10 minutes then added to confluent Vero cell (ATCC CCL-81) monolayers in 96-well plates. The monolayers were incubated at 37°C for four days then scored for cell death by microscopic observation.

A summary of the limit of detection for each kit with clinical specimen is shown in **Table 1.1**.

Table 1.1 Performance of the Norgen Biotek Total RNA Purification Kit (#17200), Bioneer AccuPrep Viral RNA Extraction Kit (#K-3033), Promega Maxwell HT Viral TNA Kit (#AX2340) and Qiagen QIAamp Viral RNA Mini Kit (#52906) at approximately 0.3 copy, 1 copies and 3 copies per microliter of virus in positive clinical specimen.

Kit	Concentration copies/ μ L	Positive Replicates / Total Replicates	N1 Avg Ct SD		N2 Avg Ct SD	
Norgen	0.3	20/20	35.8	1.0	36.4	0.7
Bioneer	0.3	18/20	36.4	1.0	36.6	0.7
Promega	0.3	20/20	32.0	1.2	31.4	2.1
Qiagen*	0.3	24/24	33.7	1.9	34.4	2.2
Norgen	1	20/20	31.9	1.3	32.2	0.6
Bioneer	1	20/20	34.5	0.8	35.2	0.6
Promega	1	20/20	31.8	0.6	31.5	0.3
Qiagen*	1	24/24	31.7	1.1	32.7	1.2
Norgen	3	20/20	32.3	0.8	33.3	0.4
Bioneer	3	20/20	33.0	0.4	33.8	0.4
Promega	3	20/20	30.0	0.6	30.2	0.5
Qiagen*	3	24/24	30.6	0.9	31.7	2.5

*Results shown are the average and standard deviation of eight replicates performed on three separate days

All four lysis buffers inactivated SARS-CoV-2 USA-WA1/2020 at the concentrations recommended in the kit instructions. All four demonstrated similar patterns of cytopathic effect (CPE) at high concentrations of lysis buffer followed by decreasing CPE at lower concentrations, followed by a return of CPE at the point of failure where virus was no longer inactivated. A summary of the point of failure for each of the buffers is presented in **Table 1.2**.

Table 1.2 Points of failure for inactivation of SARS-CoV-2 by Norgen Buffer RL, Bioneer VB Buffer, Promega Lysis Buffer MC5018 and Qiagen Buffer AVL.

Manufacturer	Point of failure Virus : Buffer	Kit Instructions Sample : Buffer	Fold-increase of Buffer Above Point of Failure
Norgen	2 : 1	100 uL : 350 uL (1 : 3.5)	7
Bioneer	1 : 1	200 uL : 300 uL (1 : 1.5)*	1.5*
Promega	2 : 1	200 uL : 200 uL (1 : 1)	2
Qiagen	2 : 1	140 uL : 560 uL (1 : 4)	8

*Only lysis buffer was tested in this experiment. The Bioneer kit instructions include a 60°C 10-minute incubation which was not performed and could change the results.

Based on the results of the PNNL experiments, the FDA listed two additional kits (<https://www.fda.gov/medical-devices/coronavirus-covid-19-and-medical-devices/faqs-testing-sars-cov-2>) as options that labs can consider using in the fight against COVID-19, boosting the supply of chemicals and supplies linked to a critical step in the testing process.

Final Report: K.M. Omberg, H. Engelmann, J. Hutchison, A. Melville, K. Oxford and K. Victry, “Evaluation of Three Extraction Kits with a 2019-n-CoV Assay,” PNNL-30085, June 2020.

1.2. Side-by-Side Evaluation of Abbott ID NOW and the CDC 2019-n-CoV Assay

On May 14, 2020, the FDA issued an alert due to “early data that suggest potential inaccurate results from using the Abbott ID NOW point-of-care test to diagnose COVID-19. Specifically, the test may return false negative results.” To assist the FDA in making decisions about the Abbott ID NOW, PNNL verified the performance of the Abbott ID NOW COVID-19 assay in comparison to the CDC 2019-nCoV assay. The Abbott ID NOW COVID-19 assay targets a unique region of the ORF1ab/RdRp gene. The CDC assay targets two regions of the N gene. The performance of the two assays had not previously been compared.

Two positive specimens in viral transport media (VTM) were obtained from the Washington State Department of Health. The specimens were previously analyzed using the CDC assay and determined to be positive with Ct values <24 for N1 and N2. In conversations with Abbott, Abbott’s technical support indicated that the presence of VTM in the specimens should not impact results.

This evaluation was performed over two separate days. One day prior to each evaluation day, a specimen was thawed and the concentration of virus in the specimen was estimated using the CDC 2019 n-CoV panel with BEI Resources’ Quantitative Synthetic RNA as the reference. On the day of the experiment, the specimen was serially diluted to working concentrations based on the concentrations calculated from the prior day’s PCR results. Each working concentration suspension was vortexed and split into two tubes. One split was used to perform 20 replicates of the Abbott ID NOW test (10 replicates on each of 2 instruments). The other split was used to perform between 3 and 20 replicates of the CDC assay.

For the Abbott ID NOW test, the suspension was vortexed and 5 uL of suspension was spiked into 2.5 mL Abbott elution buffer. Results were recorded and the process was repeated for a total of 20 replicates at each concentration.

The final suspensions had approximately 312.5 (Abbott 1X LOD), 625 (Abbott 2X LOD), 1250 (Abbott 4X) and 2500 (Abbott 8X LOD) genome copies in 5 µL.

For the CDC assay, the suspension was vortexed and 5 µL of suspension was spiked into a vial containing 3 mL VTM. Each vial was treated as one specimen for analysis by the CDC assay. 20 replicates of the CDC assay were performed at each concentration.

Results indicated that the Abbott ID NOW assay was less sensitive than the CDC assay. In parallel with this study, FDA developed a live virus reference panel that was provided to all 2019-n-CoV diagnostic test manufacturers. The results provided by Abbott and CDC similarly indicated an approximately twofold difference in sensitivity. Based on an aggregate set of data that included PNNL's, Abbott submitted a request to amend its Emergency Use Authorization to indicate that the test is approved only for specimens collected "from individuals who are suspected of COVID-19 by their healthcare provider within the first seven days of the onset of symptoms." Specimens collected within the first seven days of symptoms typically contain larger concentrations of virus than those collected pre-symptomatically or at later times. The revision of the labelling was intended to mitigate the sensitivity issues observed by restricting the use of the tests to specimens with presumed high concentrations of virus.

1.3. Side-by-Side Evaluation of the ThermoFisher TaqPath COVID-19 Combo and the CDC 2019-n-CoV Assay

The PNNL Medical Test Site (PNNL-MTS) routinely performs the CDC assay using the IDT 2019-nCoV CDC qPCR Probe Assay (#10006606, #0000510344) with the ThermoFisher TaqPath™ 1-Step RT-qPCR Master Mix, CG (#A15299) on the Applied Biosystems 7500 Fast Dx. The PNNL-MTS verified the performance characteristics of the CDC assay using Quantitative Synthetic RNA from SARS-Related Coronavirus 2 (BEI Resources, NR-52358) and successfully reproduced CDC's limit of detection data as reported in CDC-006-00019, Revision: 03, effective 03/30/2020. The CDC reports that the limit of detection (LOD) of their assay with the Qiagen Viral RNA Mini Kit is 1 RNA copy per microliter. The CDC assay targets two regions of the N gene.

PNNL was interested in verifying the ThermoFisher TaqPath COVID-19 Combo kit, which is currently used by LLNL. The ThermoFisher assay's reported LOD is slightly higher than the CDC's. In addition, concerns have been raised about potential erosion of performance of the ThermoFisher assay because it targets both the N, ORF1ab and S genes; mutations of the S gene have been observed in recent variants.

To compare limits of detection for the CDC and ThermoFisher assays, first, quantitative synthetic RNA from SARS-Related Coronavirus 2 was spiked into a diluent consisting of a suspension of human A549 cells and viral transport medium (VTM).² The limit of detection of each assay was evaluated by performing 20 extraction replicates using each kit. PNNL confirmed that the manufacturers' reported LODs are correct; that is, the ThermoFisher assay does have an LOD of 10 RNA copies per reaction, which is about twice the LOD of the CDC assay.

² VTM was prepared using the Center for Disease Control and Prevention Standard Operating Procedure, "Preparation of Viral Transport Medium," #DSR-052-03.

To compare limits of detection with recent variants, PNNL sequenced positive clinical specimens obtained between January 1, 2021 and March 31, 2021 from PNNL employees and released for research. The sequences of these samples indicate the presence of the B.1.1.7 variant of SARS-CoV-2, first detected in California. However, none of the specimens contained variants with S gene mutations that might impact assay performance.

1.4. Testing assay efficacy of COVID-19 commercial kits

Together with PNNL, LANL tested a specific commercial kit for diagnostic assay efficacy. Our initial results seemed to indicate that the kit was not working correctly. Negative controls using just plain water as the test substance yielded a positive COVID-19 signal with the RT-PCR assay across 10 different lot numbers. It was unclear at the time what might be causing the false positive tests. We speculated that there might be contamination in the kits, and the positive control used in the kits may have been inadvertently packaged with the other kit components during manufacturing and thus yielded false positive signals. To determine whether this scenario could be an explanation, the Genomics Team at LANL sequenced the false positive amplicon products from the RT-PCR reaction to look at their genetic sequence. It turned out that there were genetic sequences in the false positive amplicons that exactly matched the positive control sequences included in the kit, suggesting that our hypothesis of contamination was likely the case. Based on these results, the decision was made to pull the diagnostic kits from national distribution. This work was essential to preventing millions of contaminated COVID-19 tests from being distributed across the US, that could potentially have led to false positive diagnoses and greater distrust in US testing capabilities at a particularly sensitive time early in the pandemic.

1.5. Testing clinical sample stability

At the beginning of the pandemic, there were many questions on how to keep clinical samples stable and ensure viral stability prior to Lab Testing. Back in April 2020, there were supply chain issues for all materials and supplies needed for Lab Testing, including Viral Transport Medium or VTM. We performed evaluations of several different VTMs, including a commercially-available VTM, basic buffers such as phosphate-buffered saline (PBS), and a VTM recipe made with components available in a standard research lab, to see if there was a difference in VTMs for sample stability. We performed systematic studies using positive clinical nasopharyngeal (NP) samples acquired from the New Mexico Department of Health and determined that NP samples were stable and were detected at the same levels using any of the VTMs tested, including the basic buffers. (See **Figure 1.1**) This was particularly useful information for the Task Force since a basic buffer such as PBS is cheap and easy to acquire, so there was no need for diagnostic labs to use hard-to-find or expensive VTMs for sample storage, if supply chain proved to be an issue.

Our team also tested sample storage at different temperatures as another stability parameter. At the time, the Task Force was looking at the possibility of self-sampling with NP swabs during the summer months if there continued to be extremely long lines and wait times at testing facilities across the nation. If individuals self-sampled and then left their sample in a hot car for several days, how would that affect reliability of sample stability? Our team performed systematic experiments to test clinical sample stability at different temperatures across a range

between -80°C to +37°C (human body temperature). Surprisingly, the efficiency of virus detection in samples incubated for 3 days was similar across the entire temperature range. (See **Figure 1.1**) We had speculated that virus at 37°C for 3 days might have undergone degradation and would no longer be detectable. However, our results indicated that samples left in a hot car for 3 days would likely be just as accurate compared to storage at room temperature or in the refrigerator. These analyses provided the Task Force with a valuable risk assessment of clinical sample handling and accuracy of diagnostic testing. Self-swabbing combined with mail-in testing became an option for the public at local pharmacies last year.

- 4 VTMs
- 6 temps (-80, -20, 4, 25, 30, 37°C)
- Starting material Ct ~30 – clinical sample
- 1:5 dilution with VTM for 72 hrs
- Added T=0 sample
- CDC-approved assay

Maybe of note:

- VTM1: 25°C

Conclusions:

- Incubation at higher temperatures (30, 37) do not seem to affect assay
- Not much difference between the temperatures
- Not much difference between VTMs. Note #1-3 all have FBS, gentamicin and amphotericin

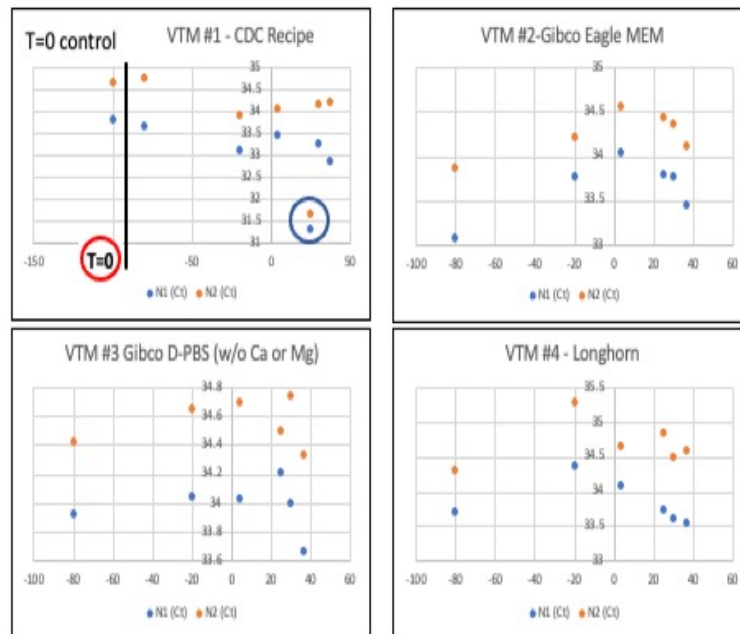


Figure 1.1 Results of LANL study to test SARS-CoV2 in different VTMs and storage temperatures.

In addition to the two examples described above, the LANL team also led studies for the Task Force on: (1) Sample pooling strategies to combine individual samples for testing in communities with low prevalence of disease to save reagents and labor; (2) Saliva studies using spiked samples to look at heterogeneity of assay efficacy in a small population; and (3) Limit of detection (LOD) studies of a heat-inactivated SARS-CoV-2 standard for the FDA. These multiple efforts provided government agency stakeholders with the data and information they needed to make timely decisions and offer validated Lab Testing guidance to the diagnostic community.

1.6. Alternative virus inactivation protocols to enable diagnostic automation

During Phase 1 testing activities, LBNL tested alternative virus inactivation protocols to enable automation methods for both RNA extraction and RT-qPCR analysis, to ultimately accelerate the testing process. Two virus inactivation tests were initiated under BSL-3 protocols (PNNL): (i) to

evaluate the potency of DNA/RNA shield (Zymo research) at inactivating viral samples prior to RNA extraction and (ii) to demonstrate inactivation by Proteinase K in both nasal fluids and saliva samples (UC Berkeley Tjian-Darzacq protocols). Each step was part of a different protocol that has been evaluated for reproducibility, stability, and subsequent automation. The Zymo DNA/RNA shield inactivation buffer had been implemented in testing standard operating protocols for surveillance at UC Berkeley in April 2020 and the methods was transferred to LBNL after inactivation efficiency was confirmed for safe handling under BSL-2 conditions. Automation Processes and LIMS protocols were developed for the following steps: (i) virus inactivation (Hamilton Microlab STARlet liquid handlers); (ii) RNA extraction and purification (KingFisher Flex); (iii) RT-qPCR dispensing and readout (Hamilton Vantage and 7500 Fast Dx RT-qPCR), and were implemented in the LBNL newly-established Berkeley Lab Automated Diagnostics Extension (BLADE) facility.

1.7. Alternative RNA extraction technologies for commonly available extraction kits and instrumentation

Testing supply manufacturers have struggled to keep up with demand, leading to shortages of commercially available RNA extraction reagents. We have identified four potential alternate RNA extraction methods comprised of readily available reagents and materials. These methods produce extraction yields that range in comparability with reagents currently authorized for use in testing, with the most promising method producing statistically equivalent PCR Ct values to the Emergency Use Authorized (EUA) Qiagen Viral RNA extraction kit.

1.7.1 Sample Preparation

Alternative RNA extraction methods were tested on simulated clinical samples containing a surrogate virus or synthetic RNA. These artificial samples were created using human nasal cavity swabs (Lee Biosolutions, Maryland Heights, MO) mixed with Viral Transport Media (VTM) (Teknova, Hollister, CA). The frozen nasal cavity swab was added to 3 ml of VTM and used fresh. Bovine coronavirus (BCoV), Mebus (NR-445) (provided by M. Borucki, LLNL) or SARS-CoV-2 synthetic RNA encapsulated in phage protein (Microbiologics, St. Cloud, MN) was then added to the nasal sample and VTM background. Additionally, RNA extraction performance was evaluated for five clinical samples supplied by the California Department of Public Health (CDPH). The samples had been previously confirmed as positive or negative for SARS-CoV-2. Of the five samples, four were confirmed by the CDPH as positive with N gene and Orflab RT-qPCR assays (**Table 1.3**).

Table 1.3. Clinical samples from the California Department of Public Health. CDPH Ct values were determined by RT-qPCR of N gene and Orflab regions tested at CDPH.

Sample Name	Specimen Source	Date Collected	CDPH Result	Mean CDPH Ct Value
LLNL_166	NP Swab	8/21/20	Positive	14.0
LLNL_167	NP Swab	8/21/20	Positive	22.0
LLNL_168	NP Swab	8/24/20	Positive	30.9
LLNL_169	NP Swab	8/24/20	Positive	36.4
LLNL_170	NP Swab	8/25/20	Negative	Not Detected

1.7.2. RNA Extraction

Extractions were carried out in triplicate using 140 µl of simulated clinical sample for each extraction method. Control extractions were performed using the Qiagen Viral RNA extraction kit, with the addition of RNA carrier as described by the manufacturer and eluted in 60 µl of elution buffer. For CDPH clinical samples, both the control and alternative RNA extractions were performed using 100 µl of sample as input and eluted in 100 µl.

Alternate methods for RNA isolation were carried out in two stages, lysis and PCR inhibition removal. Two lysis buffers were used:

- Lysis Buffer A (2 M guanidinium thiocyanate, 80 mM DTT, 25 mM sodium citrate, 20 µg/ml glycogen, pH 6.9) (He et al., 2017)
- Lysis buffer B (25 mM DTT, 1.25 mM sodium citrate, pH of 6.8)

Buffers were combined with either a magnetic bead-based or column-based clean-up procedure, for a total of four potential alternative RNA isolation methods. One of the two lysis buffers were added to each sample followed by incubation for 10 minutes:

- Buffer A was incubated at 65°C
- Buffer B was incubated at 80°C.

Heat-lysed samples were purified with one of two methods:

- 1.8X Beckman Coulter RNA Clean magnetic beads (Beckman Coulter, Pasadena, CA) and eluted in 100 µl of nuclease-free water
- Zymo RNA Clean and Concentrator 25 columns (Zymo Research, Irvine, CA), and eluted in 50 µl of nuclease-free water.

1.7.3 BCoV RT-qPCR Amplification

Bovine coronavirus RT-qPCR amplifications were run for each sample using 1X TaqPath 1-Step RT-qPCR Master Mix reagents (Life Sciences Corporation, Grand Island, NY) and custom primers and probes targeting the BCoV Mebus polymerase gene as previously described (Borucki et al, 2013). The assay contained 250 nM probe (/56-FAM/CCGTGTTAG/ZEN/GATGGTATGGCATACTCCAGTG/3IABkFQ/) and 500 nM of forward and reverse primers (5'-CCATGTGTCATGCATTGGATT-3' and 5'-CACCGATCATCCTGACAATCA-3'). Standard curves were generated by amplifying 10-fold serial dilutions of 10⁹ to 10² copies of synthetic Mebus bovine coronavirus Polymerase gene. 5 µl of extracted RNA samples were added to each RT-qPCR reaction in a final reaction volume of 20 µl.

1.7.4. SARS-CoV-2 RT-qPCR Amplification

Synthetic and clinical SARS-CoV-2 amplifications were run for each sample as described in the CDC 2019-nCoV CDC EUA published protocol. 1X TaqPath 1-Step RT-qPCR Master Mix reagents and SARS-CoV-2 (2019-nCoV) CDC qPCR Probe Assay primers and probes (Integrated DNA Technologies, Coralville, IA) were used for the N1, N2 and RP assays. For SARS-CoV-2 synthetic RNA extractions, standard curves were generated for the N1 and N2 assays by adding 10⁷ to 10² copies of SARS-CoV-2 N gene synthetic RNA (Microbiologics, St. Cloud, MN) diluted 10-fold, serially. Human RNase P positive DNA controls, Hs_RPP30 Positive Control (Integrated DNA Technologies, Coralville, IA), were included in each RP assay.

Only the N1 and N2 assays were performed for RNA extracted from CDPH clinical samples. These assays were not run with standard curves, but with 10^7 copies of synthetic SARS-CoV-2 RNA as positive controls. RNA volumes were normalized to the Qiagen extraction elution volume and 5 μ l was added to each 20 μ l PCR reaction. No template controls were included with each assay. RT-qPCR reactions for all samples, standards curves and controls were performed in triplicate.

Reverse transcriptase quantitative PCR was performed on an ABI fast 7500 Real Time System with the following parameters: 2-minute hold at 25°C, 15-minute hold at 50°C, 2 minute hold at 95°C, and 45 cycles of 95°C for 15 seconds followed by 55°C for 30 seconds.

1.7.5. Bovine Coronavirus and Synthetic SARS-CoV-2 RNA Samples

Two lysis buffers and two purification methods were tested as four total extraction comparisons against the Qiagen Viral RNA extraction method. The RNA extraction efficiencies of these four methods were evaluated by comparing the differences of the average cycle threshold (Ct) values between each procedure and the Qiagen extraction method.

For the extractions of the Mebus virus, a single RT-qPCR assay amplifying the Mebus coronavirus Polymerase gene was run using each of the four alternate extraction methods.

Figure 1.2 shows the average of these Ct values for the Buffer A and B lysis buffers, in combination with the magnetic bead and Zymo column purifications. The Qiagen standard extraction produced a mean Ct of 15.9 ± 0.3 , while the Buffer A yielded a mean Ct of 17.5 ± 0.1 and 16.9 ± 0.5 when purified by magnetic bead or column. Buffer B produced a Ct value of 17.8 ± 0.1 for the magnetic bead purification and produced the highest average extraction efficiency at a Ct of 16.0 ± 0.2 using column purification.

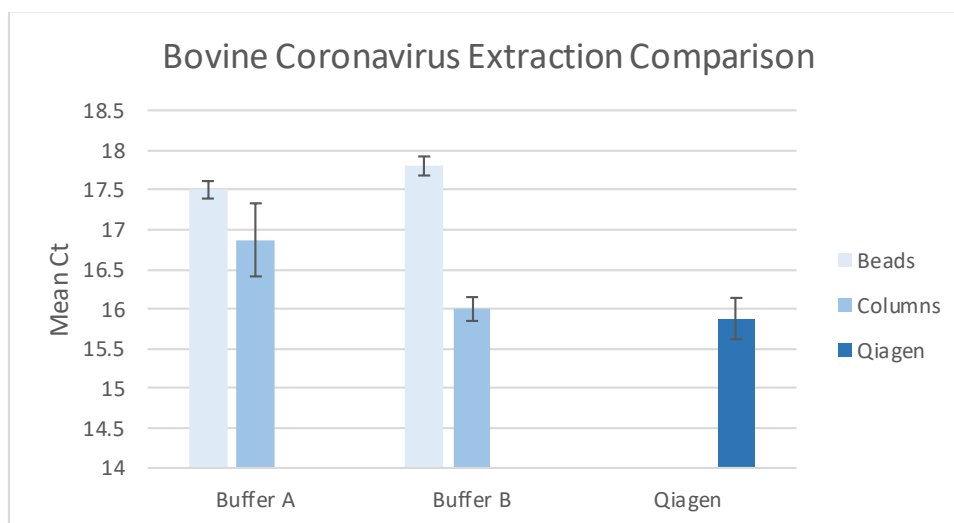


Figure 1.2. RT-qPCR of Bovine coronavirus extraction methods

The synthetic SARS-CoV-2 RNA sample extractions were evaluated by amplification of the N1 and N2 regions, which target the SARS-CoV-2 nucleocapsid (N) gene, and by amplification of the RP assay, which is used as an RNA extraction control in clinical sample testing and maps to human RNase P. Buffer A lysis amplified the N1 and N2 assays at Ct values of 29.6 ± 0.4 to 30.6

± 0.2 for bead and column purification, whereas Qiagen amplified at 28.7 ± 0.4 to 29.0 ± 0.4 (Fig. 1.3).

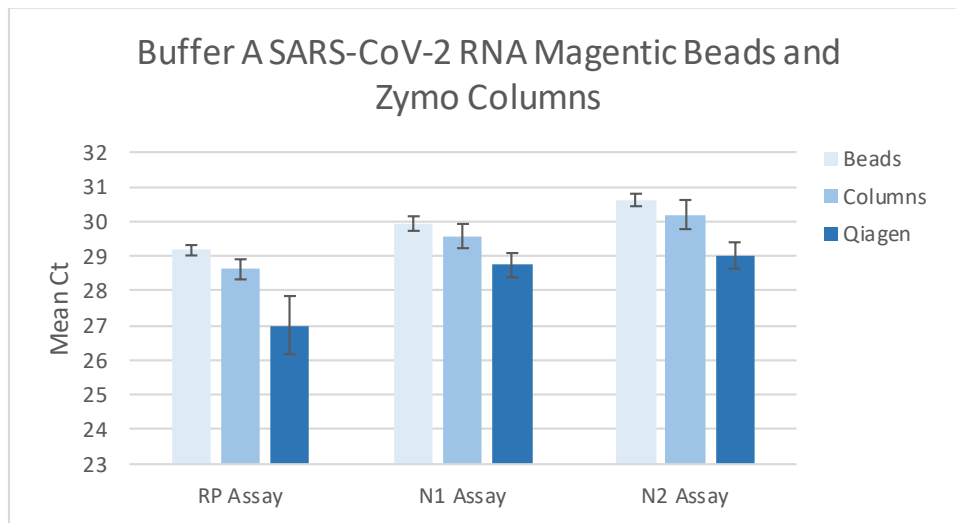


Figure 1.3. RT-qPCR of SARS-CoV-2 synthetic RNA buffer B extractions

When purified via magnetic beads, Buffer B produced average Ct values of 27.5 ± 0.1 and 29.1 ± 0.3 for the N1 and N2 assays, while the Qiagen extractions amplified at 26.9 ± 0.2 and 28.4 ± 0.1 Cts (Fig. 1.4). For lysis followed by Zymo column clean up, the N1 and N2 average Cts were at 28.8 ± 0.2 and 30.3 ± 0.3 , compared with the Qiagen amplification of 28.6 ± 0.1 and 29.9 ± 0.2 (Fig. 1.5).

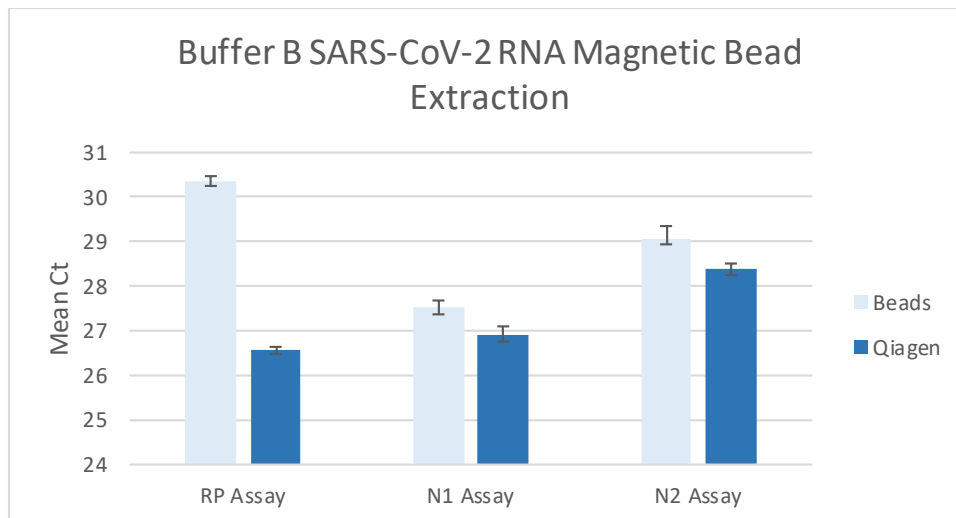


Figure 1.4. RT-qPCR of SARS-CoV-2 synthetic RNA magnetic bead extraction

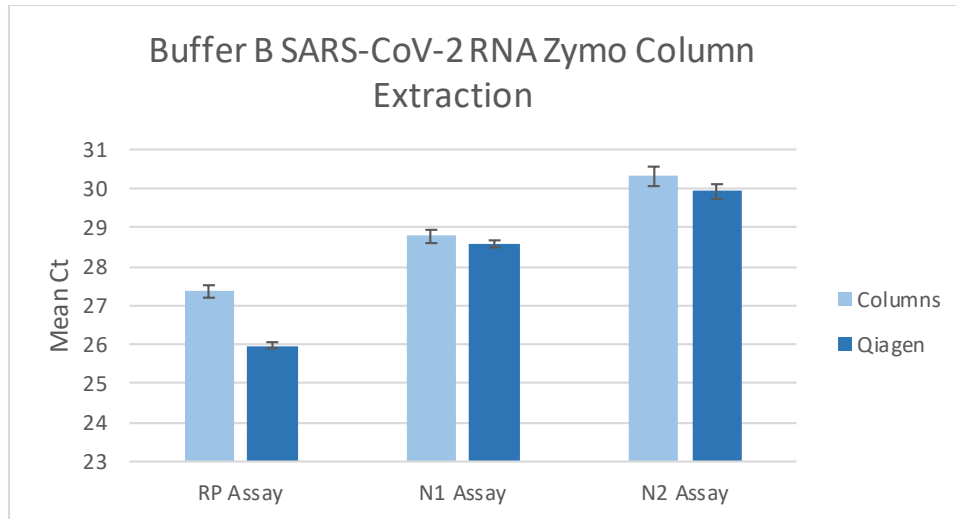


Figure 1.5. RT-qPCR of SARS-CoV-2 synthetic RNA Zymo column extraction

Each alternate extraction method average Ct value was compared to the Qiagen extraction method average Ct value. These comparisons are presented as mean Ct differences in Table 1. The alternate extractions yielded efficiencies that were dependent upon the template used, as well as on the RT-qPCR assay amplified. The first method which comprised of a Buffer A lysis followed by a magnetic bead clean up, yielded the lowest average extraction efficiency for the N1 and N2 assays as compared to the Qiagen standard kit, giving mean Ct differences of 1.2 and 1.6 (**Table 1.4**). However, for both the SARS-CoV-2 RP assay and for the bovine coronavirus RNA extraction, the most significant Ct change was seen with Buffer B lysis and bead clean up, with delta Ct values of 1.9 and 3.8. Interestingly, the N1 and N2 assays for this method had smaller Ct delays of 0.6 and 0.7, on average. Buffer A purified by column yielded an average amplification that was 1.0 Cts later for the bovine coronavirus assay and between 0.8 and 1.6 Cts later for the SARS-CoV-2 synthetic RNA. As with the Buffer B/Bead extraction, the SARS-CoV-2 N1 and N2 assays aligned more closely with the Qiagen extraction, with 0.8 and 1.2 Ct value delays, respectively.

Overall, all four of the RNA extraction methods performed better for the N1 and N2 assays as compared with the RP assay. The highest extraction efficiency overall gave a mean delta Ct of just 0.1 ($p=.24$). This was accomplished through extraction of the bovine virus using Buffer B and column purification. Indeed, extraction of SARS-CoV-2 RNA with this combination yielded Ct values closest to the Qiagen for the RP, N1 and N2 assays as well.

Table 1.4. Mean synthetic SARS-CoV-2 and BCoV Ct increase.

Buffer A			Buffer B	
RT-qPCR Assay	Beads	Column	Beads	Column
RP	2.2 ***	1.6 ***	3.8 ***	1.4 ***
N1	1.2 ***	0.8 ***	0.6 ***	0.2 *
N2	1.6 ***	1.2 ***	0.7 ***	0.4 **
BCoV	1.6***	1.0 ***	1.9 ***	0.1 ($p=.24$)
Overall Mean Ct Change	1.7 \pm 0.4	1.1 \pm 0.4	1.8 \pm 1.5	0.5 \pm 0.6

Mean increase in synthetic SARS-CoV-2 and Bovine coronavirus alternative extraction RT-qPCR Ct values compared to Qiagen extraction. Two tailed Welch's t-test

*significant at $p < .05$,

**significant at $p < .005$

***significant at $p < .001$

1.7.6. SARS-CoV-2 Clinical Samples

The Buffer B paired with a Zymo column clean up produced extraction yields which most closely resembled the Qiagen extractions for both the Mebus virus surrogate as well as for the simulated SARS-CoV-2 samples. This combination was used as the sole alternate extraction method tested with clinical samples. Five SARS-CoV-2 clinical samples, which were previously tested by the CDPH and ranged in Ct values of 14 to not detected after 40 cycles, were evaluated with the alternate extraction and Qiagen extraction methods. These sample represented the high, medium, low, and very low levels of viral RNA which may be present in clinical samples.

The negative CDPH sample, LLNL_170, was not detected using with the Buffer B/Zymo nor with the Qiagen extraction methods in the N1 or N2 assay. Sample LLNL_169, with an original CDPH average Ct of 36.4 was not detected with N1 or N2 assays following extraction with BufferB/Zymo. However, this sample yielded a mean Ct value of 35.3 ± 1.54 for the N1 assay and a single replicate amplification of Ct 36.6 for the N2 assay when extracted with the Qiagen kit. Furthermore, LLNL_169 was only detected in one of the three RT-qPCR replicates within two of the three Qiagen RNA extraction replicates, demonstrating how this level of virus within a sample may only be detected intermittently. Samples LLNL_166, LLNL_167, and LLNL_168 amplified with Ct values ranging from 13.8 ± 0.2 to 32.5 ± 0.3 for the N1 and N2 assays following extraction by Qiagen. When extracted using Buffer B/Zymo column, they amplified at Ct values of 13.9 ± 0.3 to 33.4 ± 1.4 (**Fig. 1.6** and **1.7**). The mean Ct differences between the alternate method and Qiagen for the sample with the highest level of detected virus were 0.1 and 0.4 for the N1 and N2 assays. As the CDPH Ct values within the clinical samples increased, the mean Ct delay for the alternate method increased (**Table 1.5**). This relationship between increased Ct delay as a factor of increased Ct value may reflect how RNA extraction efficiency declines with lower levels of viral RNA input.

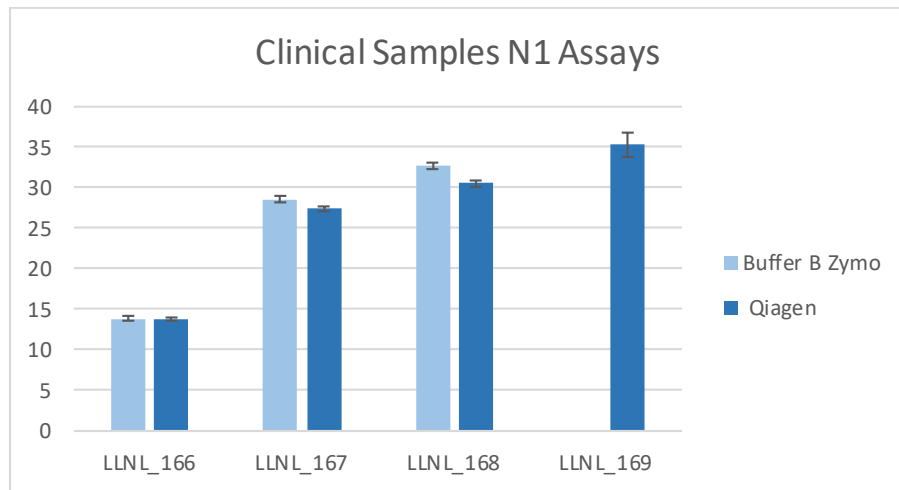


Figure 1.6. N1 assay RT-qPCR of SARS-CoV-2 clinical samples

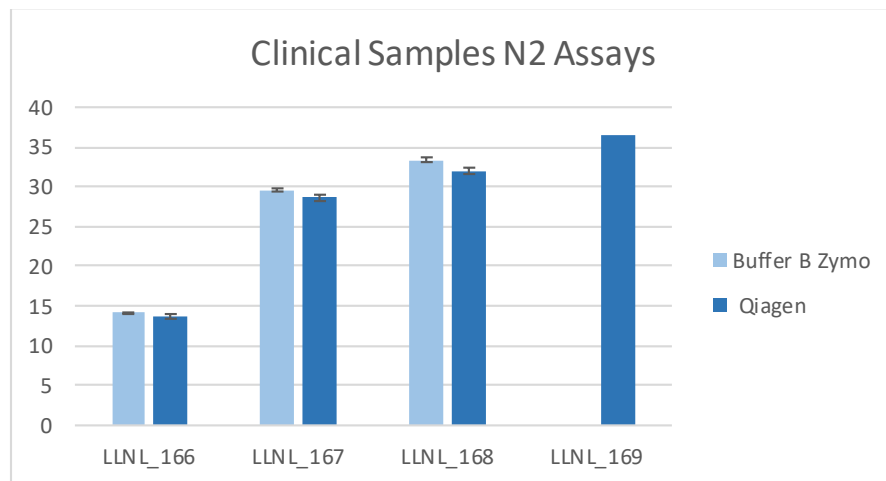


Figure 1.7. N2 assay RT-qPCR of SARS-CoV-2 clinical samples

Table 1.5. Mean clinical sample SARS-CoV-2 Ct increase.

CDPH Sample	Sample Virus Level	N1 Assay Mean Ct Delay	N2 Assay Mean Ct Delay
LLNL_166	High	0.1 ($p=.49$)	0.4**
LLNL_167	Medium	1.2***	1.0***
LLNL_168	Low	2.2***	1.4***
LLNL_169	Very Low	Not Detected	Not Detected
LLNL_170	Negative	Not Detected	Not Detected

Mean increase in SARS-CoV-2 clinical sample alternative extraction RT-qPCR Ct values compared to Qiagen extraction. Two tailed Welch's t-test

*significant at $p<.05$

**significant at $p<.005$

***significant at $p<.001$

In this project, we evaluated two lysing buffers and two PCR clean up methods as alternate RNA extraction protocols for SARS-CoV-2 detection by PCR as these reagents do not depend on commercially available kits, alleviating the dependency on kits when reagents are in shortage. The two lysing buffers can be made in a laboratory using standard reagents. The two clean up methods are not part of any extraction kits and can be purchased separately. We compared the extraction efficiency against the EUA Qiagen viral RNA extraction kit using bovine coronavirus, synthetic SARS-CoV-2 and archived clinical samples from the CDPH. Our results showed that lysing Buffer B (25 mM DTT, 1.25 mM sodium citrate, pH of 6.8) paired with the Zymo column produced extraction yields very comparable to the Qiagen extraction methods. This alternate extraction protocol will be further evaluated using an expanded panel of archived swab samples at the CDPH to facilitate future transition to public health laboratories to improve COVID-19 diagnostics.

1.8. Alternative RNA extraction technologies for saliva-based diagnostics

During Phase 1 testing activities, ORNL identified alternative RNA extraction technologies, optimized saliva-based diagnostics, and created allele-specific RT-qPCR methods to rapidly detect SARS-CoV-2 and its variants. These alternatives safeguarded a robust clinical testing program at ORNL that could have been derailed by supply chain shortages. Technologies and capabilities developed here in consultation with the multi-laboratory NVBL testing team can be applied to future biosecurity, biosurveillance and healthcare diagnostics programs to rapidly respond to emerging threats.

We demonstrated that a non-EUA approved RNA purification system, NucleoSpin RNA Plus isolation kit (Machery-Nagel), efficiently extracted viral RNA from the SARS-CoV-2 surrogate bacteriophage MS2. This system worked efficiently in saliva matrices, including artificial saliva (Pickering Laboratories) and frozen, multiple donor human saliva (Innovative Research). RNA recoveries from fresh saliva were lower and were not significantly improved by the addition of sample stabilizers or nuclease inhibitors. The addition of DTT to samples increased assay signal strength by almost 6-fold. Thus, fresh saliva samples can be stored cold without additives for rapid processing—a practice now applied by many community surveillance programs.

To evaluate the potential for test methods that do not require RT-qPCR, we compared the CDC EUA method with a commercial colorimetric LAMP assay (New England Biolabs). Both assays readily detected SARS-CoV-2 N gene transcripts spiked in pooled saliva and immediately extracted. However, samples spiked with N gene transcript and added directly to the LAMP assay mixture were not detected, demonstrating a requirement for sample purification and concentration. We also evaluated the Yale-developed Saliva Direct assay that does not require RNA purification. Several common beverages were observed to interfere with saliva-based detection results, emphasizing the importance of supervised saliva collection and abstinence from food or beverage before sample collection.

Clinical diagnostic tests at ORNL were accelerated by automating RNA extraction procedures and implementing saliva-based diagnostics. Together with ORNL Health Services, we implemented KingFisher Flex automation for RNA extraction from nasopharyngeal swab samples in a CLIA-certified testing lab that used the multiplex Thermo COVID-19 TaqPath assay. This advance amplified ORNL's testing capabilities, enabling rapid diagnostic testing of swab samples from UT-Battelle staff and contractors and enabling continuous safe, on-site

operations during Phase 1 of the return to work process. We also collaborated on the implementation of the Saliva Direct assay that was made available to staff under that EUA. Although this simple assay was used less frequently due to the additional time required for sample collection compared to swab sampling, it provided a valuable alternative test in case swabs or molecular reagents would become unavailable.

New SARS-CoV-2 variants have emerged globally and spread rapidly in the U.S., creating a need for rapid diagnostics that identify variants of concern in clinical samples in time for medical or public health response. To address this problem, we developed an allele-specific RT-qPCR method to rapidly distinguish between RNAs from reference and variant SARS-CoV-2 in COVID-19 samples. While next generation sequencing provides exceptionally detailed data for biosurveillance, new methods are required to distinguish strains in a clinically relevant timeframe. A rapid *in vitro* transcription system was developed to produce full-length RNA transcripts of the SARS-CoV-2 N and S genes. These standards were valuable for the development of rapid diagnostic methods and could be stored without degradation, shared freely, and used safely in BSL1 environments. Subsequently, we used site-directed mutagenesis to modify the S gene reference sequence in a plasmid vector, introducing characteristic mutations found in B.1.1.7, B.1.351 and P.1 variants of concerns. These variant templates were used to develop an allele-specific RT-qPCR method that blocks the reference gene sequence and preferentially amplifies variant sequences with 4-8 exponential cycles of discrimination.

Task 2: Develop Affinity Reagents and Novel Platform Approaches

Institutions: LANL; SNL; Carterra Inc., Dublin, CA; University of New Mexico

Antonietta M. Lillo [corresponding author], Nileena Velappan, Hau Nguyen, Daniel Bedinger, Chunyan Ye, Betty Mangadu, Steven B. Bradfute, Robert Meagher, and Geoff Waldo

Scientific Title: In vitro evolution-enabled selection of monoclonal human antibodies specifically recognizing SARS-CoV 2 spike protein

2.1 Objective

The overarching goal of this project was to develop antibodies for sensitive and selective detection of SARS-CoV 2, the causative agent of COVID-19. We chose the ACE2 receptor-binding domain (RBD) of viral spike protein as the target antigen.

Antibody selection and characterization was performed by in vitro evolution of a human single chain antibody (scFv) library, synergizing phage and yeast display technologies (Figure 2.1). Additionally, in order to select antibodies targeting precisely the receptor binding motif of RBD [i.e. the region of RBD with the most sequence variation between SARS-CoV 2 RBD (RBD2) SARS-CoV RBD (RBD1)] some of our selections included RBD1 as a counter selector. As a result, we have obtained a set of 18 anti-RBD antibodies (Figure S2.1), mostly selective for RBD2 (Figure 2.2) with the exception of antibody R04, which binds more strongly to RBD1. Remarkably this antibody was obtained from selections not including counter selector RBD1. Yeast-displayed scFv's affinities (K_D s) for RBD2 were determined by flow cytometry (Figure S2.1A and Table S2.1). In order to obtain soluble antibodies (i.e. free of the display organism) resembling full-length IgGs, we produced minibodies (molecules containing two

copies of scFv held together by rabbit or human Fc). Antibodies in this format behaved similarly to yeast-displayed scFvs (Figure 2.2B and C), and allowed us to perform some preliminary experiments for identification of non-competitive RBD2 binders (“antibody pairs”, data not shown). Minibodies affinity for RBD2 were determined by surface plasmon resonance (SPR) (Table S2.1). Based on affinity measurement and likelihood of forming pairs we selected antibody B04, E01, E08, F07, G07, H01, H05 and S01 for conversion to IgGs.

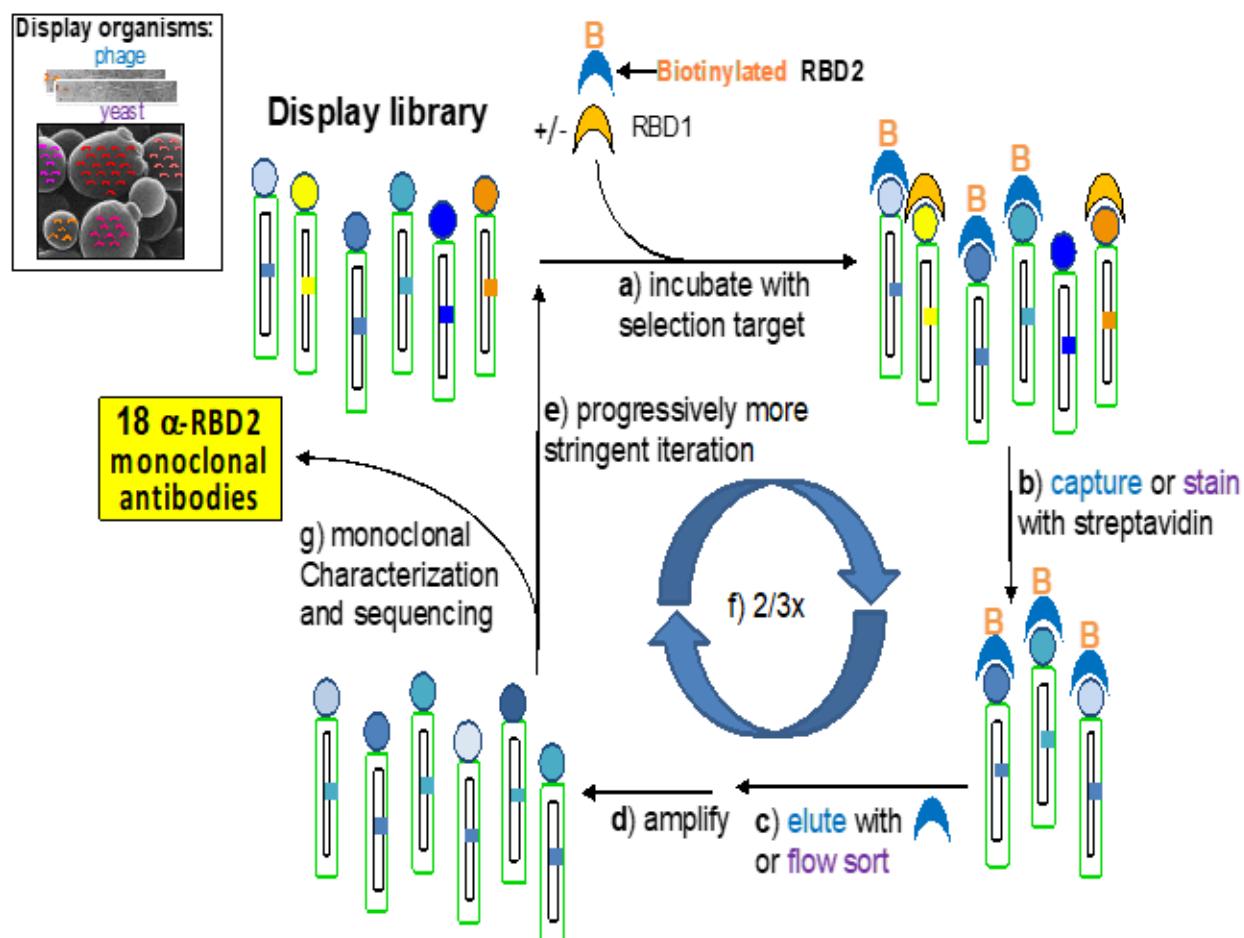


Figure 2.1: Selection of monoclonal antibodies by in vitro evolution of display libraries. Phage and yeast display technologies were used in tandem for selection of 18 anti-SARS-CoV 2 spike protein RBD (RBD2). Selection steps a through g are indicated. Actions color-coded in blue and purple pertain to phage and yeast sections, respectively. Subtractive selection strategies included: 1) the use of non-biotinylated SARS-CoV RBD (RBD1) during the incubation step (a); and 2) elution with excess unbiotinylated RBD2 during the phage display elution step (c)

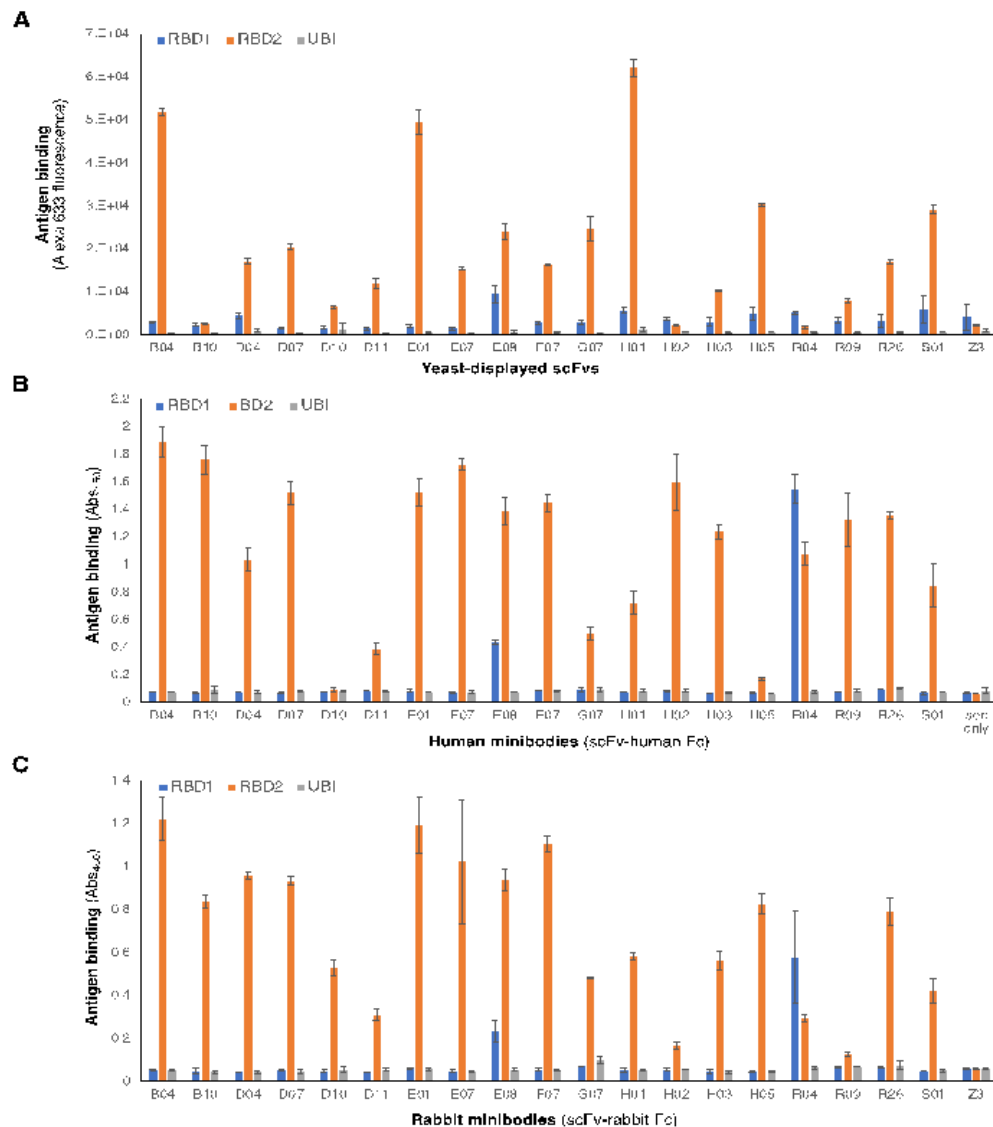


Figure 2.2: Affinity and specificity of selected antibodies. Relative binding affinity of (A) monoclonal yeast-displayed scFvs and minibodies, i.e. scFv-Fc chimeras (human Fc, **b**; rabbit Fc, **C**) measured at antigen concentration below saturation. Data include binding to a negative control antigen (ubiquitin, UBI), and a negative control human anti-influenza M2 antigen scFv (A)/rabbit minibody (C) called Z3. The height of each bar is an average of three measurements and the error bars correspond to the standard deviations of each set of three measurements.

We also converted R04 because of its unique preference for RBD1 over RBD2. IgGs' affinity for RBD2 were determined by SPR (Figure S2.2B and Table S2.1). For those antibodies available in multiple formats, we noticed that duplication of the variable region (i.e. conversion to minibodies and/or IgG) resulted mostly (82%) in decrement of affinity (increment of K_D). The remainder of the clones were equally split in those with same affinity (same K_D) and those with higher affinity (lower K_D) (Figure S2.3). IgG's ability to specifically recognize RBD2 even in the context of spike S1 portion was confirmed by fluorescence-linked immunosorbent assay (FLISA, Figure S2.4).

2.2 Diagnostic potential of antibodies

Immunoassay are much more specific and sensitive when pairs of antibodies recognizing two distinct regions of the target antigen are used rather than single antibodies. Therefore, we screened our IgGs for their ability to bind non-competitively to the antigen (epitope binning) by both SPR (**Figure 2.3**) and sandwich ELISA (Figure S2.5).

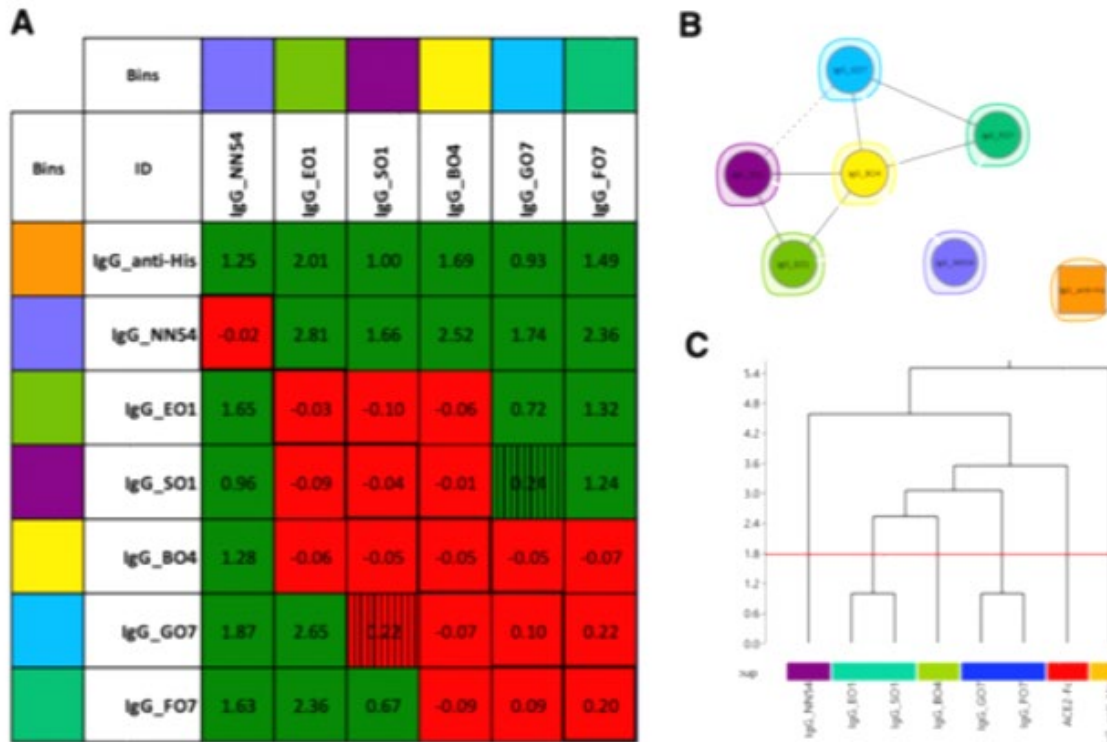


Figure 2.3: Antibody epitope binning by surface plasmon resonance (SPR). IgGs were tested for their ability to bind SARS-CoV 2 spike protein's receptor binding domain (RBD2, histidine tagged) by SPR. Antihistidine tag IgG was used as a positive control non-competitive RBD2 binder. And commercial gold standards anti-RBD2 antibody NN54 was included in the analysis. **(A)** The green and red cells in the heat map rendition of the SPR data **(A)** indicate the intersection of two non-competing and competing IgGs, respectively. The network plot rendition of the Spr DATA **(B)** indicate competing IgGs connected by a line, whereas all the non-competing igGs are isolated. The dendrogram rendition of the SPR data **(C)** shows the relatedness of the competition profiles across the clones. This can be then used to create cut-offs to group similar epitope clusters together.

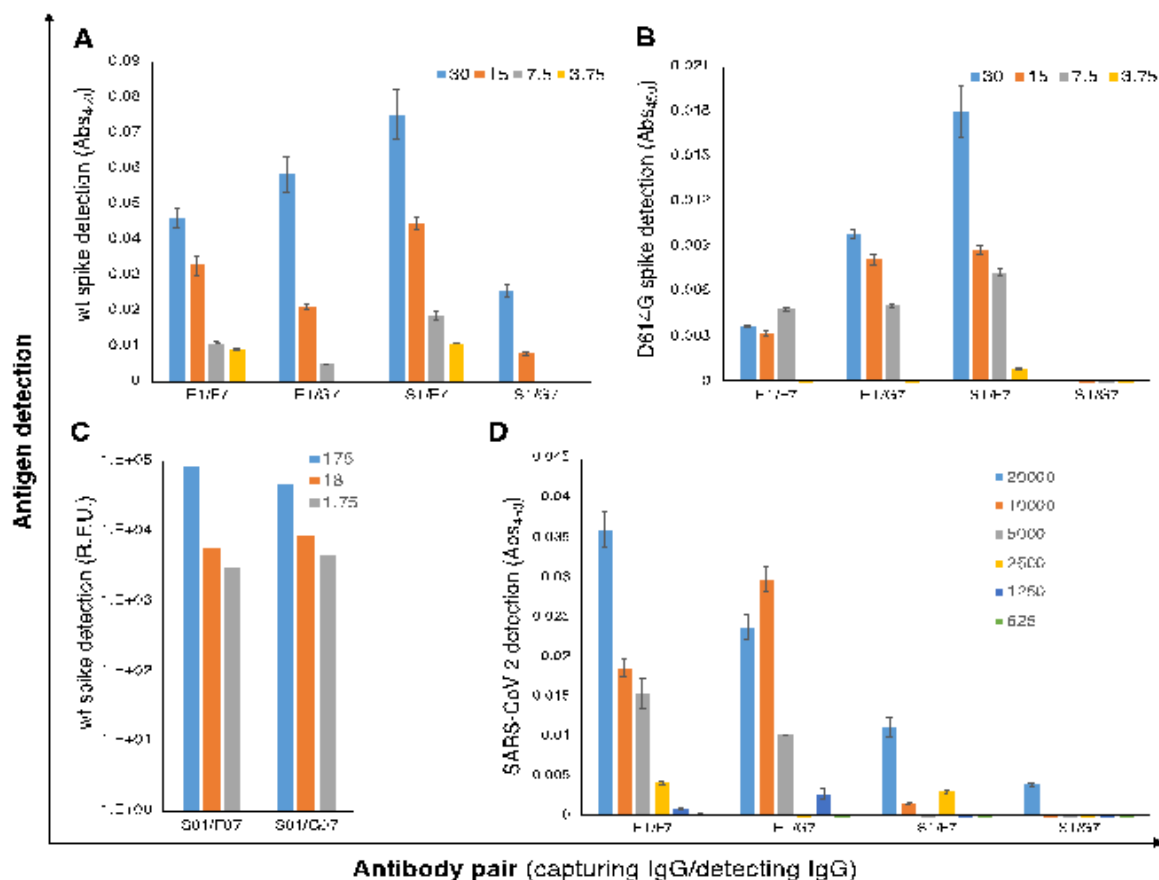


Figure 2.4: Limit of detection of trimeric spike by whole SARS-CoV 2. Detection of wild type spike (A) and D614G mutant spike (B) by sandwich ELISA. Detection of wild type spike by SpinDX (C). Detection of heat inactivated whole SARS-CoV 2 virus by sandwich ELISA (D). Binding to negative control antigen myoglobin (A and B) and beta coronavirus (D) have been subtracted from reported data. Signal detected in the absence of antigen (noise) has been subtracted from data reported in C.

A set of 4 IgG pairs were identified: E1/F07; E1/G07; S1/F07 and S1/G07. These pairs were tested for sensitivity of detection of spike protein and whole SARS-CoV 2 virus (Figure 2.4). In sandwich ELISA: 1) pairs E01/F07 and S01/F07 detect wild type spike at ≤ 3.4 pM (Figure 2.4A); 2) pair S01/F07 detect spike mutant D614G at a minimum of 3.4 pM (Figure 2.4B); and 3) pairs E01/F07 and E01/G07 detect whole heat inactivated SARS-CoV 2 virus at a concentration of 1.25×10^3 mL (Figure 2.4D). In the Sandia National Laboratory's SpinDX diagnostic platform, the best performing IgG pairs were S01/F07 and S01/G07 (Figure 2.4C), which detect spike protein at 0.16 and 9.6 pM, respectively.

Therapeutic potential of LANL antibodies:

Although discovery of therapeutic antibodies was not part of our proposal, we were able to explore the therapeutic potential of our antibodies through collaborations with UNM (Steven Bradfute) and with LANL coworkers (Sofiya Micheva-Viteva). SPR analysis revealed that all of

our IgGs (including B04, which does not form pairs, see Figure 3) compete with ACE2 for binding to RBD2 (Figure 2.5A), suggesting that they could be used as a therapeutic cocktail. These results were partially corroborated by immuno-cytochemistry analysis (Figure 2.5B).

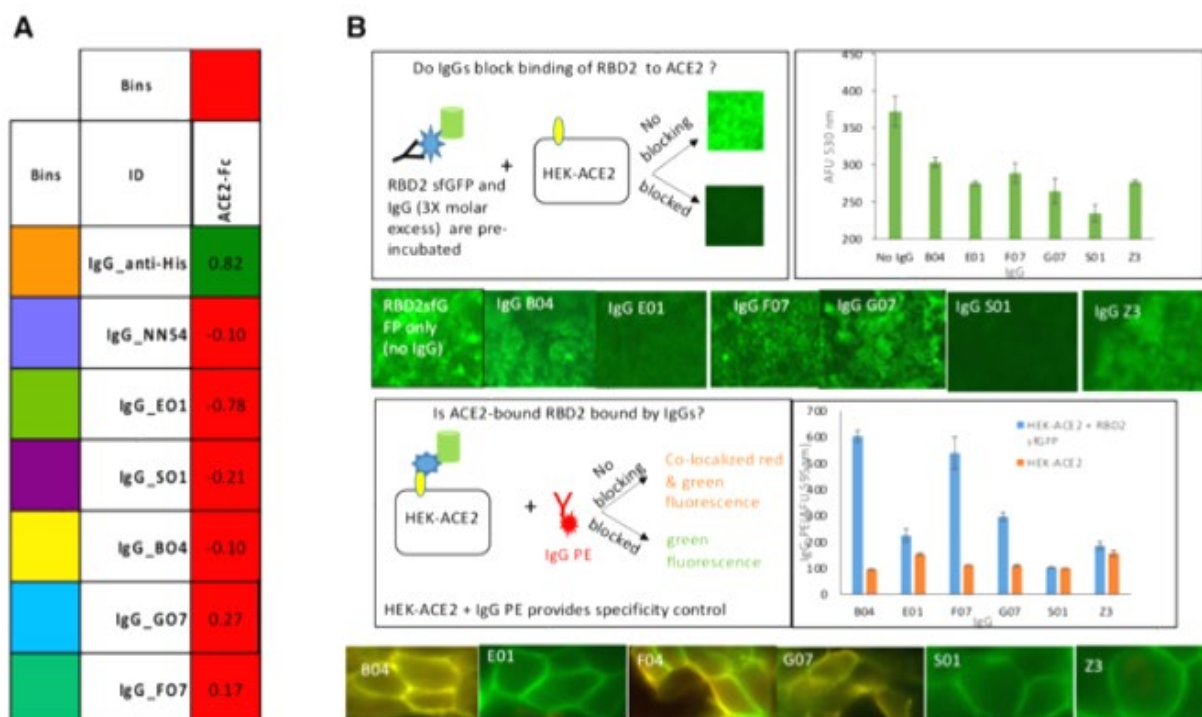


Figure 2.5: Antibody interference with binding SARS-CoV 2 spike protein's receptor-binding domain (RBD2) to ACE2. Surface plasmon resonance epitope binning heat map (A) shows that recombinant ACE2-Fc and LANL IgGs B04, E01, F07, G07 and S01 compete for RBD2 binding. IgGs Nn54 and anti-histidine tag were used as positive and negative controls for competitive binding, respectively. (B) Immuno-cytochemistry studies using HEK cells expressing ACE2 and microscopy analysis, revealed that IgGs B04, F07, G07 and in particular IgGs E01 and S01 block super folder (sf) GFP-RBD2 chimera's binding to cell expressed ACE2 (top panels). sfGFP-RBD2 bound to HEK cells also binds PE-labelled B04, F04, and G07 but not PE-labelled E01 and S01. Anti-influenza M2IgG was used as a positive control for absence of binding (bottom panels).

Finally, in-vitro study of HEK cells viral infection demonstrated that all our IgGs, except G07, neutralize the live virus (Figure 2.6A) and that antibody pairs S01/F07 and E01/F07 outperform the most active member of each pair (Figure 2.6B).

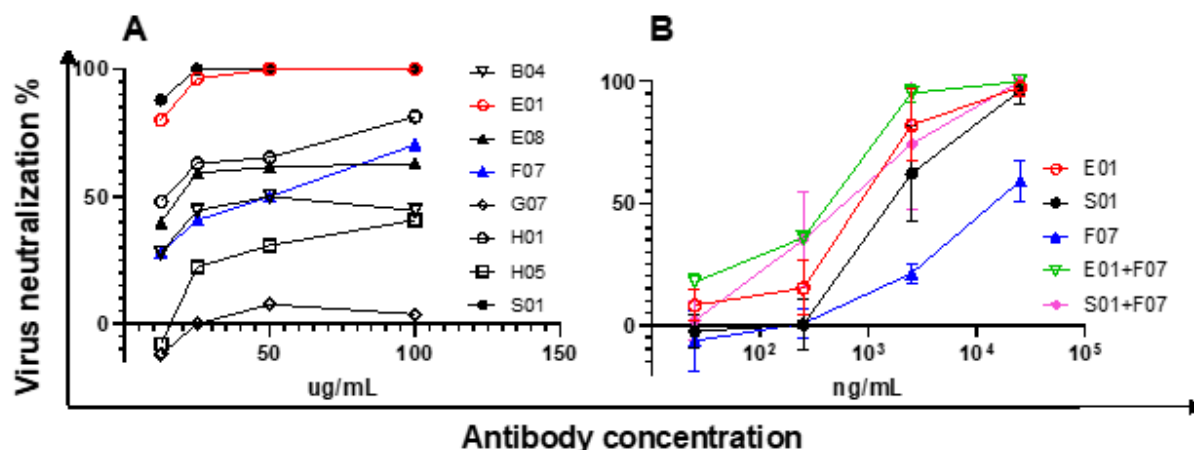


Figure 2.6: Antibody neutralization of SARS-CoV2 infection HEK cells expressing ACE2. Single antibody analysis (A) and pairs versus single antibody analysis (B). Data reported in B are averages of 3 measurements plus corresponding standard deviations (error bars).

2.3 Conclusions

We have selected and characterized a set of 18 antibodies recognizing SARS-CoV 2 spike protein's receptor binding domain (RBD2). Four of these antibodies (E01, F07, G07 and S01) form four pairs of non-competitive RBD2 binders (E01/F01; E01/G07; S01/F07; and S01/G07). These same antibodies plus antibodies B07, E08, H01, and H05 compete with recombinant ACE2 for binding to RBD2, and neutralize viral infection of HEK cells. Antibody pair S01/F07 can detect as little as 160 femtomolar spike by SpinDx, and pair E01/F07 can detect as little as 1.25E+3/mL viral particles by sandwich ELISA.

In addition to fulfilling the main objective of this proposal (development of high selectivity/sensitivity assays for detection of SARS-CoV 2) we have also obtained potentially therapeutic antibody cocktails.

Last but not least, this project has allowed us to explore collaborative side projects with LANL coworkers (B and T divisions) and form collaborations with UNM, Carterra inc., Lawrence Berkley National Laboratory and Argonne National laboratory. This network will be a solid foundation for future proposals on COVID-19 research and obtainment of additional funding.

2.4 Supplementary information and graphics

B04
SYVLTQPPSVSVAPGKTARITC**GGNNIGIRSVH**WYQQKPGQAPVLVI**YDSDRPS**GIPERFSGSKSGNTATLTISRVEAGDEADYYC**QVWDS****SSDHPV**FGGGTKLTV
LSGGSTITSYNVYYTKLSSSGTQVQLVESGAIEVKKPGASVKVSCAS**GYTFTTRYMH**WVRQAPGQGLEWMG**IINPSGGTTSYAQKFQGR**VTMTTRDTSTSTVYMELS
SLRSEDATAVYCAR**SFELTSFDY**WGQGLTVTVSS

B10
QSVVTQPPSVSGAPGQRTVISC**TGSSSNIGSR**TVNWWYQQLPGTAPKLLI**YANNQRP**SGVPDRFSGSKSGTSASLAISGLQSEDEADYYC**AAWDDSLNGYV**FGTGK
LTVL**SGGSTITSYNVYYTKLSSSGT**QVQLQSGPGLVKPSQTLSTCAIS**GDSVSSNSAT**WNWIRQSPSRGLEWL**GR**TY**YGSKW**HSDY**AVSVKS**RITINPDTSKNQIS
LHNPVTPEDTAVYCAR**GRSYAFDI**WDQGTMTVTVSS

D04
SYVLTQPPSVSVAPGKTARITC**GGNNIGWKS**VHWWYQQKPGQAPVLV**YNDNDRPS**GVPERFSGSNSGNTATLTISRVEAGDEADYYC**QVWDS****SSDHLV**FGGGTKL
TVL**SGGSTITSYNVYYTKLSSSGT**QVQLVQSGAEVKKPGSSVKVSCAS**GGTFSSY**AIWVRQAPGQGLEWMG**GIIPFGTANYAQKFQGR**VTITADESTSTAYMELS
SLRSEDATAVYCAR**ASGRWLQF**WHYYGMDVWGQGTMTVTVSS

D07
SYELTQPPSVSVAPGETARMTC**GGNNIGTKGVH**WYQQKPGQAPVLV**YDSDRPS**GIPERFSGSNAGNTATLTISRVEAGDEADYYC**QVWDS****SRSDQYV**FGTRTKL
TVL**SGGSTITSYNVYYTKLSSSGA**QVTLKESGPVLVKPTETLTCTV**SGFSLNARMGV**SWIRQPPGKALEWLA**HIFSNGEKSYSTLSK**SRLTISKDTSKQSVLTM
NMDPVDATATYCAR**LDYYDSSGYLVGGAFDI**WGQGTMTVTVSS

D10
QSVVTQPPSASGSPGQVTITISC**SGNSANIGNPN**VNWWYQQLPGTAPKLLI**YSNNQRP**SGVPDRFSGSKSGISASLAISGLQSEDEADYYC**AAWDDSLNGV**IFGGGKTL
TVL**SGGSTITSYNVYYTKLSSSGT**QVQLVQSGAEVKKPGESLKISCKGS**GYSTFSY**WIGWVRQMPGKGLEWMG**IIPGDS**TRYSP**SG**QGVITISADKSISTAYLQW
SSLKASDTAMYYCAR**RHSGSYSGAFDI**WGQGTMTVTVSS

D11
SYELTQPPSVSVAPGQTARITC**GGNNIGSKSVH**WYQQKPGQAPVLV**YDSDRPS**GIPERFSGSNSGNTATLTISGTQAMDEADYYC**QAWDS****SSTAYV**FGSGTKLTV
VL**SGGSTITSYNVYYTKLSSSGT**QVQLQSGAEVKKPGSSVKVSCAS**GFTFSNYAMS**WVRQAPGKGLEWV**SAISGGGATFHADSVKGR**FTISRDNKNTLYLQMN
SLRAEDTAVYCAR**RVGYDSSGYWSDAFDI**WGQGTMTVTVSS

E01
SYELTQPPSVSVAPGETARITC**GGDNIGRRHVH**WYQQKPGQAPVLVI**YDSDRPS**GIPDRFSGSNSGNTATLTIGRVEAGDEADYYC**QVWGS****NDPHV**FGTGKLT
TVL**SGGSTITSYNVYYTKLSSSGT**QVQLQWGAAGLLKPSETLSLKCAVY**GGSFSGY**WGWIRQSTGKGLEWIG**EINRSGSTNYNPSLKS**RVITISVDTSKNQFSLKLSS
VTAADTAVYCAR**GGARYYGGSGSYRSTPRPYFDY**WGQGLTVTVSS

E08
SYVLTQPPSVSVAPGKTARITC**GGNNIGWKS**VHWWYQQKPGQAPVLV**YDSDRPS**GIPERFSGSNSGNTATLTISRVEAGDEADYYC**QVWDS****SSDLV**FGGGTKLTV
VL**SGGSTITSYNVYYTKLSSSGT**QVQLVQSGAEVKKPGSSVKVSCAS**GGTFSSY**AIWVRQAPGQGLEWMG**GIIPFGTANYAQKFQGR**VTITADESTSTAYMELSS
LRSEDATAVYCAR**ASGRWLQF**WHYYGMDVWGQGTMTVTVSS

F07
SYVLTQPPSVSVAPGQTARITC**GGNNIGSKSVH**WYQQKPGQAPVLV**YDSDRPS**GIPERFSGSNSGNTATLIISRVEAGDEADYYC**QVWDS****SSVHYV**FGTGKLT
VL**SGGSTITSYNVYYTKLSSSGT**QVQLVQSGAEVKKPGSSVRVSCV**SGYFTFGYMH**WVRQAPGQGLEWMG**IINPSGGTTSYAQKFQGR**VTMTTRDTSTSTVYME
SSLRSEDATAVYCAR**VRVGASDAFDI**WGQGTMTVTVSS

G07
QSVLIQPPSASGTPGQRTVISC**SGSNSNFGSNSV**SWYQQRPGTAPKLLI**EGNNQRP**SGVPDRFSGSKSGTSASLAISGLQSEDEAEYSC**ASWDDSLNAFV**FGPGTK
LTVL**SGGSAITSYNVYYTKLSSSGT**QVQLVQSGAEVKKPGESLKISCKGS**GYSTFSY**WIGWVRQMPGKGLEWMG**IIPGDS**IRYSP**SG**QGVITISADKSFSAYLQ
WSSLKASDTAMYYCAR**LGATGAFDI**WGQGTMTVTVSS

H01
QPGLTQPPSVSLAPGQTARITC**GGNNIGSKSVH**WYQQKPGQAPVLV**YDSDRPS**GIPERFSGSNAGNTATLTISRVEAGDEADYYC**QVWDS****SRSDQYV**FGTRTKLT
VL**SGGSTITSYNVYYTKLSSSGA**QVTLKESGPVLVKPTETLTCTV**SGFSLNARMGV**SWIRQPPGKALEWLA**HIFSNGEKSYSTLSK**SRLTISKDTSKQSVLTM
MDPVDATATYCAR**LDYYDSSGYLVGGAFDI**WGQGTMTVTVSS

H02
QSVVTQPPSVSAAPGQKVITISC**SGSSSNIGNNYV**SWYQQLPGTAPKLLI**YRDTQRP**SGVPDRFSGSKSGTSASLAISGLRSEDEADYYC**ATWDKSLSGPV**FGGGTKV
TVL**SGGSTITSYNVYYTKLSSSGT**QVQLQSGPGLVKPSQTLSTCAIS**GDSVSSNSAA**WNWIRQSPSRGLEWL**GR**TY**YRSKWYNDYAVSVKS**RITINPDTSKNQFSL
QLNSVTPEDTAVYCAR**QDNNPYGLDV**WGQGTMTVTVSS

H03
SYELTQPPSVSVAPGQTARITC**GGNNIGSKSVH**WYQQKPGQAPVLVI**YDSDRPS**GIPERFSGSNSGNTATLTISRVEAGDEADYYC**QVWDS****SSALYV**FGTRTKTV
VL**SGGSTITSYNVYYTKLSSSGT**QVQLVESGGGLVQGRSLRLSCAAS**GFTFDYAMH**WVRQAPGKGLEWV**SGISWNSGSIGYADSVKGR**FTISRDNKNSLYLQVN
SLRAEDTAVYCAR**ELVGTTSPTDAFDI**WGQGTMTVTVSS

H05
SYVLTQPPSVSVAPGQTARITC**GANNIGRISVH**WYQQKPGQAPVLV**YDSDRPS**GIPERFSGSNFGNTATLTISRVEAGDEADYYC**QVWDSYSDHVI**FGGGTKLTV
LSGGSTITSYNVYYTKLSSSGTQVQLVQSGAEVKKPGSSVKVSCAS**GGTFSSY**AIWVRQAPGQGLEWMG**GIIPFGTANYAQKFQGR**VTITADESTSTAYMELSSL
RSEDATAVYCAR**SIFGVVISHADGY**YGMVWGQGTMTVTVSS

R04
EIVMTQSPSSLSASVGDRTVITC**QASQDISNYLN**WYQQKPGKAPKLLI**DASNLET**GVPSRFSGSGSGTGFTFTISLQPEDFATYYC**QQSYSTPYT**FGQGTKEIKS
GGSTITSYNVYYTKLSSSGA**QVQLQSGPGLVKSSQTLSTCAIS****GDSVSSNGAA**WHWIRQSPSRGLEWL**GR**TY**YRSGWYNDYAVSVKS**RITINQDTSKNQFSLQL
NSVTPEDTAVYCAR**EGGGGRMDV**WSQGTMTVTVSS

R09
QPGLTQPPSVSVSPGQTASITC**SGDKLGKYVSV**WYQQKPGQSPVLVI**YEDTKRPS**GIPKRFSGSNSGNTATLTICGTQAVDEADYYC**QAWDSSV**FGGGTKLTVLS
GGSTITSYNVYDTKLSSSGTQVQLVQSGAEVKKPGASVKVSCAS**GYTFTSYGIS**WVRQAPGQGLEWMG**WISAYNGNTNYAQKFQGR**VTMTTDTSTSTAYMELRS
LRSDDTAVYCARD**MELRPPFDY**WGQGLTVTVSS

R26
SYELTQPPSVSVAPGQTATITC**GGKNIESKSVH**WYQQKPGQAPVLV**YDSDRPS**GIPERFSGSNSGGAATLTISRVEAGDEADYYC**QVWDS****SPSDHYV**FGPGTKLT
VL**SGGSTITSYNVYYTKLSSSGT**QVQLVESGGGVQPGRLRLSCAAS**GFTFSYAMH**WVRQAPGKGLEWV**AVISYDGSNKYADSVKGR**FTISRDKAKNTLYLQMN
NSLRGEDTAVYCAR**ELSYDSSGYLGDWYFDL**WGRGTLTVTVSS

S01
EIVMTQSPSSLSASVGDSTVITC**QASQDISNYLN**WYQQKPGKAPKLLI**DASNLET**GVPSRFSGSGSGTGFTFTISLQPEDFATYYC**QQYDNFPPT**FGPGTKVDIKSG
GSTITSYNVYYTKLSSSDTQVQLVESGGGLVKPGSLRLSCAAS**GFTVGSNYS**WVRQAPGKGLEWV**SVISGGSTY**YADSVKGRFTISRDNKNTLYLQMNLSRA
EDTAVYCAR**GSSGAWYFDL**WGRGTLTVTVSS

Figure 2S.1: Sequences of unique antibodies derived from all selections. Single chain antibodies (scFvs) B04 through H05 were obtained by competitive selections using chemically biotinylated RBD2 as a target. scFvs R04 through S01 were obtained by non-competitive selections using avitagged-biotinylated RBD2 as a target. The three complementarity-determining regions (CDRL1, 2, and 3) in each scFv's variable light regions (VL) are indicated in red; the linker between the VL and the scFv's variable heavy portion (VH) is indicated in gray; the CDRH1, 2, and 3 are indicated in green. The sequences differ the most in the CDRH3 regions. Sequences obtained from competitive selections (B04 through H05) are more similar to each other than sequences obtained from non-competitive selection (R04 through S01).

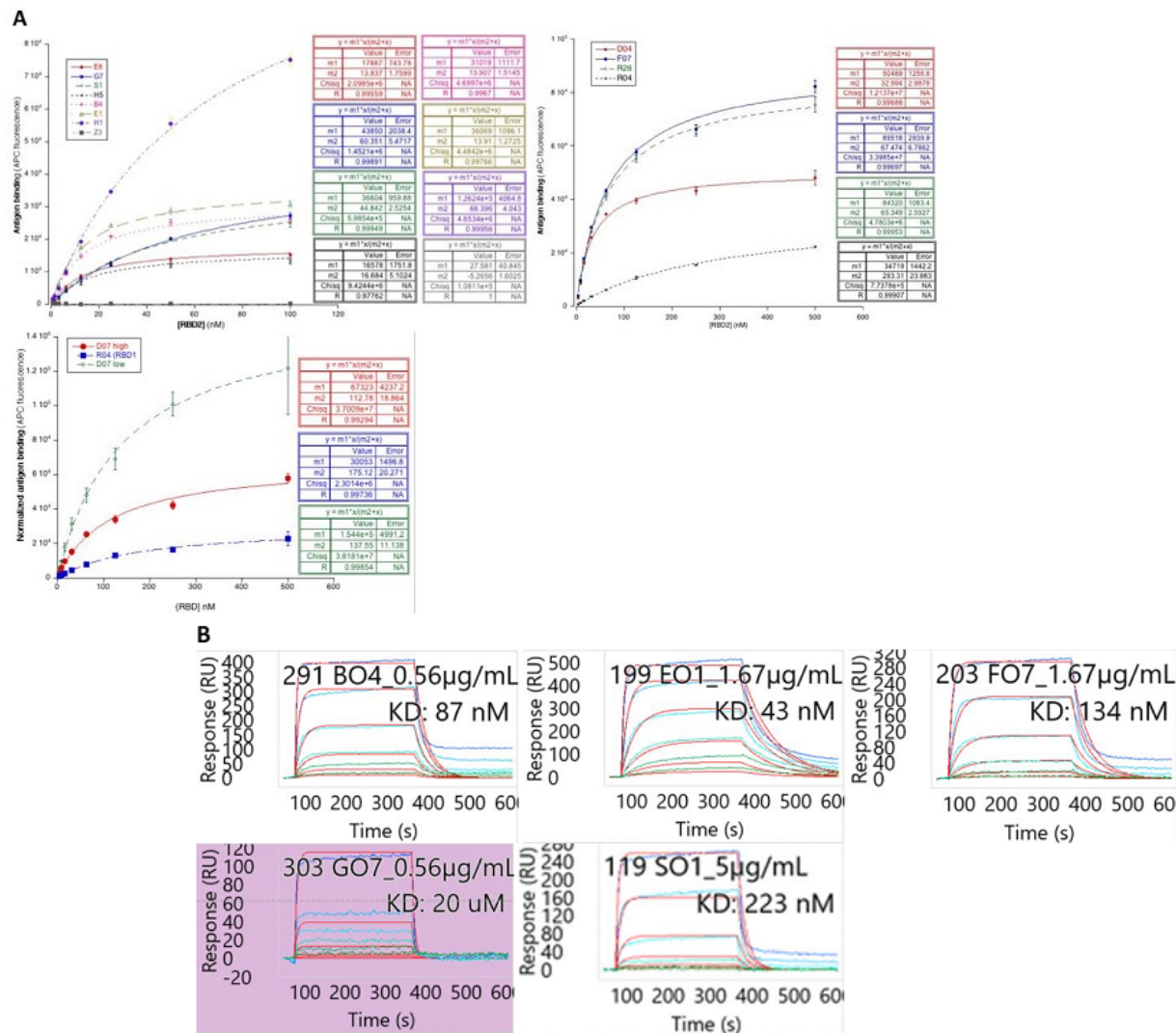


Figure 2S.2: Kinetic data. **A)** Graphs from flow cytometry-based kinetic measurements of yeast-displayed single chain antibodies (scFv). The upper two graphs are kinetics of RBD2 binding. The lower graph contains kinetics of scFv R01 binding to RBD1 and kinetics of scFv F07 binding to RBD2 at two different yeast densities. The minimal differences of K_D s measured in these two conditions shows that yeast density does not affect kinetic measurements. **B)** Representative sensograms from surface plasmon resonance (SPR)-based kinetic measurements.

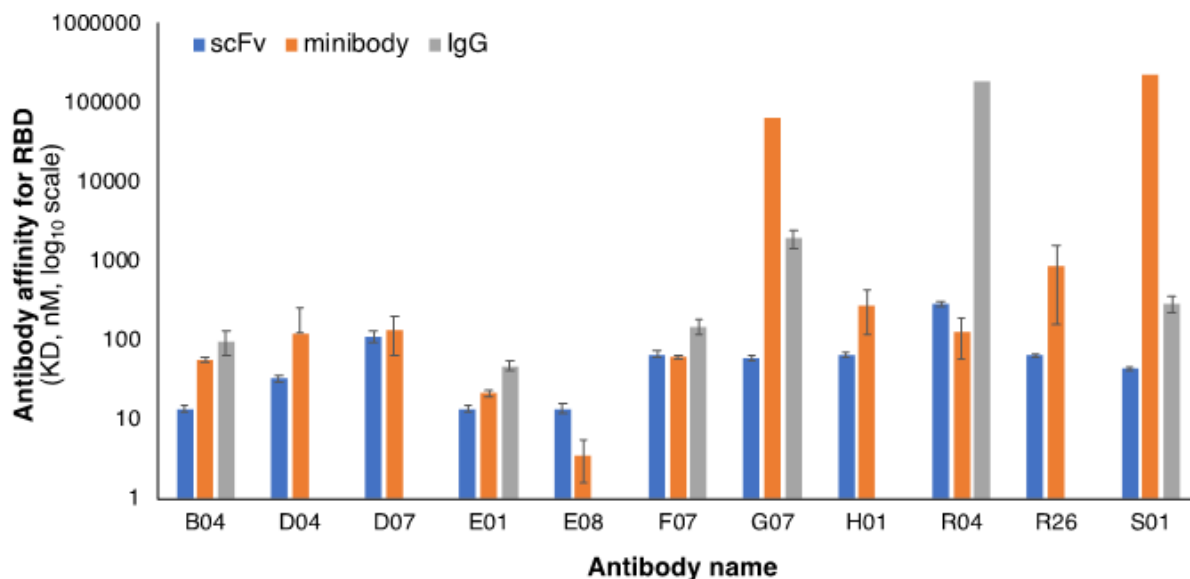


Figure 2S.3: Affinity variations depending on antibody format. Affinities of antibodies for SARS-CoV 2 spike protein's receptor-binding domain (RBD2) are reported as dissociation constants (KD, lower KD → higher affinity) for: 1) single chain (scFv, blue bars); 2) minibody (orange bars); or 3) igG (grey bars) format. For affinity measurements repeated multiple time, K_D averages and corresponding standard deviations are reported.

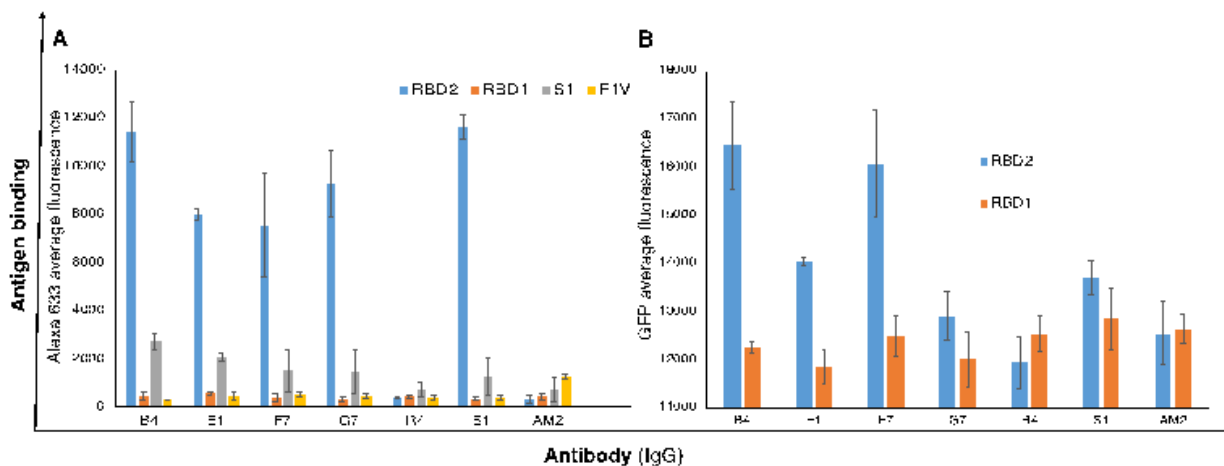


Figure 2S.4: Specificity of IgG interactions. IgGs were immobilized on plastic and tested for recognition of either (A) chemically biotinylated SARS-CoV 2 RBD (RBD2, blue bars) and SARS-CoV RBD (RBD1, orange bars) and avitag-biotinylated SARS-CoV 2 spike subunit 1 (S1, grey bars), subsequently stained with streptavidin-Alexa 633, or (B) super folded GFP-RBD2 (RBD2, blue bars) and super folded GFP-RBD2 (RBD2 orange bars) chimeras. Antigen *Y. pestis* F1V (F1V) and anti-F1 antibody aF1Ig Am2 (AM2) were used as negative controls. Average or three measurements plus standard deviations (error bars) are reported.

Table 2S.1 : Affinity of all selected antibodies

	Antibody name	Affinity for RBD2 (k _D , nM) ^a		
		<i>scFv</i>	<i>Minibody</i>	<i>IgG</i>
Competitive selections	B04	13.9 ± 1.5	56.8 ± 3.5	99.0 ± 35.6
	B10	N/D ^f	343.5 ± 99.7	N/A ^c
	D04	33.0 ± 3.0	123.5 ± 139.3	N/A ^c
	D07	112.8 ± 18.9	134.5 ± 68.6	N/A ^c
	D10	N/D ^b	N/D ^b	N/A ^c
	D11	N/D ^b	798.5 ± 567.8	N/A ^c
	E01	13.9 ± 1.3	21.5 ± 2.12	48.3 ± 7.4
	E08	13.9 ± 1.8	3.6 ± 2.0	N/D ^b
	F07	67.5 ± 6.8	61.5 ± 3.5	151.8 ± 30.5
	G07	60.3 ± 5.5	63900	1966.7 ± 503.3
	H01	66.4 ± 5.1	281.0 ± 162.6	N/D ^b
	H02	N/D ^b	15.5 ± 7.8	N/A ^c
	H03	N/D ^b	117.0 ± 52.3	N/A ^c
	H05	16.7 ± 4.0	N/D ^b	N/D ^b
Non-competitive selections	R04 (RBD2)	293.3 ± 24.0	127.5 ± 70.0	190000
	R04 (RBD1)	175.1 ± 20.3	N/D ^b	N/A ^c
	R09	N/D ^b	539.0 ± 223.4	N/A ^c
	R26	65.3 ± 2.6	887.5 ± 724.78	N/A ^c
	S01	44.1 ± 2.5	227000	293.0 ± 74.3
^a Determined either by flow cytometry (scFvs) or by surface plasmon resonance, SPR (minibodies or IgGs) ^b Not Determined ^c Not available in IgG format				

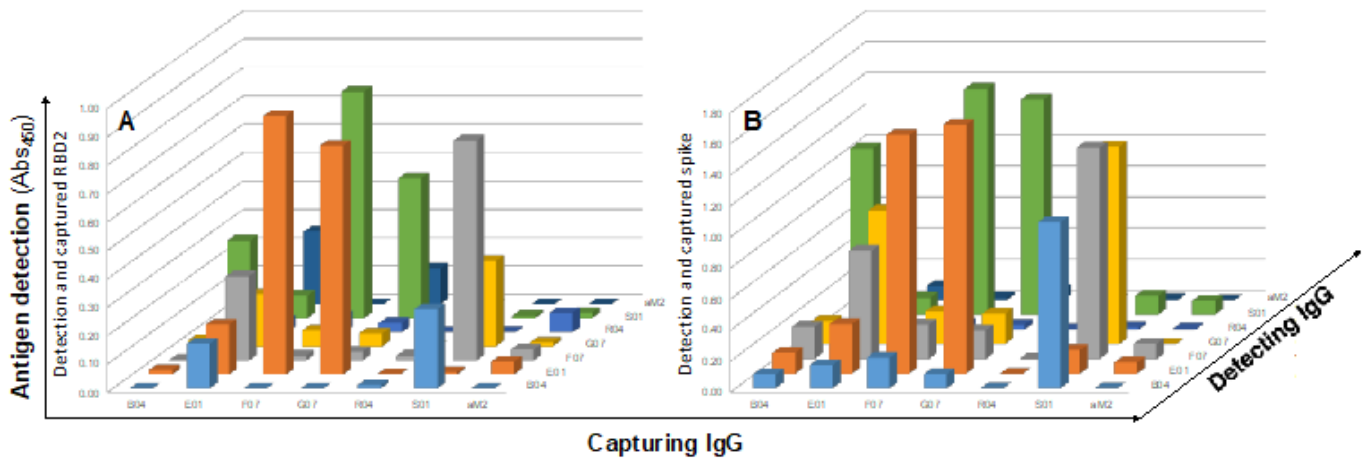


Figure 2S.5: Epitope binning by sandwich ELISA. Identification of antibody pairs (capturing and detecting IgG) capable of binding to distinct regions (epitopes) of SARS-CoV 2 spike protein receptor binding domain (RBD2, A) and SARS-CoV 2 whole spike protein (B). Plastic bound capturing IgG (x axis) immobilize the antigen, and HRP-conjugated detecting IgG (z axis) reports the captured antigen. Anti-influenza M2 antigen (aM2) antibody was used as a negative control IgG. Signals above aM2-mediated antigen detection (noise) reveal antibody pairs non competitively binding to the antigen.

Task 3. Droplet Digital Microfluidic Platforms for Detection of COVID-19

Institutions: LBNL, SNL

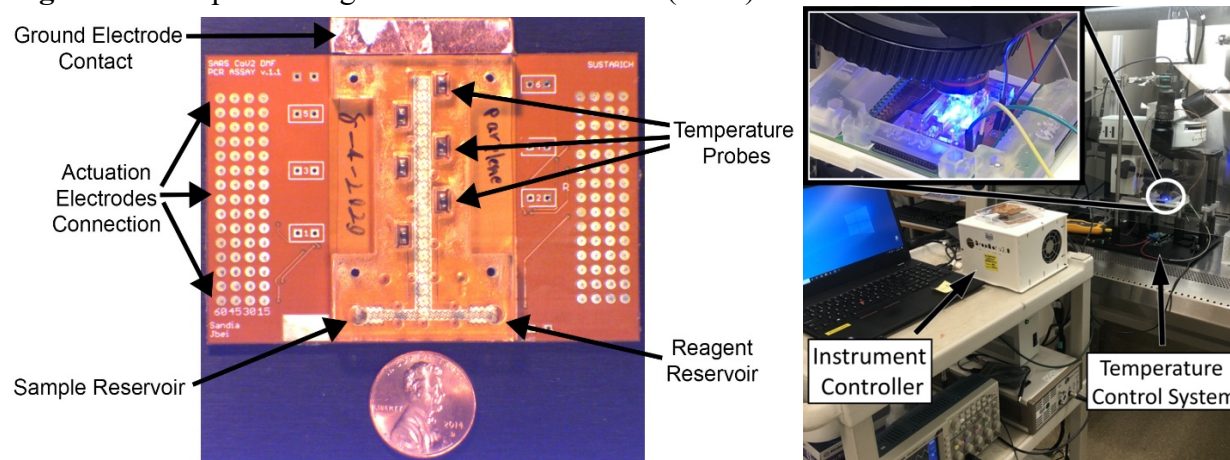
Blake Simmons, Anup Singh, Nathan Hillson, Robert Meagher, Jess Sustarich

The goal of this task was to develop a proof of concept microfluidic platform for SARS-CoV-2 nucleic acid detection, using a synthetic RNA standard for testing. The platform allows for a hundredfold reduction in reagent consumption per test, with an inherently scalable design that would allow for multiplexing and low production cost.

3.1 Disposable device

The disposable digital microfluidic (DMF) device transports, mixes and splits small ‘digitized’ packets of aqueous droplets submerged in an immiscible oil phase. The movement is provided by an electrostatic force generated by electrode pads on the device. The proof of concept DMF device is designed to mix droplets containing PCR or LAMP reagents and SARS-CoV-2 samples, generated from their respective reservoirs. The resultant mixed droplet is then moved to on-board resistive heating locations that enable the various enzymatic reactions required for reverse transcription, PCR or LAMP. During the amplification steps, periodic collection of fluorescence data are collected to provide real time data.

Figure 3.1: Disposable digital microfluidic device (DMF)



3.2 Current project status

We have built a device with a scalable and low-cost production design that successfully performs droplet generation, mixing and transportation of reagents and RNA standards. Materials compatibility at elevated temperatures was one of the largest hurdles in this project, requiring an array of different materials used for various components of the device to be tested. At the end of the project’s budget and timeline, a successful combination of materials was determined.

Remaining steps required to complete the project include refinement of data acquisition controls, fabrication of new devices for testing, and completion of an experimental matrix showing successful nucleic acid detection of SARS-CoV-2 via PCR or LAMP.

Task 4: Integrated Data Science and Genomic-Guided Approaches

Phase 1 (4.1): Integrated Data Science Approach to Support COVID Detection and Diagnosis

Institutions: LBNL, LANL, LLNL, ORNL, PNNL, SLAC

Adam Arkin (PI), Nisha Mulakken, Crystal Jaing

Phase 2 (4.2): Using Genomics-Guided Approaches to Improve Testing Effectiveness

Institutions: LBNL, LLNL, LANL, PNNL, SNL, SLAC

Nigel Mouncey (PI)

4.1 Integrated data science approach to support COVID selection and diagnosis

As part of the DOE national laboratory COVID-19 Testing and Diagnostics team, LLNL performed research for Task 4: Integrated Data Science Approach to Support COVID Detection and Diagnosis. We focused our bioinformatics research on two areas: 1). Analysis of SARS-CoV-2 proteomics structures and mutations; and 2) Analysis of all available SARS-CoV-2 genomes and design signatures on consensus regions that can capture the variants of SARS-CoV-2.

4.1.1 SARS-CoV-2 proteomic mutation analysis

Mutation analysis in various SARS-CoV-2 proteins was performed to support future applications for discovering compounds for therapeutic use. By comparing the frequency of mutations between binding sites and surrounding regions, classifying mutations by the type of secondary structure they are found in, and evaluating the solvent accessibility of a mutation based on whether it is exposed or buried within PDB models, we created a pipeline that can rank viral protein candidates as drug targets. Future work also aims to use this pipeline to explain differences in mutation rates between geographic regions that favor different drug therapies by examining the same mutation characteristics.

4.1.1.1. Technical details

Tens of thousands of protein sequences from GISAID and ViPR were processed for identifying mutations. Sequences that were too short (missing more than ten amino acids compared to the maximum length sequence), or contained undetermined amino acids were filtered out. To access the same position on all available sequences for a protein, the sequences have to be aligned first so that deletions can be represented by gaps. Each multiple sequence alignment (MSA) was generated using MUSCLE version 3.8.1441 software. This tool allows a maximum of 500 sequences to be included per run. Many MSAs were generated per protein to be able to align all available sequences.

Mutations across all 20 amino acids were counted for drug binding pockets of interest as shown in **Figure 4.1** below. A similar analysis was performed in pockets of interest in proteins: Nsp1, Nsp3, Nsp4, Nsp5, Nsp7, Nsp8, Nsp9, Nsp10, Nsp12, Nsp13, Nsp14, Nsp15, Nsp16, Orf3A, Orf7A, Spike, E, S, and N.

Using the approach outlined in Zemla, Adam et al. "GeneSV - an Approach to Help Characterize Possible Variations in Genomic and Protein Sequences." *Bioinformatics and biology insights* vol. 8 1-16. 8 Jan. 2014, doi:10.4137/BBI.S1307, from the same team, at each position

in a drug binding site, closely matched PDB models are used to determine the secondary structure the position is most likely found in. The PDB models also determine if the amino acid at the site is pointing in towards the protein, stabilizing it, or pointing outside the protein, more likely to interact with other proteins and solvent.

Residue	A	R	N	D	C	G	Q	E	H	I	L	K	M	F	P	S	T	W	Y	V	
T24	1	0	0	0	0	0	0	0	0	0	2	0	0	0	0	0	0	74600	0	0	0
T25	0	0	0	0	0	0	0	0	0	0	2	0	0	0	0	0	0	74601	0	0	0
T26	0	0	0	0	0	0	0	0	0	0	0	0	0	0	0	0	0	74603	0	0	0
L27	0	0	0	0	0	0	0	0	0	0	74603	0	0	0	0	0	0	0	0	0	0
H41	0	0	0	0	0	0	0	0	74602	0	0	0	0	0	0	1	0	0	0	0	0
M49	0	0	0	0	0	0	0	0	0	0	4	0	0	74599	0	0	0	0	0	0	0
Y54	0	0	0	0	0	0	0	0	0	0	0	0	0	0	0	0	0	0	74603	0	0
F140	0	0	0	0	0	0	0	0	0	0	0	0	0	74603	0	0	0	0	0	0	0
L141	0	0	0	0	0	0	0	0	0	0	74603	0	0	0	0	0	0	0	0	0	0
N142	0	0	74593	0	0	0	0	0	0	0	0	5	0	0	0	0	5	0	0	0	0
G143	0	0	0	0	0	74597	0	0	0	0	0	0	0	0	0	0	6	0	0	0	0
S144	0	0	0	0	0	0	0	0	1	0	0	1	0	0	0	0	74601	0	0	0	0
C145	0	0	0	0	74602	0	0	0	0	0	1	0	0	0	0	0	0	0	0	0	0
H163	0	0	1	0	0	0	0	0	0	74602	0	0	0	0	0	0	0	0	0	0	0
H164	0	0	0	0	0	0	0	0	0	74603	0	0	0	0	0	0	0	0	0	0	0
M165	0	0	0	0	0	0	0	0	0	0	2	1	0	74600	0	0	0	0	0	0	0
E166	0	0	0	0	0	0	0	74601	0	0	0	0	0	0	0	0	0	0	0	0	2
P168	0	0	0	0	0	0	0	0	0	0	0	0	0	0	74597	6	0	0	0	0	0
H172	0	0	0	0	0	0	0	0	74603	0	0	0	0	0	0	0	0	0	0	0	0
D187	0	0	0	74602	0	1	0	0	0	0	0	0	0	0	0	0	0	0	0	0	0
R188	0	74595	0	0	0	0	0	0	0	0	0	0	7	0	0	0	1	0	0	0	0
Q189	0	0	0	0	0	0	0	74602	0	0	0	0	1	0	0	0	0	0	0	0	0
T190	1	0	0	0	0	0	0	0	0	0	4	0	0	0	0	0	0	74598	0	0	0
A191	74520	0	0	0	0	0	0	0	1	0	0	0	0	0	0	0	0	2	0	0	80
Q192	0	0	0	0	0	0	74603	0	0	0	0	0	0	0	0	0	0	0	0	0	0

Figure 4.1: Residues in drug binding pocket of interest in protein Nsp5 and corresponding amino acid counts in GISAID sequences for Nsp5. The 'Residue' column shows the wild type amino acid and the position of a ligand binding residue. The rest of the columns are counts for the amino acid indicated in the column header.

In addition to mutations in the binding sites, mutations in amino acids near binding sites were examined, as well as mutations further from the binding sites to score proteins by the conservation of their drug binding sites.

The end result is a pipeline that will help prioritize proteins and their drug binding sites in drug discovery pipelines, and help researchers understand the selection pressures against various drugs.

4.1.2. SARS-CoV2 genomic signature analysis

Finding regions in SARS-CoV-2 that distinguish it from all other viruses is the key to designing molecular detection assays. Ideal signature regions are highly conserved across most isolates of the virus. Multiple signatures that span across the entire genome are needed for multiplexed assays that have high sensitivity in degraded samples where parts of the genome may be missing.

4.1.2.1. Technical details

All possible 60-mers from 41,540 SARS-CoV-2 genomes were generated using Jellyfish 2.2.10 for evaluation as signatures. Only complete, medium or high coverage genomes from GISAID were included for this analysis. Any genome with over 3,000 N's or genomic length below 28,000 were filtered out. Only viruses isolated from human hosts were included. To find unique 60-mers, the 60-mers were mapped with BLAST against an "anti-target" sequence set consisting

of all virus families other than Coronaviridae from NCBI and SARS-CoV-1, as well as the human genome. A hybridization probability score based on entropy, BLAST bit score, GC content, and number of mismatches was computed for every BLAST hit. 60-mers with a probability of over 20% to any anti-target genome was filtered out, leaving 365,292 unique k-mers.

The next step was to determine which of the unique k-mers were also highly conserved among the SARS-CoV-2 genomes. 42 BLAST databases were created out of the genomes to parallelize the conservation analysis. After the unique 60-mers were BLASTED to the target genomes, the same hybridization probability score was calculated for each BLAST result. This time 60-mers that had at least 95% probability of mapping to any of the target genomes were kept. High scoring 60-mers were split into several categories. 60-mers that map to almost all target genomes and those that are less conserved were separated since the less conserved 60-mers may be useful in distinguishing isolates in different samples. Next, each of those two groups of 60-mers were split by genomic location to make it easier to select signature regions across the genome for assay design.

The signature regions generated using the technique described here can now be incorporated into multiple existing pipelines for different types of assay design. A total of 78 microarray probes were downselected from the set of signature regions to span the SARS-CoV2 genome as shown in **Figure 4.2** and included in the LLMDA microarray, which is being used to test SARS-CoV2 positive samples for co-infection. The LLMDA can detect up to 20,000 species, including viruses, bacteria, archaea, protozoa, and fungi in one run.

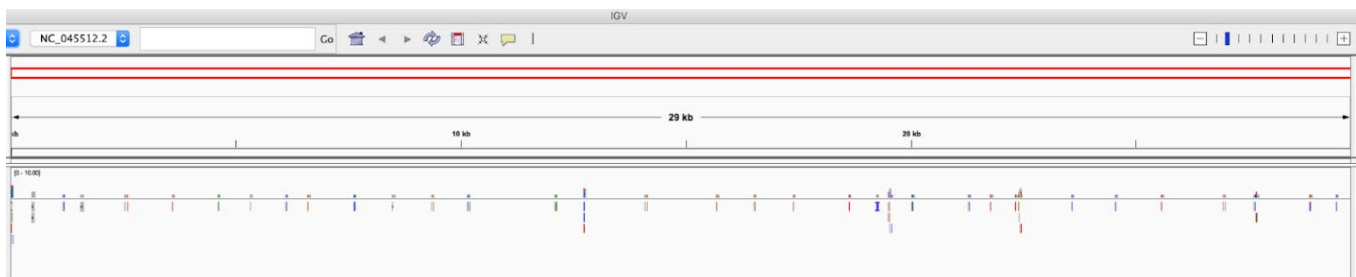


Figure 4.2: Microarray probes distributed across the SARS-CoV2 genome, reference sequence NC_045512.2) shown using Integrative Genomics Viewer (IGV) from the Broad Institute. The top panel shows the 29kb reference. The bottom panel shows where in the reference each 60 mer probe maps. Locations that are highly conserved show multiple probes at the same location.

4.2 Using Genomics-guided approaches to improve testing effectiveness

The novel coronavirus SARS-CoV-2 and other respiratory viruses are known to modify their surface proteins through nucleic acid mutations that result in changes in protein structure and content. These changes influence immune recognition and hence, the effectiveness of serological tests. Furthermore, the impact of these mutations and the resulting SARS-CoV-2 variants on the nasal microbiome in patients with and without co-infections is not known. In this task, genomics-guided approaches will be used to perform correlative analyses between the viral sequence with

protein structure, immune recognition, nasal microbiome and co-infections, both experimentally and computationally.

4.2.1 Population genomics of SARS-CoV-2

4.2.1.1 Quasispecies analysis of SARS-CoV-2 genomes

Monica Borucki, Sally Hall, Joseph Moon, Jeff Kimbrel, Chris Daum, Christa Pennacchio, Yuko Yoshinaga

Approximately 100 nasopharyngeal samples that had previously tested positive for SARS-CoV-2 viral RNA were obtained from the California Department of Public Health (CADPH) via collaboration with Drs. Debra Wadford and Sharon Messenger. The samples that were available for analysis were collected throughout California and were collected between late February 2020 to mid-July. Metadata available for each sample included age and geographic region, however, no symptomatic data was available for most samples. For each sample, SARS-CoV-2 RNA was amplified using the ARTIC v3 protocol (Freed et al., 2020, doi:[10.1093/biomethods/bpaa014](https://doi.org/10.1093/biomethods/bpaa014)) in which primer sets that span the genome amplify the genome in 2 highly multiplexed PCR reactions. The RT-PCR products were sequenced at JGI using the Illumina NovaSeq platform to ensure the error rate was low enough to allow sensitive detection of emerging variants. Due to the SARS-CoV-2 genome size and depth of coverage achieved with the NovaSeq platform, the sequence data files generated were very large with an average compressed Fastq file size of about 1 GB each. This has necessitated building a higher throughput analysis pipeline for data analysis and visualization. In particular, a V-pipe bioinformatics pipeline (Kuipers et al, 2020, <https://doi.org/10.1101/2020.10.12.335919>) is being established on LLNL HPC as part of an internally funded LDRD project that will enable these samples to be run in parallel on multiple nodes thus allowing rapid processing of large data sets, and this capability will be leveraged to allow the remainder of the samples to be analyzed. Preliminary data analysis of the spike protein data from a subset of samples indicate that indels leading to frameshifts are very common and generally occur at low frequency (<1%). Missense mutations are also detected, generally at much lower frequency as compared to synonymous mutations. We also observe that minor variants that are present at low frequency in a subset of the CADPH samples are sometimes seen as consensus changes that have later emerged during the course of the pandemic. Preliminary analysis indicate that mutation patterns may differ significantly among individual patient samples and between the timepoints in which samples were collected. Upon analysis of data, the Illumina reads for each sample, and available metadata will be deposited in GenBank SRA database. The results of the sequence data analysis will be published in an open-source journal.

4.2.1.2 Genome analyses of SARS-CoV-2 sequences

Bishoy Kamel, Yuko Yoshinaga

Clinical diagnostic and surveillance testing of samples is currently one of the many fronts critical to containing and monitoring of the SARS-CoV-2 spread. Capitalizing on over 100K sequenced and publicly available SARS-CoV-2 genomes, we developed a computational pipeline to detect conserved regions across the available SARS-CoV-2 diversity to use them as potential target sites for diagnostic and surveillance testing. Using this approach, we identified 65 sites of lower variance than sites currently used in CDC protocols for testing. We further prioritized these

conserved sites to design primers and probes for nucleic acid amplification tests that take in consideration thermodynamic properties of qPCR amplification and viral secondary RNA structure into 12 primer pairs and their corresponding probes for testing in the lab.

Using a standard qPCR assay with ROX dye, we investigated the performance of the 12 primer sets using synthetic RNA of the Wuhan-Hu-1 strain from Twist Bioscience and found that while the 12 pairs of primer sets worked as expected 7 in particular had low background noise and performed better than the current CDC 2019-nCoV-N1 & 2019-nCoV-N2 primer sets. The set of 7 primers performed well to detect >100 copies of SARS-CoV-2 template. We are currently further developing these 7 sets of primers into full TaqMan assays to increase their sensitivity and specificity with the goal of making these available for diagnostic testing and generating a peer-reviewed publication.

With the availability of more viral sequences from global sequencing efforts combined with the rise in the number of variants of concerns, we modified the analysis pipeline to process a larger set of viral sequences currently analyzing up to 700 K available genome sequences from NCBI and GISAID. Further, we incorporated a lineage sorting function using existing tools to separate the genomes into their respective lineages with emphasis on current variants of concern. The sorted lineages then undergo entropy analysis to detect conserved and slow mutating sites per lineage and then this information is collated and used to design lineage specific primers and probes that can provide discriminating power between different variants of concern such as the B.1.1.7 or B.1.351 strains while still maintaining overall specificity.

4.2.1.3 Analysis of SARS2 genome and proteome sequence variation

Kelly Williams

Monitoring genomic and proteomic sequence variation of a pathogen during an outbreak may signal turning points, such as appearance of variants that with increased or decreased (attenuated) virulence. It may also reveal when therapeutics, vaccines and diagnostics may begin to fail. We developed a system to develop an all-coronavirus genome sequence database and automate its updating as much as possible. It tackled the challenges of 1) cross-referencing identical samples from the two main data sources (GenBank and GISAID) who did not coordinate their efforts, and 2) treating the high frequency of samples with blocks of uncertain nucleotide sequence.

Variations in genome and proteome sequences were identified and monitored. Findings were:

1. A subset of coronavirus proteins were identified that were sufficiently conserved for broad phylogenetic analysis.
2. Regions of the SARS2 genome were identified where variations occurred from 10-50-fold higher than the background level of variation. One high-variation region was within the spike gene but others were found in accessory protein and polyprotein genes. A small number of exceptionally frequent variations such as spike D614G were also identified.
3. SARS2 ORF9c and ORF3a showed high levels of missense variation and ORF9c also had significant levels of gross variation (frameshifts, nonsense or unstop).
4. Spike phylogeny and receptor-binding motif sequence alignment among the SARS genus showed four main insertion/deletion types: BatA, SARS1, BatB and SARS2.
5. Analysis of the binding sites for nucleic acid based SARS2 diagnostics, such as the CDC PCR tests and Sandia LAMP assays, showed that as of October 1, these tests were not seriously compromised (variations detected in <0.04 % of the genomes).

4.2.2 Genomics-guided antibody-epitope interactions

4.2.2.1 Impacts of sequence variation on surface protein structures

4.2.2.2 Viral surface protein glycosylation

4.2.2.3 SARS-CoV-2 - Antibody-binding capacity prediction

Vince Gerbasi, Lili Pasa-Tolic, Jesse Wilson, Scott Baker, Mowei Zhou

We assessed multiple separation methods intact mass recombinant spike receptor binding domain (RBD). The method tested were capillary electrophoresis (CE), reverse phase (C2) and hydrophilic liquid interaction chromatography (HILIC). Our HILIC method outperformed CE and C2. Previous research has shown the SARS-CoV-2 spike RBD to be heavily glycosylated. Our mass spectrometry analysis indicates substantial heterogeneity in glycosylation leading a diversity of protein glycoforms. Our current method can robustly generate analyses of spike RBD glycoforms and will allow for rapid characterization of spike RBD mutants. Finally, we have initiated development of mass spectrometry methods for assessment of antibody binding to SARS-CoV-2 spike recombinant RBD proteins.

Publications in preparation:

1. Glycoprotein separation method
2. Characterization of SARS-CoV-2 RBD wildtype and mutant glycosylation
3. Development of method to assess antibody-RBD binding

4.2.3 Effects of viral sequence on the nasal microbiome and co-infections

4.2.3.1 Nucleic acid extraction from archived swab samples

4.2.3.2 Identifying co-infecting pathogens using the LLMDA technology

4.2.3.3 Metagenomic sequencing

James Thissen, Michael Morrison, Nisha Mulakken, Crystal Jaing, Yuko Yoshinaga, Chris Daum

The presence of co-infections in COVID-19 and the nasal microbiome affects disease severity and morbidity, and also affects the SARS-CoV-2 diagnostic assay sensitivity and specificity. In this task, we analyzed 201 retrospective COVID-19 samples to identify co-circulating viral, bacterial and fungal pathogens using a comprehensive microarray technology, the Lawrence Livermore Microbial Detection Array (LLMDA). We conducted bioinformatics analysis to identify pathogens whose presence is correlated or anti-correlated with COVID-19 infection, and nasal microbial communities that could affect the susceptibility or resilience to COVID-19.

We found that the LLMDA is sensitive to detect SARS-CoV-2. When compared to PCR, the array detected 92% of the PCR positive samples. The 9 samples that were not detected by LLMDA had a range of PCR Ct values, and the negative detection could be related to sample processing or degradation. The correlation of sensitivity of more comprehensive technology like the LLMDA to PCR is also conducted by another study³ using Nanopore sequencing. In this

³ Mostafa H.H., Fissel J.A., *et al.*, “Metagenomic next-generation sequencing of nasopharyngeal specimens collected from confirmed and suspect COVID-19 patients,” *mBio Clinical Science and Epidemiology*, Vol. 11, No. 6, Nov./Dec. 2020.

study, SARS-CoV-2 were confirmed by nanopore sequencing in 77.5% (31/40) of samples positive by RT-PCR, correlating with lower cycle threshold (Ct) values and fewer days from symptom onset. In the same study, possible bacterial or viral co-infections were detected in 12.5% of SARS-CoV-2 positive samples, and a decrease of microbiome diversity was observed in COVID confirmed patients.

LLMDA identified other viruses and bacteria from both COVID-positive and COVID-negative samples. *Streptococcus*, *Prevotella*, *Haemophilus*, *Mycoplasma*, and *Veillonella* were detected in both positive and negative samples. They are considered commensal microbiome.

Flavobacterium was only detected in COVID-positive samples, while *Lactococcus* was only detected in COVID-negative samples. In a recent study⁴ of 40 COVID-19 samples, five phyla, namely Firmicutes, Bacteroidetes, Proteobacteria, Actinobacteria, and Fusobacteria were detected by 16S rRNA sequencing. The microbiota of the nasopharynx was not different in patients positive for SARS-CoV-2 RNA compared to the microbiota of patients negative for SARS-CoV-2 RNA. Our study provided species level detection and differences in microbiome are observed in COVID-negative vs COVID-positive samples. Overall, additional bacteria and viruses were detected in 16% of all samples, and 17% of COVID-positive samples.

Overall, from Task 4, we expect 6 publications.

Task 5: Structure-Based Protein Design for Diagnostics

Budget: \$1,100k

Institutions: Argonne National Laboratory, Lawrence Berkley National Laboratory, Los Alamos National Laboratory, Oak Ridge National Laboratory

Andrzej Joachimiak, Paul Adams, Greg Hura, Ramesh Jha, Geoff Waldo, Jerry Parks, Hugh O'Neal

Task 5 activities focused on the topic of Structure-Based Protein Design for Diagnostics. An integrated approach for utilizing emerging structural data (e.g., the surface spike glycoprotein and new high-resolution crystal structures) was applied to address essential targets and demonstrate high-affinity reagents for non-nucleic acid-based detection systems. This work leveraged and complemented existing efforts on high-resolution structural characterization of viral proteins and variants.

5.1 Objective

The multi-laboratory working group for the Testing Research and Development Team identified opportunities where additional R&D would assist with response to the COVID-19 public health emergency. Priority emphasis was given to quick implementation as well as development of novel capabilities for current and evolving pandemic needs without placing any additional burden on current reagent demand. Priority elements capitalized on US DOE National Laboratory strengths and expertise, and also provided a forward-leaning posture to prepare for future scale-up needs, multi-element testing, and prediction for testing elements for diagnostics or therapeutics. Task 5 activities focused on the topic of Structure-Based Protein Design for

⁴ De Maio F., Posteraro B, Ponziani F.R., *et al.*, “Nasopharyngeal microbiota profiling of SARS-CoV-2 infected patients,” *Biological Procedures Online*, Vol. 22, No. 18, 2020.

Diagnostics. An integrated approach for utilizing emerging structural data (e.g., the surface spike glycoprotein and new high-resolution crystal structures) was applied to address essential targets and demonstrate high-affinity reagents for non-nucleic acid-based detection systems. This work leveraged and complemented existing efforts on high-resolution structural characterization of viral proteins and variants.

An integrated approach for utilizing emerging structural data was applied to develop novel targets and demonstrate high-affinity reagents for non-nucleic acid-based detection systems. The participating national laboratories coordinated their activities as follows:

- **Argonne National Laboratory**

The ANL team helped provide proteins for affinity reagent development for COVID-19 diagnostics. As part of the structural characterization effort conducted by the Center for Structural Genomics of Infectious Diseases (<https://csgid.org/>) the ANL/University of Chicago (ANL/UofC) team had previously cloned and purified more than 50% of the SARS-CoV-2 proteome. The ANL team can produce proteins in affinity tagged or free form that would enable the identification of high-affinity reagents and provide new constructs targeting regions of the Spike protein amenable for HTP studies.

ANL would also provide expression of key viral proteins in mammalian cells. The Spike protein variants were cloned and expressed as described previously (PMID: 32075877). Similarly, human ACE2 (wild type and variants identified by recent GWAS study) were expressed in a C-terminal fusion form. Other SARS-CoV-2 surface proteins requiring glycosylation were expressed and purified similarly.

The ANL team also used the Advanced Protein Characterization Facility to produce antibodies developed through collaborations and optimized these antibodies (affinity, specificity, stability) for diagnostic purposes. Mutants of SARS-CoV-2 proteins could be rapidly developed and used to monitor virus evolution. We worked closely with modelling efforts at ANL, LBNL and PNNL to predict mutations that may help the virus avoid detection. New reagents could be developed to monitor and detect this evolution and track down new versions of virus. Crystal x-ray and cryo-EM structures were determined for selected complexes to confirm key interactions and aid design of specific high affinity reagents. Argonne's Advanced Photon Source Structural Biology Center (SBC) beamlines were used for this project.

- **Lawrence Berkeley National Laboratory**

The LBNL team performed high-throughput small angle X-ray scattering experiments at the Advanced Light Source, using proteins provided by ANL. These studies: a) provided biologically-relevant information about the conformation, oligomeric state and flexibility of the targets in solution, b) provided experimental distance data to help constrain our *ab initio* structure prediction calculations, in particular for those targets recalcitrant to other structural solution methods, c) identified viral protein variants that alter the conformation, which might indicate changes in functionality or detectability, d) were used to screen for changes in protein conformation in the presence of candidate high-affinity reagents once they are available.

SIBYLS, located at ALS beamline 12.3.1, is the leading US beamline for mail-in high throughput SAXS (HT-SAXS) and size exclusion chromatography-SAXS (SEC-SAXS)

data collection program. In high throughput mode, data can be collected on hundreds of samples in one day, with samples loaded on 96 well plates. Structure prediction calculations will make use of the ASCR-supported NERSC supercomputing center at Berkeley Lab.

- **Oak Ridge National Laboratory**

The ORNL team contributed to neutron protein crystallography (NPX) studies and structure-based development of diagnostics. Prior to the project, the structure of the main protease from SARS-CoV-2 had been solved with X-ray diffraction to a resolution of 1.31 Å, indicating its viability as a target for NPX studies. The determination of neutron crystal structures at ORNL provided a detailed description of potential ligand binding sites, including the positions of all hydrogen atoms and associated hydrogen bond networks. The resulting structures can then be used to guide the development of rapid small-molecule-based viral diagnostics, bypassing the need for polymerase chain reaction (PCR)-based approaches. Specifically, ORNL performed high-throughput, supercomputer-based virtual screening on the Summit supercomputer to identify small molecule ligands that bind the protease with high affinity. Understanding the molecular details of these interactions is expected to provide new routes for diagnostics that reveal the presence of coronavirus infections.

- **Los Alamos National Laboratory**

The cryo-EM structure of SARS-CoV-2 (causative agent of COVID-19) surface spike glycoprotein (S-protein) interaction with human Angiotensin-converting enzyme 2 (ACE2) had been published prior to the start of the project (PDB id: 6M17). Based on this info, LANL used Rosetta protein design and high-throughput screening to develop affinity reagents for diagnostic tests. The binding affinity between these proteins is ~35 nM. Learning from the interface they selected a peptide motif from ACE2 and redesigned around it into small globular proteins (of ~40 amino acids). They then created a library of these small globular proteins (~10,000), displayed them on yeast surface, and screened for binding activity. The top binders were selected, sequenced, and the beneficial mutations incorporated into the next cycle of Design-Build-Test-Learn. The main goal was to achieve a binding affinity which is 10-fold stronger than the native RBD and ACE2 interaction. This then can be potentially used for diagnostics. LANL researchers also docked ACE2 in RBD in the near native conformation, while redesigning the RBD surface, to be able to predict the mutational landscape. The knowledge gained from here will be useful for creating diagnostics for evolved strains in the future.

5.2 Key findings

A summary of key findings from this project are outlined below according to the main activities conducted during the funding period.

5.2.1 Antibodies

Monoclonal antibodies (mAbs) are the basis of treatments and diagnostics for pathogens and other biological phenomena. We characterized a number of monoclonal antibodies specific for several SARS-CoV-2 proteins. Collaboration with Patrick Wilson's lab at the University of Chicago resulted in isolation of specific human monoclonal antibodies. Complexes were prepared, crystallized and five structures of human antigen-binding fragments (Fabs) with the N-nucleocapsid RNA binding domain were solved at 1.50, 1.82, 2.41 Å and two at 2.70 Å resolution. The overall conformations of the N-nucleocapsid RNA binding domain in the complexes are quite similar. However, the orientations of the N-nucleocapsid RNA binding domain in the complexes relative to Fabs are different. In particular, N-protein bound by one Fab complex has a more divergent epitope than the others. We have also obtained crystal of human IgG with N-nucleocapsid RNA binding domain. The best crystals diffracted to about 3.8 Å. These structures reveal that complement-determining regions (CDR1-3) of these Fabs are distinct but bind to mostly similar epitopes of N-nucleocapsid RNA binding domain.

We also conducted a structural characterization of commercial

mAbs against the N-nucleocapsid RNA binding domain from SARS-CoV-2 using small-angle X-ray scattering and transmission electron microscopy. Our solution-based results distinguished

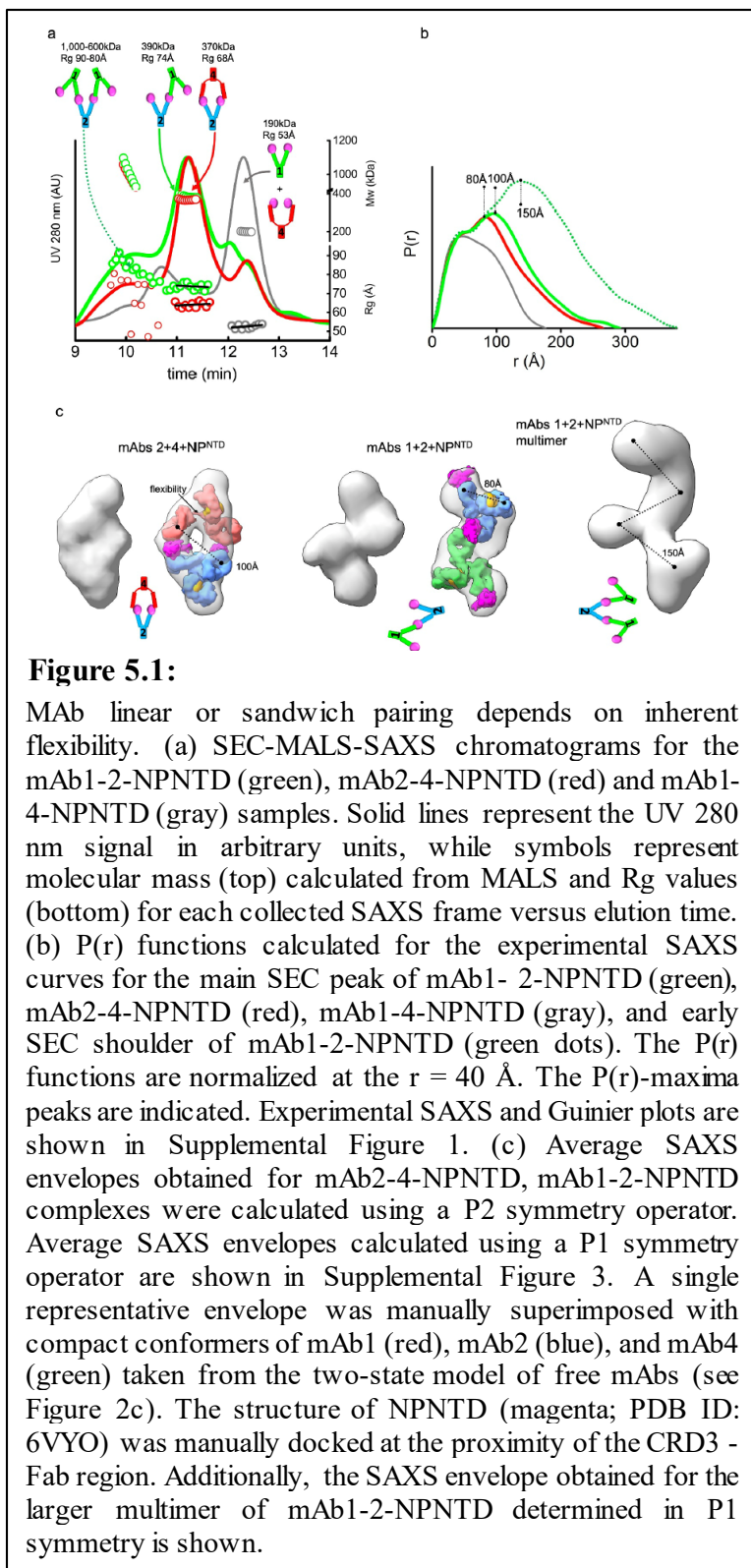


Figure 5.1:

MAb linear or sandwich pairing depends on inherent flexibility. (a) SEC-MALS-SAXS chromatograms for the mAb1-2-NPNTD (green), mAb2-4-NPNTD (red) and mAb1-4-NPNTD (gray) samples. Solid lines represent the UV 280 nm signal in arbitrary units, while symbols represent molecular mass (top) calculated from MALS and Rg values (bottom) for each collected SAXS frame versus elution time. (b) P(r) functions calculated for the experimental SAXS curves for the main SEC peak of mAb1-2-NPNTD (green), mAb2-4-NPNTD (red), mAb1-4-NPNTD (gray), and early SEC shoulder of mAb1-2-NPNTD (green dots). The P(r) functions are normalized at the $r = 40$ Å. The P(r)-maxima are indicated. Experimental SAXS and Guinier plots are shown in Supplemental Figure 1. (c) Average SAXS envelopes obtained for mAb2-4-NPNTD, mAb1-2-NPNTD complexes were calculated using a P2 symmetry operator. Average SAXS envelopes calculated using a P1 symmetry operator are shown in Supplemental Figure 3. A single representative envelope was manually superimposed with compact conformers of mAb1 (red), mAb2 (blue), and mAb4 (green) taken from the two-state model of free mAbs (see Figure 2c). The structure of NPNTD (magenta; PDB ID: 6VYO) was manually docked at the proximity of the CRD3-Fab region. Additionally, the SAXS envelope obtained for the larger multimer of mAb1-2-NPNTD determined in P1 symmetry is shown.

the mAbs' flexibility and how this flexibility affects the assembly of multiple mAbs on an antigen (see **Figure 5.1**). By pairing two mAbs that bind different epitopes on the N-nucleocapsid RNA binding domain, we show that flexible mAbs form a closed sandwich-like complex. With rigid mAbs, a juxtaposition of the antigen-binding fragments is prevented, enforcing a linear arrangement of the mAb pair, which facilitates further mAb polymerization. In a modified sandwich enzyme-linked immunosorbent assay, we show that rigid mAb-pairings with linear polymerization led to increased NP^{NTD} detection sensitivity. These enhancements can expedite the development of more sensitive and selective antigen-detecting point-of-care lateral flow devices, which are critical for early diagnosis and epidemiological studies of SARS-CoV-2 and other pathogens.

5.2.2 Repurpose existing antibodies such as CR3022 (that binds to RBD of SARS-CoV) for SARS-CoV-2 RBD

An antibody, CR3022, which could be effective against SARS-CoV-2 was identified very early during the COVID-19 pandemic. CR3022, originally isolated from a convalescent SARS-CoV (2003) patient, binds to the receptor binding domain (RBD) of the spike protein. While CR3022 has potential to become a diagnostic reagent as well as a promising therapeutic and prophylactic agent against SARS-CoV-2, poorer binding affinity compared to SARS-CoV would have restricted its application. The comparison of the binding affinities of the CR3022 Fab with the RBD and spike protein of SARS-CoV and SARS-CoV-2 showed greater than a hundredfold difference in dissociation constant in favor of SARS-CoV.

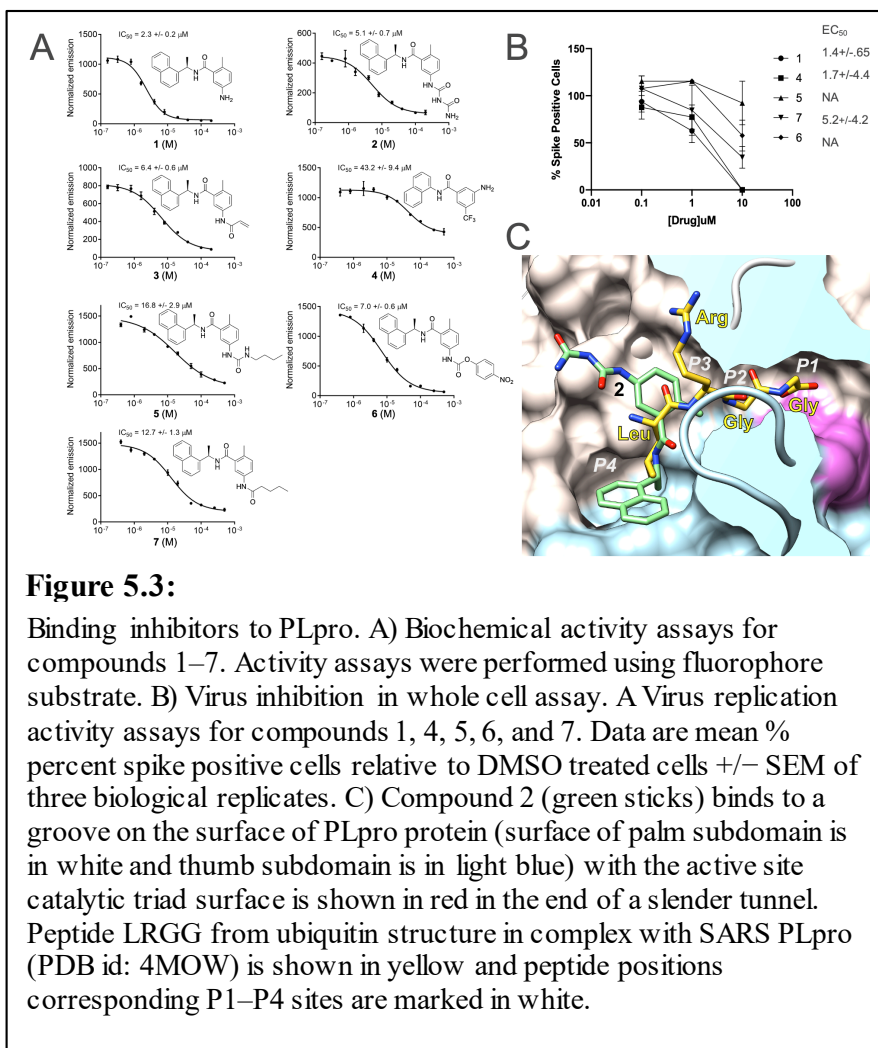
While leveraging various crystal structures of the CR3022, the RBD of SARS-CoV-2 (henceforth called RBD2) and SARS-CoV (henceforth called RBD1) and the complex between the CR3022 Fab and RBD2, we pursued computational and experimental analysis with a goal to improve the binding affinity of CR3022 for SARS-CoV-2. We extracted the light and heavy chains from the complex structure (PDB code 6yla). Concurrently, we also extracted the coordinates of CR3022 from the apo structure (PDB code 6w7y) and of RBD2 from another complex between RBD2 and the human receptor ACE2 (PDB code 6m0j). In our analysis, we performed protein-protein docking between CR3022 (V_L-V_H) and RBD1 and RBD2. Three poses of the CR3022 V_L-V_H with RBD were then relaxed using the ROSETTA fastrelax protocol to remove any clashes introduced due to overlaying or crystal structure imperfections, which were then used as an input for the docking studies. Using the RosettaDock protocol, the V_L-V_H dimer was randomly perturbed around the starting conformation, followed by low resolution centroid mode and finally high resolution all-atom refinement stage to predict a bound pose. The interface score calculated by subtracting the energy of each partner in isolation from the score of the complex was then plotted against the RMSD of the new complex from the input structure. While the input structures derived from the bound complex (6yla) showed stems of the funnel around low RMSD, the other input poses derived from unbound 6w7y CR3022 and 6m0j RBD2 or 6waq RBD1 only showed very weak funnels and pointing to relatively high RMSD. To further analyze the interface, we performed a more rigorous docking study. SnugDock has been specifically developed for antigen/antibody docking. The protocol aggressively samples the CDR loops from the structural database, hence a larger conformational space search is possible.

Papain-like protease (PLpro) is one of two SARS-CoV-2 proteases potentially targetable with antivirals.

PLpro is an attractive target because it plays an essential role in cleavage and maturation of viral polyproteins, assembly of the replicase-transcriptase complex, and disruption of host responses. We report a substantive body of structural, biochemical, and virus replication studies that identify several inhibitors of the SARS-CoV-2 enzyme.

We determined the high-resolution structure of wild-type PLpro, the active site C111S mutant, and their complexes with inhibitors (see **Figure 5.3**). This collection of structures details inhibitors recognition and interactions providing fundamental molecular and mechanistic insight into

PLpro. All compounds inhibit the peptidase activity of PLpro in vitro, some block SARS-CoV-2 replication in cell culture assays. These findings will accelerate structure-based drug design efforts targeting PLpro to identify high-affinity inhibitors of clinical value.

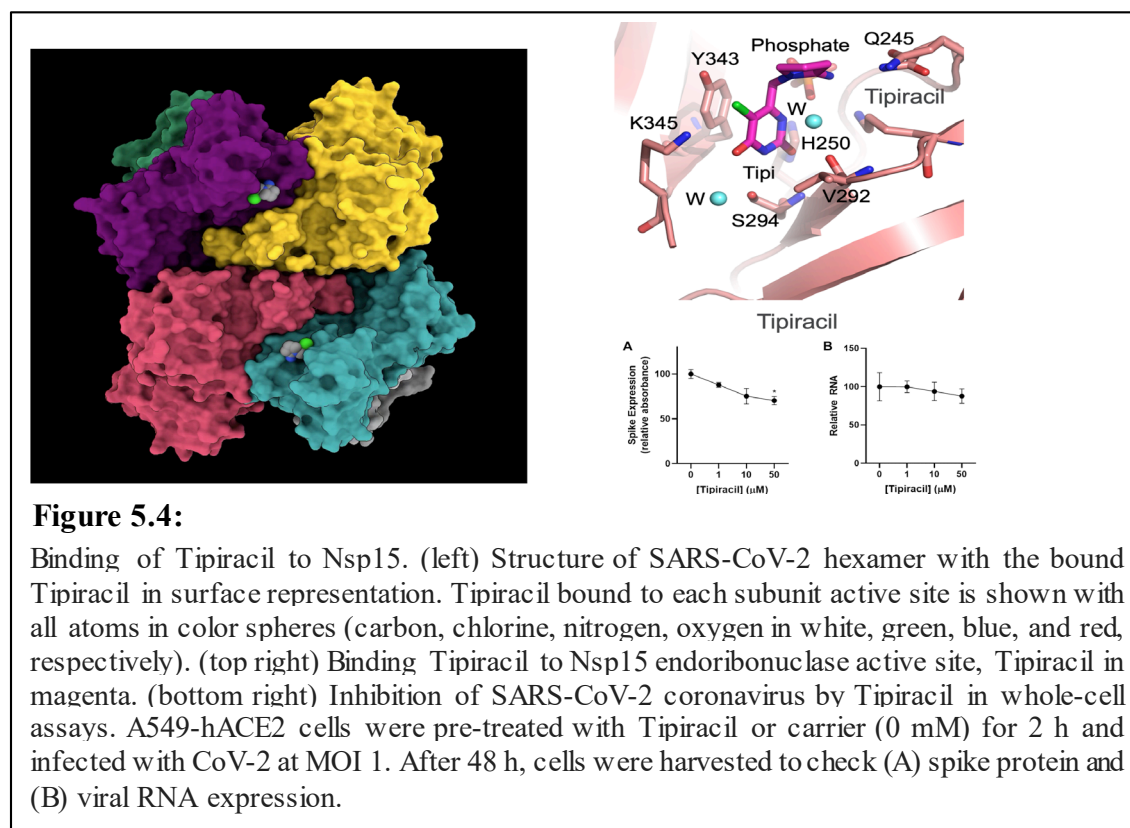


5.2.5 Nsp15 endoribonuclease

SARS-CoV-2 Nsp15 is a uridine-specific endoribonuclease with a C-terminal catalytic domain belonging to the EndoU family that is highly conserved in coronaviruses. As endoribonuclease activity seems to be responsible for the interference with the innate immune response, Nsp15 emerges as an attractive target for therapeutic intervention.

We report the first structures with bound nucleotides and show how the enzyme specifically recognizes uridine moiety. In addition to a uridine site we present evidence for a second base binding site that can accommodate any base. Our structures are consistent with the binding of single stranded nucleic acids, such as loops or bulges. The structure with a transition state analog, uridine vanadate, confirms interactions key to catalytic mechanisms. In the presence of manganese ions, the enzyme cleaves unpaired RNAs.

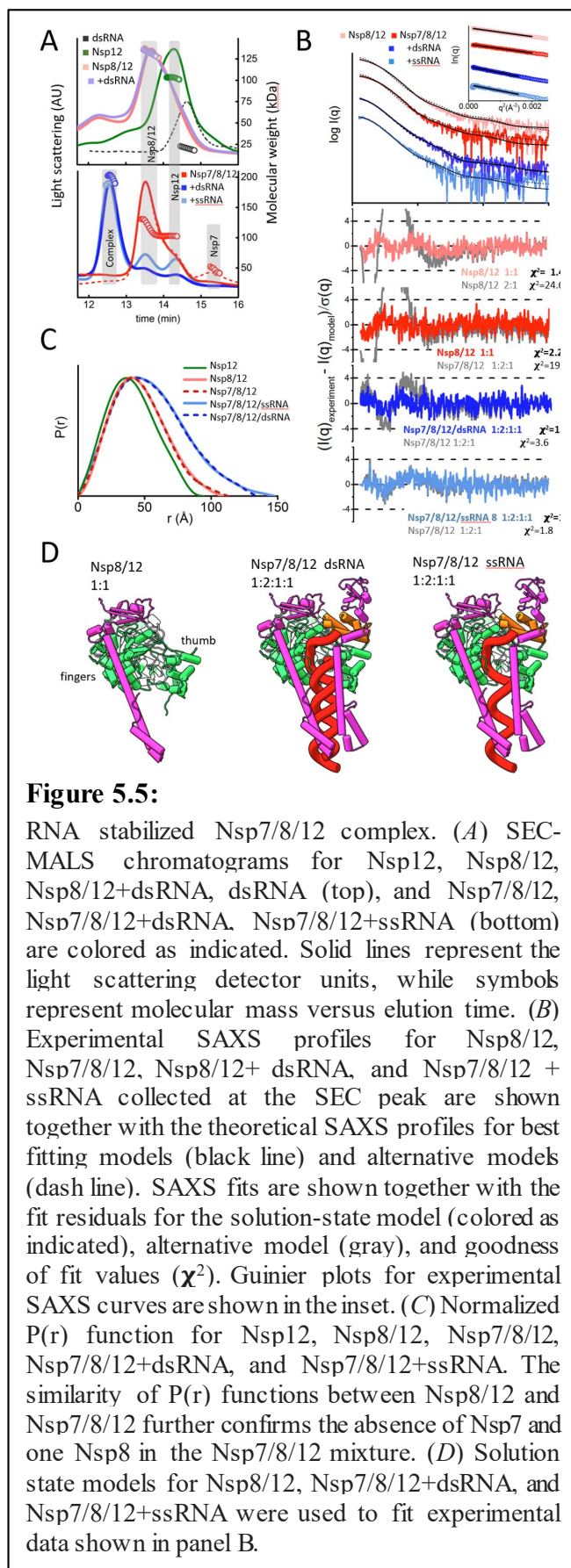
This acquired knowledge was instrumental in identifying Tipiracil, an FDA approved drug that is used in the treatment of colorectal cancer, as a potential anti-COVID-19 drug. Using crystallography, biochemical, and whole-cell assays, we demonstrate that Tipiracil, an uracil derivative, inhibits SARS-CoV-2 Nsp15 by interacting with the uridine binding pocket in the enzyme's active site (see **Figure 5.4**). *In vitro* it inhibits Nsp15 RNA nuclease activity and shows modest inhibition of CoV-2 virus replication in the whole cell assay. While the compound itself is not optimal for the therapeutic applications, our work shows that uracil and its derivatives may represent a plausible starting point for nucleotide-like drug development. Moreover, interaction of Trp333 with bases may provide additional site to build much higher affinity inhibitors. Our findings provide new insights for the development of uracil scaffold-based drugs.



5.2.6 Nsp7/Nsp8/Nsp12 RNA-dependent RNA polymerase complex

The RNA transcription complex (RTC) from the virus, SARS-CoV-2, is responsible for recognizing and processing RNA for two principal purposes. The RTC copies viral RNA for propagation into new virus and for ribosomal transcription of viral proteins. To accomplish these activities the RTC mechanism must also conform to a large number of imperatives including RNA over DNA base recognition, base pairing, distinguishing viral and host RNA, production of mRNA that conforms to host ribosome conventions, interface with error checking machinery and evading host immune responses. In addition, the RTC will discontinuously transcribe specific sections of viral RNA to amplify certain proteins over others. Central to SARS-CoV-2 viability, the RTC is therefore dynamic and sophisticated.

We have conducted a systematic structural investigation of three components that make up the RTC: Nsp7, Nsp8 and Nsp12 (also known as RNA dependent RNA polymerase [RdRp]; see **Figure 5.5**). We have solved high resolution crystal structures of the Nsp7/8 complex providing insight into the interaction between the proteins. We used small angle X-ray and neutron solution scattering (SAXS and SANS) on each component individually as pairs and higher order complexes and with and without RNA. Using size exclusion chromatography and multi-angle light scattering coupled SAXS (SEC-MALS-SAXS) we defined which combination of components form transient or stable complexes. We used contrast matching neutron scattering to mask specific complex forming components to test whether components change conformation upon complexation. Altogether, we find that individual Nsp7,



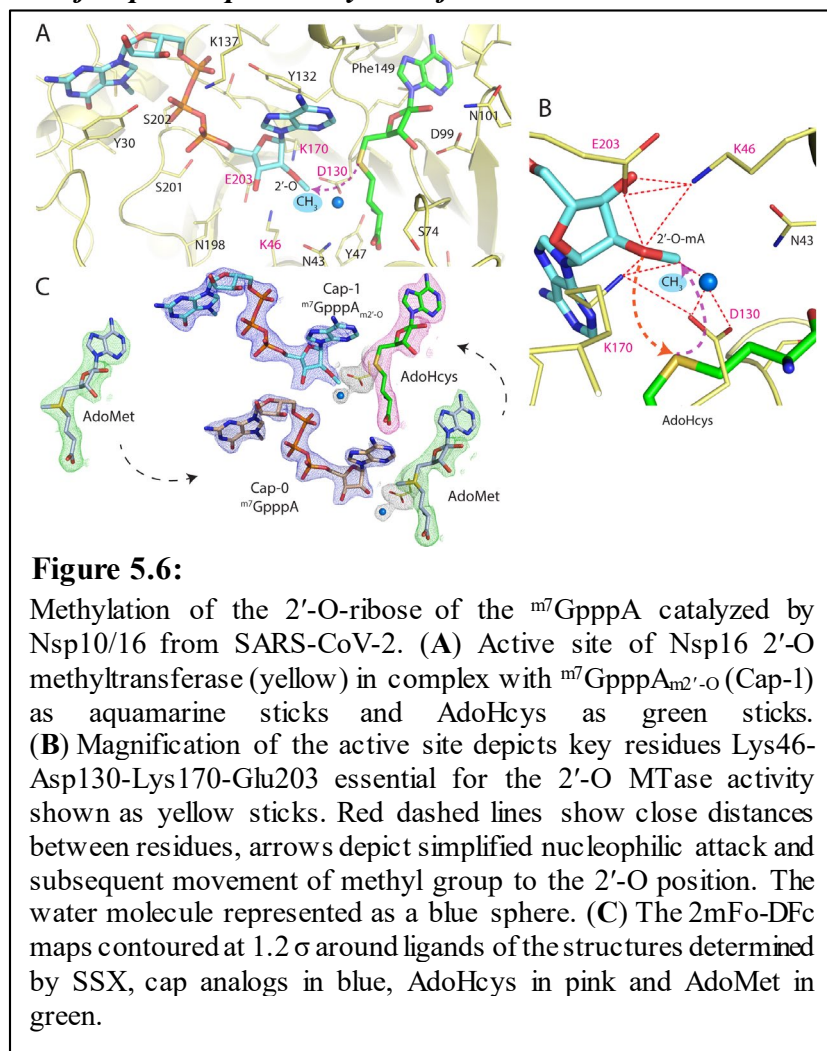
Nsp8 and Nsp12 structures vary based on whether other proteins in their complex are present. Combining our crystal structure, atomic coordinates reported elsewhere, SAXS, SANS and other biophysical techniques we provide greater insight into the RTC assembly, mechanism and potential avenues for disruption of the complex and its functions.

5.2.7 Serial crystallography studies of Nsp10/Nsp16 methyltransferase

The genome of the SARS-CoV-2 coronavirus has a capping modification at the 5' UTR to prevent its degradation by host nucleases. These modifications are performed by the Nsp10/14 and Nsp10/16 heterodimers using S-adenosylmethionine as methyl donor. Nsp10/16 heterodimer is responsible for the methylation at the ribose 2'-O position of the first nucleotide. To investigate the conformational changes of the complex during 2'-O methyltransferase activity, we used a fixed-target serial synchrotron crystallography method at room-temperature. We determined crystal structures of Nsp10/16 with substrates and products that revealed the states before and after methylation, occurring within the crystals during the experiments (see **Figure 5.6**). Here we report

the first crystal structure of Nsp10/16 in complex with Cap-1 analog ($m^7GpppA_{m2'-o}$). Inhibition of Nsp16 activity may reduce viral proliferation making this protein an attractive drug target. The 2'-O methyl group in Cap-1 is essential to protect viral RNA from host interferon-induced response. We determined crystal structures of SARS-CoV-2 Nsp10/16 heterodimer in complex with substrates (Cap-0 analog and S-adenosyl methionine) and products (Cap-1 analog and S-adenosyl-L-homocysteine) at room-temperature using synchrotron serial crystallography. Analysis of these structures will aid structure-based drug design against 2'-O-methyltransferase from SARS-CoV-2.

5.2.8 Model receptor binding domain of (RBD) SARS-CoV-2 spike protein interaction with human ACE2 receptor to gain insights into “hotspot” residues on spike protein that can be targeted



5.2.8.1 Key residues at RBD2-ACE2 interface

To rank the relative importance of each residue at the interfaces of RBD1 and RBD2 with ACE2, we computed the “bound” probability of each pair at the interfaces during the 5- μ s equilibrium simulations. **Figure 5.7** shows a relative ranking of pairs of residues at the interface: high probabilities indicate highly interactive pairs, while low probabilities indicate weakly interacting pairs. To the best of our knowledge, such a complete ranking has not been reported in previous studies, even though calculations of relative changes of interaction energies or free-energies were done for some of the pairs and mutations. **Figure 5.7** shows that both RBD1-ACE2 and RBD2-ACE2 interfaces have almost the same number of interacting pairs. However, if counting stable pairs that have a probability larger than 60% (i.e.,

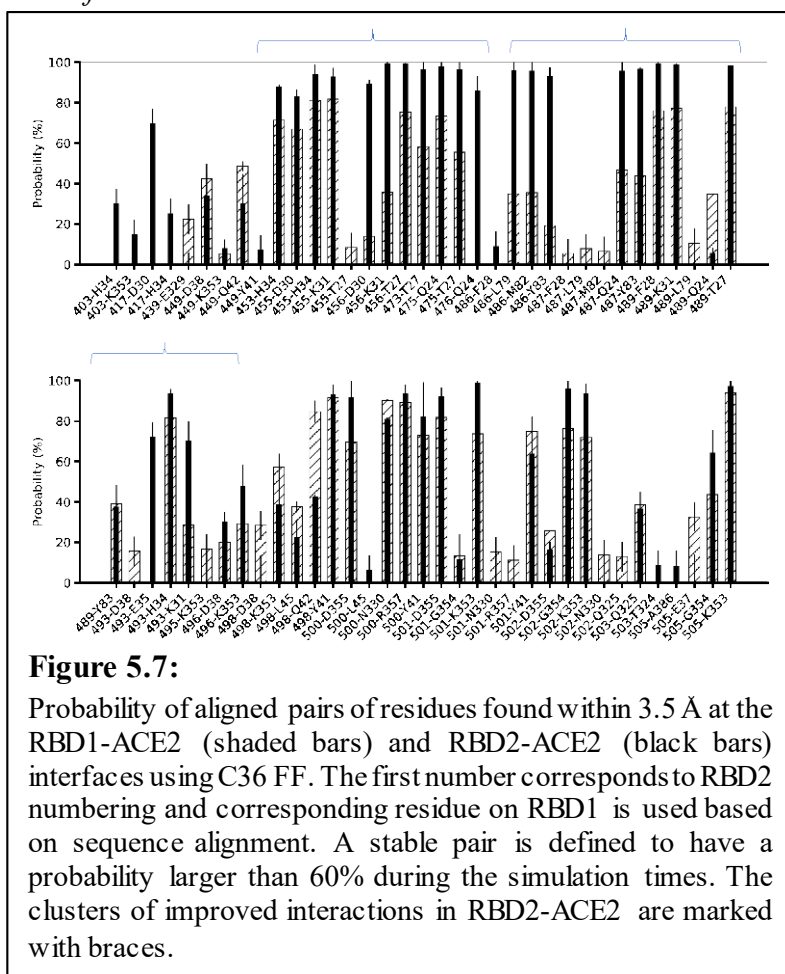


Figure 5.7:

Probability of aligned pairs of residues found within 3.5 Å at the RBD1-ACE2 (shaded bars) and RBD2-ACE2 (black bars) interfaces using C36 FF. The first number corresponds to RBD2 numbering and corresponding residue on RBD1 is used based on sequence alignment. A stable pair is defined to have a probability larger than 60% during the simulation times. The clusters of improved interactions in RBD2-ACE2 are marked with braces.

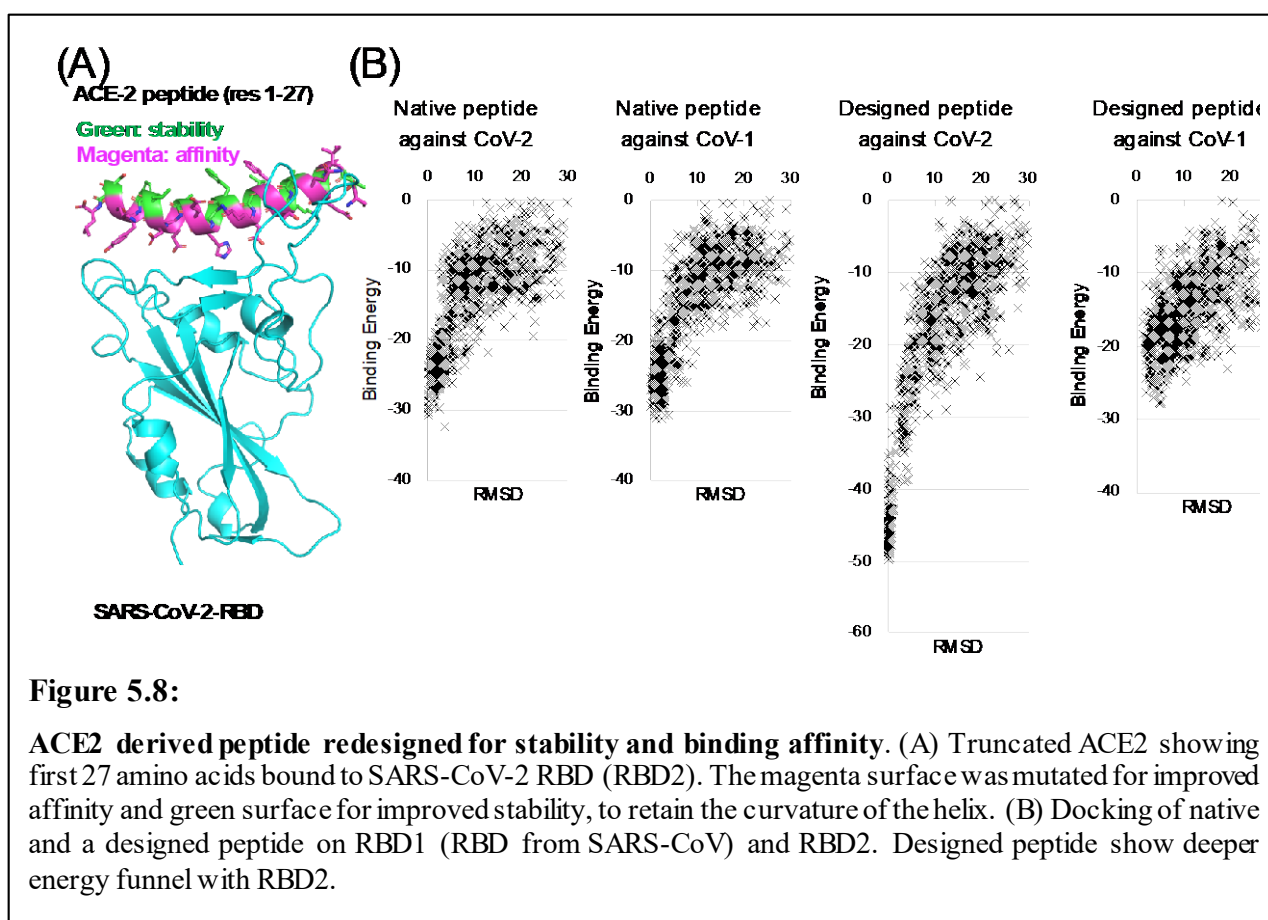
in close contact 60% of the total simulation time), there are only 22 ± 2 pairs in the RBD1-ACE2 interface, while RBD2-ACE2 showed substantially higher with 35 ± 1 stable pairs at the interface. Among these stable pairs, the mutations from RBD1 to RBD2, namely, Y455L, L456F, Y498Q, T501N and L486F appear to noticeably enhance the probabilities of interaction with the residues of ACE2 with multiple pairs having probabilities close to 100%. The brackets in **Figure 5.7** indicate two groups of neighboring residue clusters that have a substantial increase in interactions in the RBD2-ACE2 interface compared to the similar clusters in the RBD1-ACE2 interface. This suggests that they are key residues that differentiate the RBD2-ACE2 binding interface from the RBD1-ACE2 binding interface.

To probe whether the use of a different force field may change the outcomes of the key residues in the interfaces, we compared the probabilities with those obtained from the simulations using modified AMBER ff99SB FF performed by the Shaw group. We found that regardless of the FFs, the RBD2-ACE2 interface shows stronger inter-molecular interactions than the RBD1-ACE2 interface involving the same group of residue positions (**Figure 5.7**). The clusters of the important residues are consistent with the finding that residues L455 and F486 and N501 of SARS-CoV-2 are perhaps the most critical residues that increase the interactions between RBD2 and ACE2 in comparison with the interactions between RBD1 and ACE2 with Y455, L486 and

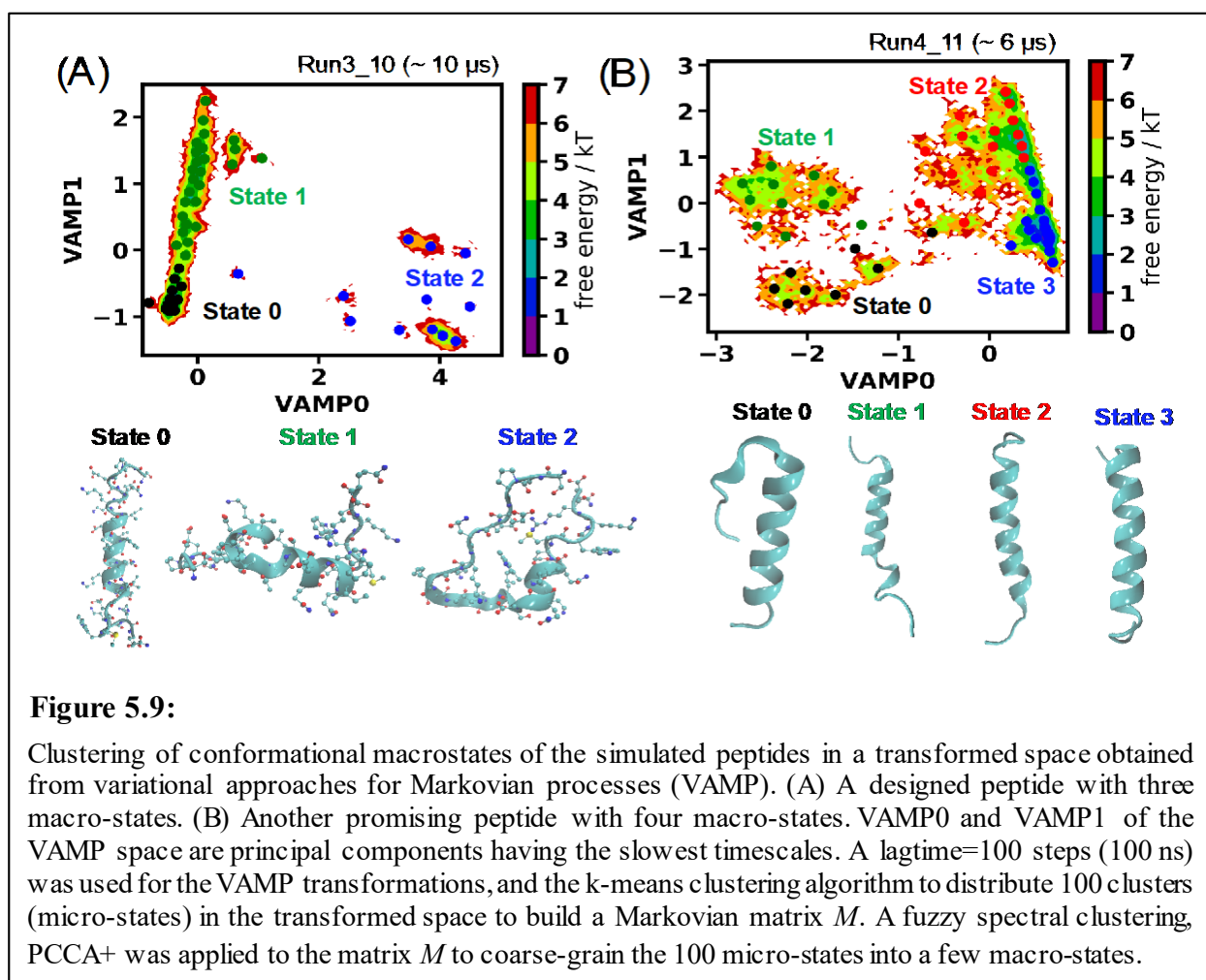
T501 residues on RBD1. New residues such as K417, Y473 and A475, which were not reported earlier but proposed to be important in others work, emerged to be important for RBD2-ACE2 interface and enhanced the interaction compared to RBD1-ACE2 with V417 and P475 residues. Particularly, the V417K mutation created a salt-bridge with D30 (on ACE2), thus contributing to an increase in the electrostatic interactions and compensating for coulomb energy due to mutation R439N and loss of distal R439-E329 electrostatic interaction (seen in RBD1-ACE2 interface).

5.2.8.2 Explore and design novel binders for RBD

With an available crystal structure of ACE2 and RBD2, an approach was to design and test minimal sized peptide that can bind to the RBD2 and block interaction with the ACE2 receptor. Our preliminary study using molecular dynamics simulation showed that the peptide consisting of first 30 amino acids is unstable and would collapse or unfold. Using Rosetta, we took the first



27 amino acids (even smaller than our previously chosen sequence) and redesigned for higher affinity (magenta surface, **Figure 5.8A**) and improved stability (green surface, **Figure 5.8A**). The redesigned peptides were then tested for binding energy funnel and showed improved binding only for RBD2 (**Figure 5.8B**). Binding affinity for RBD1 was in fact marginally disrupted in some of the designed peptides, hence improving the specificity of the designed peptides. Further, the peptides were also evaluated for stability using long timescale molecular dynamics simulations. The native peptide (res 1-27) showed very low stability. Contrary to that, the designed peptides showed high stability and retained helical structure (**Figure 5.9**). A total of



66 peptides were displayed on yeast cell surface and tested for binding to RBD2-sfGFP. While we were able to show display of the peptides on the yeast surface using c-myc tag expressed at the C-terminus of the peptide, at a low micromolar concentration range of the target RBD2-sfGFP, we failed to see any binding. While it is very likely that the stability of the designed peptides improved, it is also very likely that the peptide does not preserve the right curvature/conformation to present interfacial residues to the RBD2. Further work will be needed to understand the structural perturbation in a single helical peptide which can have detrimental effect on the binding affinities. We also expect that use of RBD2 at higher concentrations (>20 uM) could show detectable binding affinities, and would help compare the designed peptides with the native one.

A total of 66 peptides were displayed on yeast cell surface and tested for binding to RBD2-sfGFP. While we were able to show display of the peptides on the yeast surface using c-myc tag expressed at the C-terminus of the peptide, at a low micromolar concentration range of the target RBD2-sfGFP, we failed to see any binding. While it is very likely that the stability of the designed peptides improved, it is also very likely that the peptide does not preserve the right curvature/conformation to present interfacial residues to the RBD2. Further work will be needed to understand the structural perturbation in a single helical peptide which can have detrimental effect on the binding affinities. We also expect that use of RBD2 at higher concentrations (>20 uM) could show detectable binding affinities, and would help compare the designed peptides with the native one.

Task 6: Next-Generation Rapid Testing (Phase 2 – Next Gen Task 1)

Institutions: SNL, LANL, ORNL, ANL, LLNL, PNNL, and Ames

Lead PI: Robert Meagher

The next-generation testing R&D team performed research pertaining to the following two aims:

1. Developing novel methods for concentrating viruses from dilute sample matrices
2. Developing highly sensitive and specific assays that would be suitable for rapid screening outside of a laboratory setting.

6.1 Highlights

- ORNL developed a novel breath sampling device for non-invasive COVID sampling and concentration of virus from breath.
- LLNL developed a portable reader for colorimetric RT-LAMP assays for COVID.
- SNL piloted freeze-drying of RT-LAMP reagents and tested methods for virus concentration from dilute samples. The freeze-drying work has fed into a CRADA for a
- PNNL and AL worked on aptamer-based detection assays.
- LANL tested methods for developing ultrasensitive quantum dot-based immunoassays.
- ANL tested protocols for RT-LAMP detection in droplets, and provided key reagents to other laboratories.

6.2 Inter-lab collaborations

- SNL, LLNL, and SLAC collaborated on a review article on point-of-care diagnostics using LAMP, with a special focus on COVID-19 LAMP assays.
- ORNL shared protocols for agarose gel matrices as a substrate for other laboratories to test detection assays.
- ANL shared reagents including anti-RBD antibodies with PNNL and SNL.
- PNNL and AL shared knowledge on aptamer-based assays.
- SNL, LLNL, and ANL shared knowledge on LAMP assays.

A multilab publication resulted from work funded by this task: Taylor J. Moehling, Gihoon Choi, Lawrence C. Dugan, Marc Salit & Robert J. Meagher (2021) “LAMP Diagnostics at the Point-of-Care: Emerging Trends and Perspectives for the Developer Community”, *Expert Review of Molecular Diagnostics*, 21:1, 43-61, DOI: 10.1080/14737159.2021.1873769

6.3 Impacts and follow-on work

- ORNL has filed a joint invention disclosure on the breath sampling “whistle” device.
- SNL’s reagent stabilization work helped inform an NIH RADx-sponsored CRADA project with a small business (VIC Foundry) to develop a home-based molecular COVID-19 test.
- LLNL has received inquiries for licensing the Reveal-CoV instrument.

- ANL's Spike-RBD and antibody work continues in the NIAID structural biology center (CSGID)

6.4 ORNL Breath Sampling “Whistle” (focus on Aim 1)

ORNL's work evolved to focus on the capture of viral particles from aerosols in exhaled breath using a ‘whistle’ that is loaded with a hydrogel material designed to capture aerosol as a patient blows into the whistle for a set duration and volume (Figure 6.1). To date they have produced 100s of whistles using 3D printers within the Nanofabrication Research Lab and Macromolecular Nanomaterials groups at the Center for Nanophase Materials Science, and have sent these to the University of Tennessee Health Science Center for testing with patients. UTHSC has Institutional Review Board approvals in place and is doing work on site to analyze the hydrogels as they are used alongside nasal swab tests. **A joint invention disclosure has been submitted.**

The whistles have a tone and volume that modulates based on breathing rate so that it is possible to consistently monitor duration and rate of exhalation. The loading of agarose hydrogels into the bottom portion of the whistle did not negatively impact the tone or volume of the whistle during operation. It was determined that a 4% agarose solution (~400 microliters) could be readily added to the ‘bottom’ of the whistle and easily rinsed with buffer to remove adequate amounts of virus for analysis by PCR or sequencing. These agarose hydrogels have been used in all patient testing.

Engineering of structured hydrogels and optimization of those hydrogels is a primary focus. ORNLs expanded beyond the basic agarose hydrogels used in the UTHSC partnership and



Figure 6.1:
(Top) A 3D CAD rendering of the ‘whistle’ show is the location where the hydrogel is added. The hydrogel can be readily removed for testing. (Bottom) ‘Whistles’ were 3D printed for testing, with modifications being made for to improve ease of use and handling based on feedback during patient testing.

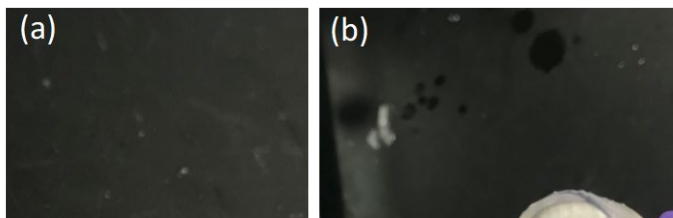


Figure 6.2:

(a) Lattice structures of printed hydrogels and solid supports coated with hydrogels were created and (b) placed within the whistle. Lattices did not interfere with the operation of the whistle. Ongoing modeling and testing are being done to determine the impacts of surface topography, chemical composition, and airflow on pathogen capture.

determined how the topography, porosity, and surface chemistry of the capture material can be tuned to improve capture and release of breath generated aerosols for introduction into a lateral flow assay or another analytical platform. The geometry, topography and chemistry of the material can be tuned to optimize

capture and subsequent release. Due to the limits in printing resolution and stability of available formulations of hydrogels. It was determined the printing a lattice from a conventional 3D printing resin and coating that lattice with hydrogel formulation was the most cost effective and flexible approach for introducing highly structured hydrogels into the ‘whistle’ (Figure 6.2). A laboratory system for testing the flow and capture of particles in the ‘whistle’ has been setup and is being used to test the capture of aerosols in different designs (Figure 6.3).

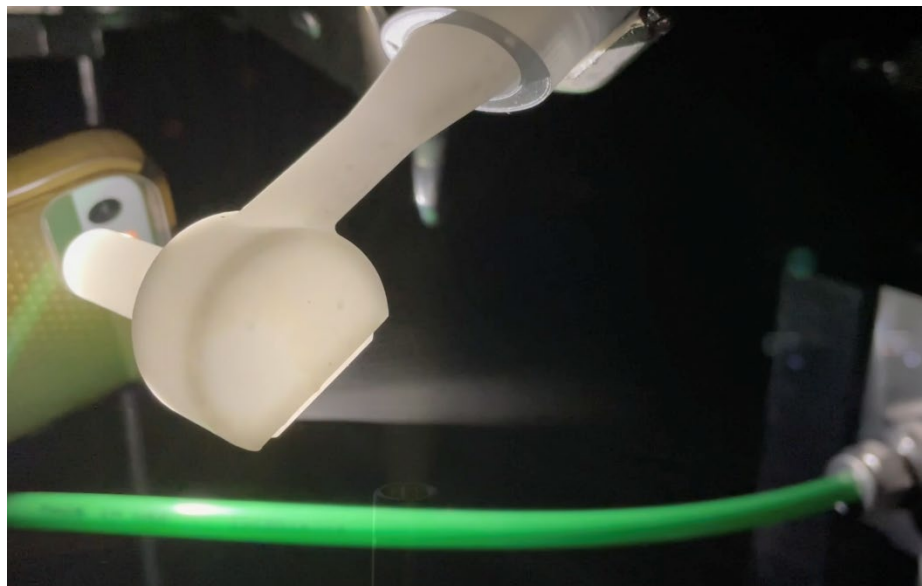


Figure 6.3: Laboratory testing using an atomizer was initiated to visualize flow and particle capture was initiated and is still underway. Laboratory testing was performed using aqueous aerosols with colored and fluorescent dyes or particles in water.

6.5 LLNL Reveal-CoV instrument for point-of-care diagnostics (focus on Aim 2)

LLNL designed and built a rapid, RT-LAMP-based molecular diagnostics platform as a potential tool to quickly diagnose COVID-19 in under one hour. This point-of-care testing approach involves an initial high temperature swab sample inactivation step followed by amplification of viral RNA using up to 5 control and pathogen-specific assays. Results are determined based on a discreet reaction color change from red to yellow but can also be determined using fluorescence detection. Testing of this prototype platform was conducted with synthetic viral RNA and dried, stabilized reagents. Buffer systems, swab selection, and assay stabilization formulations were evaluated for performance. Limits of detection were determined using RNA; however, testing was not performed with viable SARS-CoV-2 virus or clinical samples.

Figure 6.4 shows the prototype instrument (left) developed to inactivate a sample in the Stage 1 heater and test for viral RNA with a single, pathogen-specific assay in Stage 2. The Stage 1 heating cycle required ~12 min to heat from RT to 95°C, maintain 95°C for the required 5 min and then cool to a safe handling temperature below 45°C. Stage 2 heating is isothermal at 65°C for 30 min and requires ~40 min from heat up to cool down to safe handling temperature.



Figure 6.4: Reveal-CoV instrument development. Left: First unit build of prototype single assay instrument consisting of two single-tube heaters for sample inactivation (Stage 1) and detection assay amplification (Stage 2). Right: CAD model of 5 assay instrument concept consisting of a sample inactivation heater (Stage 1) and a 5-tube detection assay heater (Stage 2).

A redesigned instrument concept model is shown in Figure 6.4 on the right. The redesign incorporates a 5-tube heating block in Stage 2. This design change was pursued to allow us to incorporate additional assays into testing for improved specificity and potentially reduced limits of detection. Additionally, this redesign could allow testing against other pathogens, the use of independent control reactions and potentially incorporation of fluorescence detection.

Several key test parameters were studied to demonstrate improved test sensitivity and performance. Heat lysis/viral inactivation of samples was incorporated into the testing scheme based on testing performed on a surrogate human coronavirus, NL63. A 5 min hold at 95°C improved colorimetric detection ~10-fold as shown in Figure 6.5 left. Selection of sampling swabs is critical such that the swab material does not interfere with the initial or final reaction color (Figure 6.5 center). Finally, the use of positive and negative controls along with three virus-specific assays provides added confidence that the testing performed as expected (Figure 6.5 right).

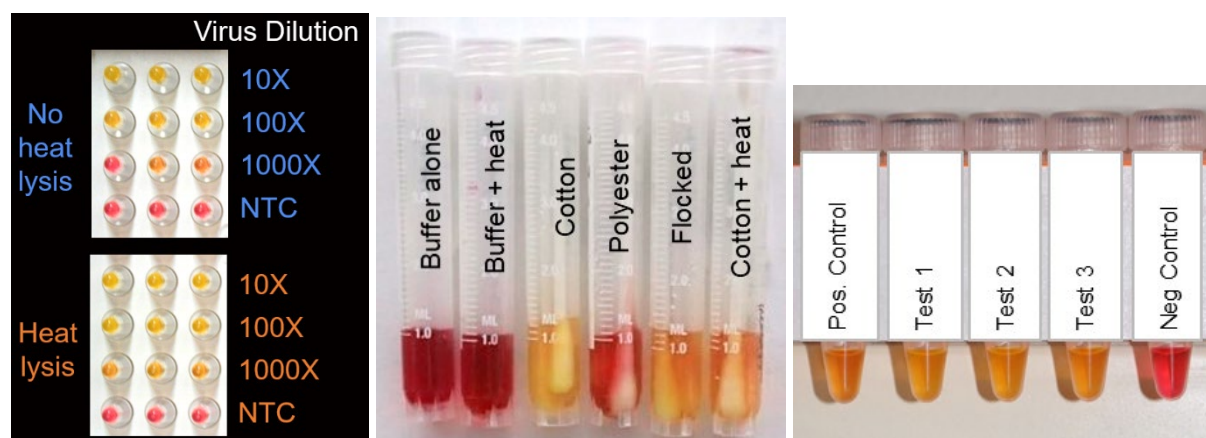


Figure 6.5: Reveal-CoV test parparameter development. Left: A pre-amplification heat lysis/sample inactivation step improves colorimetric endpoint detection ~10-fold Center: Commercial swabs were evaluated to identify products with minimal effect on reaction color. Right: A panel of 5 assays, including positive and negative controls and 3 virus-specific assays, were selected for optimal test performance.

6.6 SNL stabilization of RT-LAMP reagents (Aim 2)

Sandia performed work related to Aim 1 to concentrate virus from dilute samples, although that work is ongoing and data is not presented here. Pursuant to Aim 2, the goal of this work was to determine the stability of reverse transcription loop-mediated isothermal amplification (RT-LAMP) reagents, lyophilized by a commercial service provider. Our goal is to provide a data set and recommendations that would be generally useful to the LAMP developer community, since reagent stabilization is critical to point-of-need assays, but is rarely described in any detail in open literature. The RT-LAMP assay was designed at SNL and consists of three primer sets: two targeting distinct genes in the SARS-CoV-2 genome and one targeting human genomic DNA (assay control). The assay incorporates SNL's patented end-point fluorescence detection mechanism called QUASR or quenching of unincorporated amplification signal reporters. This method incorporates a dye-labeled primer and a quencher-tagged probe. After the 45-minute reaction, the solution is cooled to ambient temperature, resulting in dark quenching of fluorescent primers in negative samples and highly fluorescent amplicons in positive samples. We also track amplification in real-time by adding an intercalating dye.

RT-LAMP reagents were lyophilized, or freeze-dried, by our collaborator BIOLYPH and packaged with desiccant in airtight pouches. BIOLYPH used three proprietary excipients to stabilize the enzymes during the freeze-drying process. First, we tested the sensitivity of the lyophilized samples (three excipient groups for each primer set) using various concentrations of RNA and compared the results to freshly prepared reagents. After analyzing the data for all three primer sets, two excipients enabled the lyophilized samples to perform similarly to the fresh reagents. Moving forward, we only utilized samples lyophilized with these two excipients. We then evaluated the lyophilized reagents using inactivated SARS-CoV-2 virus as template and saw excellent amplification even at low concentrations of virus. Finally, we explored the performance of the lyophilized samples using inactivated virus spiked in 10% human saliva to better mimic a clinical diagnostic test. Our sample pretreatment process included chemical inactivation (using TCEP and EDTA) of RNases commonly found in saliva and a heating step (95°C for 5 min) to

promote viral lysis. The sensitivity with the lyophilized reagents (both excipients) coincided with the results from the fresh controls.

In the next portion of the project, we assessed the long-term stability of lyophilized RT-LAMP reagents. Lyophilized samples (two excipient groups for each primer set) were stored in airtight pouches containing desiccant at both 22°C and 45°C. After one month, the lyophilized reagents were reconstituted with RNA template and compared to freshly prepared samples. At the lower storage temperature (22°C), lyophilized reagents behaved similarly to the fresh controls (Figure 6A). We noticed slower amplification in real-time for the lyophilized samples stored at the elevated temperature (45°C) (Figure 6B) but this did not seem to affect end-point fluorescence measurements. We repeated this experiment after 3 months of storage. The lyophilized reagents were able to successfully detect target RNA even after extended storage at 22°C. Alternatively, lyophilized samples held at 45°C for 3 months showed very little amplification, even at high RNA concentrations. This indicates that there was significant loss in enzyme activity and the lyophilized reagents cannot tolerate 45°C for more than 1 month. It is worth noting that it is unlikely that lyophilized samples would experience temperatures as high as 45°C for any length of time.

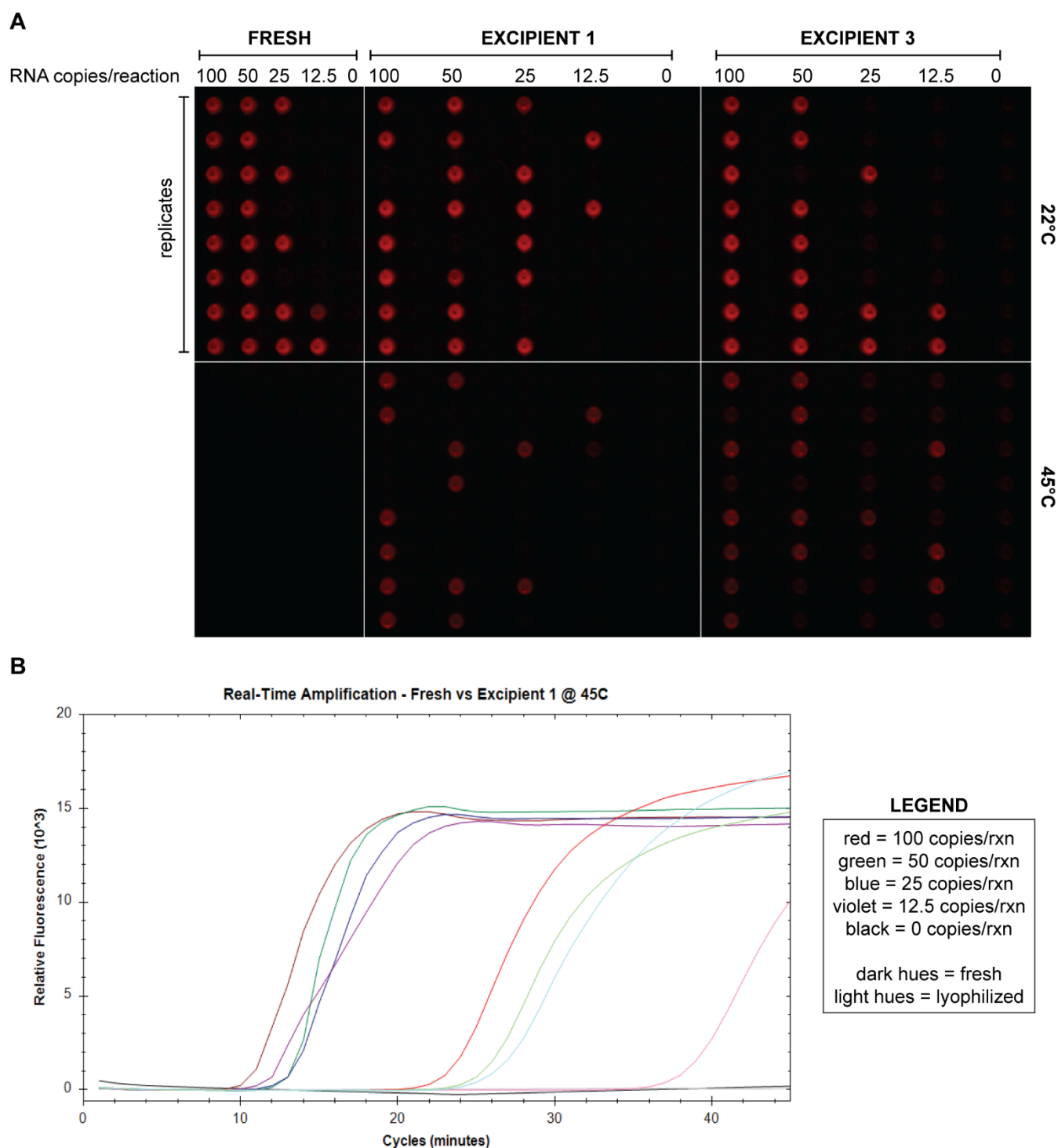


Figure 6.6: Storage of lyophilized reagents for one month. (A) End-point fluorescence demonstrates that reagents lyophilized with both excipients amplify RNA template comparably to fresh controls when stored at 22°C; however, when stored at an elevated temperature (45°C), fewer of the replicates amplify. (B) Real-time fluorescence of representative replicates for both fresh controls and lyophilized reagents with excipient 1 stored at 45°C. There is a clear delay in time to amplify for the lyophilized reagents (light hues) when compared to the fresh controls (dark hues).

6.7 ANL: Alternative molecular diagnostics and protein reagents (Aims 1 and 2)

During this project the ANL team has focused on developing alternative molecular diagnostic tools and provide reagents to collaborators.

Alternative RT-qPCR protocol. The mainstream SARS-CoV-2 RT-qPCR-based diagnostic protocol uses predefined primer sets and associated Taqman probe. The ANL team has developed alternative primer sets using the *nsP1* and nucleocapsid genes and identified several primer sets that can be used with conventional intercalating dyes to obtain similar sensitivity and specificity to the commercial Taqman-based method. The assay price is significantly lower and the freedom of selecting alternative primer sets avoids restrictions that DNA oligo synthesis companies placed on sequences that were highly similar to the commercially used probe sets. The ANL team has also demonstrated the feasibility of obtaining high quality RNA standards for the RT-qPCR assays using a plasmid template and the NEB HiScribe® T7 High Yield RNA Synthesis Kit. The ANL RNA standard was calibrated against the commercial RNA standard and used in all assay development efforts. The in-house generated RNA is < 10,000 times cheaper than the commercial one.

LAMP assay. The ANL team has tested the LAMP assay with probe sets described in the literature for SARS-CoV-2 detection. Both the fluorophore and colorimetric dyes were tested for detection using the in-house RNA standard. The ideal temperature and reaction times were optimized using a BioRad CFX-384 touch instrument. The optimized assay was then tested with low-cost Mini-PCR instrument and demonstrated that the assay was able to detect ~ 100 copies of RNA per reaction confidently using the colorimetric substrate. The RNA was also detected from saliva when an intermediate purification process was employed. The LAMP assay was tested in microfluidic droplets. Several surfactant and fluorinated combinations were tested, which were used in the laboratory for droplet PCR, droplet assays, and other biological experiments. Unfortunately, the droplets were unstable when using the commercial LAMP reagents (NEB). The reaction optimization with lowered detergent concentrations was not pursued.

Protein reagents. The ANL team has expressed the SARS-CoV-2 Spike-RBP protein in HEK-293 cells and purified it with high homogeneity for distribution to many labs and local ANL efforts. In addition to the pure protein, biotinylated forms were also distributed for other users. The biotinylated form was used at ANL for characterization of mAbs, Fabs, and nanobodies. The team has also purified and distributed the CR3022 mAbs to the NVB network.

6.8 PNNL aptamer magnetic nanoparticle assay (Aims 1 and 2)

PNNL's work toward developing a next generation Covid-19 test focused on using a single-stranded DNA aptamer (COV2-RBD-1C) to recognize and bind the receptor binding domain (RBD) of the SARS-CoV-2 Spike glycoprotein.

The first aim was to capture and concentrate the virus from saliva samples using magnetic nanoparticles (MNPs) (Figure 6.7A). PNNL made progress toward this goal by capturing RBD protein from aqueous solution. First, PNNL functionalized the surface of commercially available MNPs with aptamers using streptavidin-biotin chemistry and characterized the aptamer loading using flow cytometry to show successful co-localization of the MNP fluorescence and the

fluorophore-conjugated aptamer (Figure 6.7B). Next a polyhistidine-tagged RBD protein (produced and purified by Dr. Babnigg at Argonne National Laboratory) was incubated in a solution of aptamer-functionalized MNPs. The MNPs were pulled from the solution using an externally applied magnet, redispersed in fresh buffer, and then tested for RBD protein using a his-tag competitive ELISA kit. Results from the his-tag ELISA suggest that increasing the aptamer bound to the surface of the MNPs increases the amount of RBD detected in the assay (as indicated by a decrease in absorbance) for larger quantities of protein (592ng or 1.48 μ g/mL, Figure 6.1C). Due to the nonlinear standard curve for RBD protein from the ELISA, an absolute quantity of RBD captured could not be determined. A micro-bicinchoninic acid test was tried as a secondary method for quantifying captured RBD, but the streptavidin-coated MNPs interfered with this method's results.

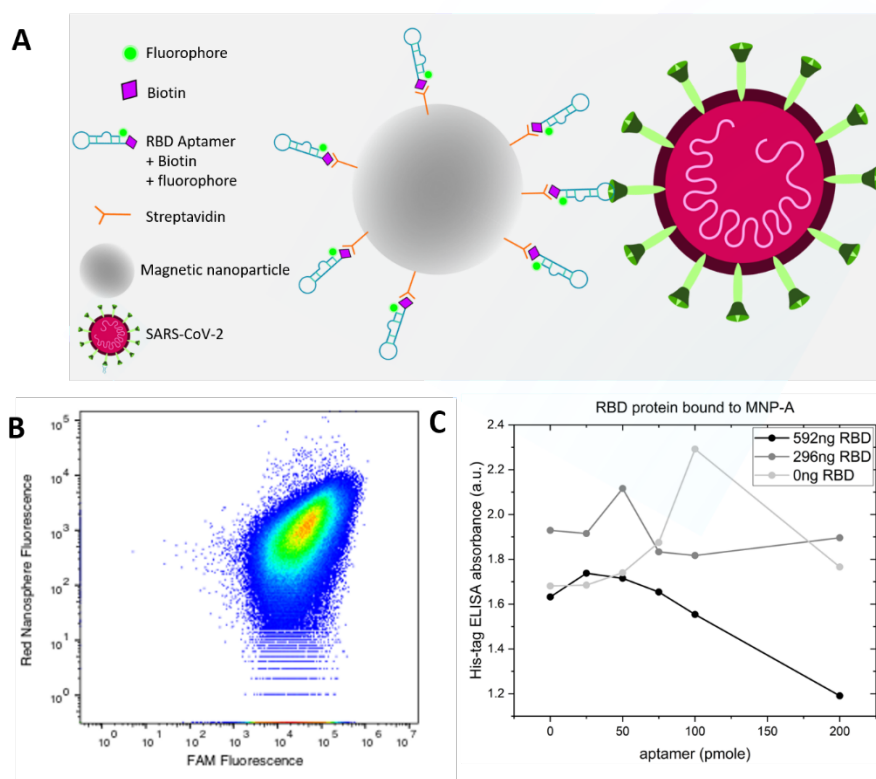


Figure 6.7: (a) An illustration shows the mechanism behind aptamer-functionalized MNP capture of SARS-CoV-2. (b) Flow cytometry confirmed successful MNP surface functionalization with aptamer. (c) Results from his-tag ELISA show decreasing absorbance with increased aptamer loading for the highest tested concentration of RBD (592ng or 1.48 μ g/mL) suggesting RBD was captured by the MNPs.

The second aim of PNNL's work was to develop a colorimetric assay to detect SARS-CoV-2 using the COV2-RBD-1C aptamer for SARS-CoV-2 molecular recognition and gold nanoparticles (AuNPs) as a peroxidase enzyme mimic. The theory behind this assay (previously demonstrated for norovirus detection) is that, in the presence of H₂O₂, AuNPs catalyze the oxidation of a 3,3',5,5'-Tetramethylbenzidine (TMB) substrate to create a blue colored solution. This reaction can be prevented by passivating the surface of the AuNPs with the aptamers which cling to the gold surface via static interaction. When the SARS-CoV-2 virus is introduced, the

aptamer can bind to the Spike glycoprotein RBD, and free the surface of the AuNP to catalyze the TMB oxidation (Figure 6.8A). PNNL optimized the peroxidase ability of citrate-capped AuNPs (Figure 6.8B) and achieved a 37% reduction in TMB oxidation by passivating the surface of the AuNPs with up to 200pmole of aptamer (Figure 6.8C). The colorimetric assay was then tested with gamma-irradiated inactive SARS-CoV-2 (BEI Resources) and the Vero E6 cell lysate control (BEI Resources).

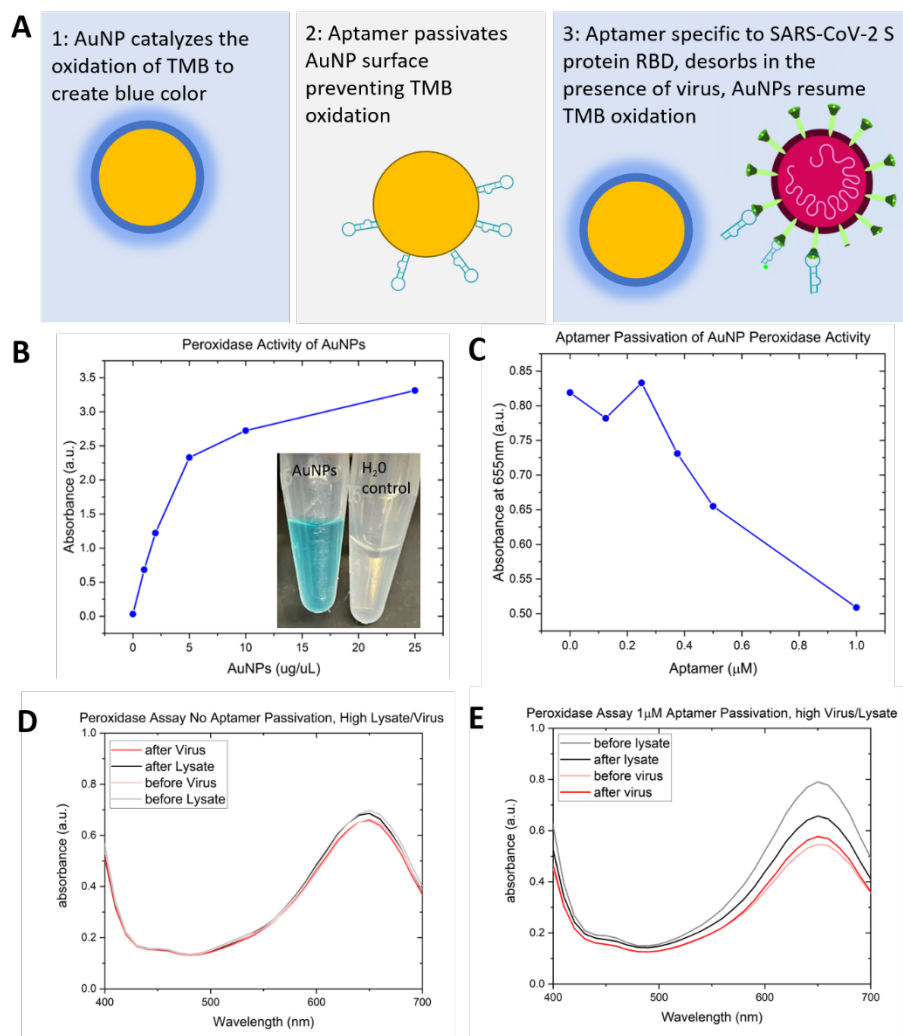


Figure 6.8: (a) Schematic describing theory behind colorimetric detection assay. (b) Peroxidase activity of AuNPs was optimized to create a strong colorimetric response. (c) a 37% reduction in peroxidase activity was achieved by passivating the AuNP surface with aptamer. (d) No change in 655 nm absorbance was observed before or after lysate or virus addition for the zero-aptamer passivation experiment. (e) A modest 5.2% increase in 655nm absorbance was observed after adding inactivated SARS-CoV-2 to the 1 μM aptamer passivated assay.

Both virus and cell lysate samples were dialyzed to prevent salt-induced AuNP aggregation from the background cell culturing media. For non-passivated AuNPs (no aptamer), the assay's 655nm absorbance peak was not significantly different before or after the addition of cell lysate control or virus samples (Figure 6.8D). For passivated AuNPs (1uM aptamer) only a modest increase

(5.2%) in absorbance was observed for the highest concentration of virus tested (2.8×10^5 TCID₅₀ per mL) which was not visible by eye (Figure 6.8E). Further optimization would be required to lower the detection limit and increase the colorimetric response; however, future work should focus on detecting active SARS-CoV-2 or pseudovirus, as it is possible that the Spike glycoprotein RBD could have been damaged in the viral inactivation process, making binding and detection by aptamer less effective.

6.8 Ames nanoporous alumina sensor (Focus on Aim 2)

With the purpose of developing a sensor to detect SARS-2 virions, we started with an available model system and in parallel we tested the components necessary to detect SARS-2 virions. The model system was vesicular stomatitis virus (VSV) virions tagged (pseudotyped) with the Ebola virus glycoprotein (GP1,2). An electrochemical sensor consisting of a nanoporous alumina membrane functionalized with an aptamer that recognizes GP1,2 with high affinity was tested for its ability to detect virions using ebola glycoprotein labeled VSV virions (EBVSV).

To develop the sensor, anodized alumina membranes with nominal pore-size of 20 nm were coated with gold films and thiolated aptamers were immobilized on the gold-coated alumina membranes. A thus functionalized membrane was mounted in an electrochemical cell filled with phosphate saline as electrolyte. A four-electrode configuration was used to monitor the impedance changes across the membrane during exposure to different densities of suspended virions. Two sets of experiments were performed: 1) to determine the minimum particle density detected by the sensor, and 2) to determine the ability to selectively detect the targeted virion (in this case EBVSV) in the presence of other virions with the total virion density being constant.

The first set of experiments showed that the sensor can detect densities higher than 500 virions/mL. Specificity was demonstrated because membrane impedance decreased on exposure to EBVSV virions but exposure to VSV virions produced either no-change or an increase in membrane impedance. The second set of experiments showed that with densities of 1000 virions/mL, a specific sensor response was recorded with EBVSV virions as 12% of the total. These results demonstrated that aptamer-functionalized sensor could detect the presence of virions in the presence of higher concentrations of similar particles but lacking the ebola GP1,2 protein for which the aptamer is specific.

In addition to the sensing experiments, we designed a frequency analyzer chip-based reader for continuous monitoring of membrane impedance. The chip-based reader replaces laboratory potentiostat in the sensing experiments and can reduce the sensing system cost from \$15000 to few hundred dollars.

In parallel with development of the sensor for detecting virions using the surrogate ebola aptamer, we tested the affinities of aptamers isolated to the SARS-2 receptor binding domain to bind the SARS-2 spike protein and identified one aptamer with high affinity. In preparation for testing this aptamer on the electrochemical device for its ability to recognize the SARS-2 virions, we tested various methods of purifying the virions from the large amount of contaminating membranous and other cellular materials. We have come to what looks like is the most effective separation, which involves a filtration step followed by a sucrose gradient. These conditions will be used to fractionate recently received SARS-2 virions for testing on the sensor with the identified SARS-2 aptamer.

Manuscripts, Reports, and Presentations

Task 1: Establish Alternative Instruments/Reagents and Reachback/Validation

Publications

1. Adikari, SH, Alipio-Lyon, EZ, Hollander, TD, Deshpande, A, Hong-Geller, E. Investigation of pooling strategies using clinical COVID-19 samples for more efficient diagnostic testing. 2020, Accepted, *medRxiv*, <https://connect.medrxiv.org/gr/2020.08.10.20171819>

Submitted manuscripts

2. García, M, Fares-Gusmao, R, Lien, C, Subramaniam, S, Liu, S, Dey, R, Adikari, SH, Lovell, S, Scherf, U, Hong-Geller, E, Wang, T, McGivern, D, Stenzel, T. SARS-CoV-2 reference panel for molecular-based diagnostic devices as an FDA response tool to a public health emergency, 2020, Submitted to *J Molec Diagnostics*.

Reports

3. Omberg, KM, Engelmann, Hutchison, J, Melville, A, Oxford, K, Victry, K. Evaluation of Three Extraction Kits with a 2019-n-CoV Assay, June 2020, PNNL-3008.
4. Final reports on all tasks have been submitted to the Inter-Agency Task Force and are available upon request.

Presentations

5. Sequencing, Finishing and Analysis to the Future (SFAF) Conference, “COVID-19 Diagnostic and Next Generation Lab Testing”, Dec. 2020.
6. LANL Director’s Colloquium, “COVID-19 Diagnostic and Next Generation Lab Testing”, Nov 2020.

Task 2: Develop affinity reagents and novel platform approaches

Publications

7. Provisional patent for the entire suite of 18 antibodies (EIDR S133918).

Reports

8. Manuscript in preparation for publication to Science Immunology.

Task 5: Structure-based protein design for diagnostics

Publications

9. Wilamowski, M, Sherrell, DA, George Minasov G, Kim, Y, Shuvalova, L, Lavens, A, Chard, R, Maltseva, N, Jedrzejczak, R, Rosas-Lemus, M, Nickolaus Saint, N, Foster, IT, Michalska, K, Satchell, KJF, Joachimiak, A. 2'-O Methylation of RNA Cap in SARS-CoV-2 captured by serial crystallography, Proc. Nat. Acad. Sci. USA, 2021, accepted, <https://www.biorxiv.org/content/10.1101/2020.08.14.251421v2>
10. Wilamowski, M, Hammel, M, Leite, W, Zhang, Q, Kim, Y, Weiss, K, Jedrzejczak, R, Rosenberg, DJ, Fan, Y, Bierma, J, Sarker, AH, Tsutakawa, SE, Pingali, SV, O'Neill, HM, Joachimiak, A, Hura, GL. Transient and stabilized complexation of Nsp7, Nsp8 and

Nsp12 in the SARS-CoV-2 replication-transcription complex (RTC), Biophysical Journal, accepted with minor revision

11. Kim Y, Wower J, Maltseva N, Chang C, Jedrzejczak R, Wilamowski M, Kang S, Nicolaescu V, Randall G, Michalska K, Joachimiak A. Tipiracil binds to uridine site and inhibits Nsp15 endoribonuclease NendoU from SARS-CoV-2. *Commun Biol*. 2021 Feb 9;4(1):193. doi: 10.1038/s42003-021-01735-9. PMID: 33564093, <https://www.biorxiv.org/content/10.1101/2020.06.26.173872v1.full.pdf>
12. Osipiuk J, Azizi SA, Dvorkin S, Endres M, Jedrzejczak R, Jones KA, Kang S, Kathayat RS, Kim Y, Lisnyak VG, Maki SL, Nicolaescu V, Taylor CA, Tesar C, Zhang YA, Zhou Z, Randall G, Michalska K, Snyder SA, Dickinson BC, Joachimiak A. Structure of papain-like protease from SARS-CoV-2 and its complexes with non-covalent inhibitors. *Nat Commun*. 2021 Feb 2;12(1):743. doi: 10.1038/s41467-021-21060-3. PMID: 33531496, <https://doi.org/10.1101/2020.08.06.240192>
13. Kneller DW, Phillips G, Weiss KL, Pant S, Zhang Q, O'Neill HM, Coates L, Kovalevsky A. Unusual zwitterionic catalytic site of SARS-CoV-2 main protease revealed by neutron crystallography. *J Biol Chem*. 2020 Dec 11;295(50):17365-17373. doi: 10.1074/jbc.AC120.016154. Epub 2020 Oct 15. PMID: 33060199
14. Kneller DW, Phillips G, Weiss KL, Pant S, Zhang Q, O'Neill HM, Coates L, Kovalevsky A. Unusual zwitterionic catalytic site of SARS-CoV-2 main protease revealed by neutron crystallography. *J Biol Chem*. 2020 Dec 11;295(50):17365-17373. doi: 10.1074/jbc.AC120.016154. Epub 2020 Oct 15. PMID: 33060199
15. Hodge CD, Rosenberg DJ, Grob P, Wilamowski M, Joachimiak A, Hura GL, Hammel M. Rigid monoclonal antibodies improve detection of SARS-CoV-2 nucleocapsid protein. *MAbs*. 2021 Jan-Dec;13(1):1905978. doi: 10.1080/19420862.2021.1905978. PMID: 33843452
16. Kneller DW, Galanie S, Phillips G, O'Neill HM, Coates L, Kovalevsky A. Malleability of the SARS-CoV-2 3CL Mpro Active-Site Cavity Facilitates Binding of Clinical Antivirals. *Structure*. 2020 Dec 1;28(12):1313-1320.e3. doi: 10.1016/j.str.2020.10.007. Epub 2020 Oct 23. PMID: 3315226
17. Kneller DW, Phillips G, O'Neill HM, Tan K, Joachimiak A, Coates L, Kovalevsky A. Room-temperature X-ray crystallography reveals the oxidation and reactivity of cysteine residues in SARS-CoV-2 3CL Mpro: insights into enzyme mechanism and drug design. *IUCrJ*. 2020 Sep 21;7(Pt 6):1028-35. doi: 10.1107/S2052252520012634. Online ahead of print. PMID: 3306379
18. Kneller DW, Phillips G, Kovalevsky A, Coates L. Room-temperature neutron and X-ray data collection of 3CL Mpro from SARS-CoV-2, *Acta Crystallogr F Struct Biol Commun*. 2020 Oct 1;76(Pt 10):483-487. doi: 10.1107/S2053230X20011814. Epub 2020 Sep 15. PMID: 33006576

Submitted manuscripts

19. Jha RK#, Yankey A, Shabazz K, Naranjo L, Velappan N, Bradbury AM, Strauss CEM#. Engineered pH-sensitive protein G / IgG interaction. In Revision in *ACS Chem Biol*. bioRxiv (2020) doi: <https://doi.org/10.1101/2020.12.25.424402>

20. Ngo AV#, Jha RK#. Identifying key determinants and dynamics of SARS-CoV-2/ACE2 tight Interaction. In Review in PLOS ONE. bioRxiv (2020)
doi: <https://doi.org/10.1101/2020.07.13.199562>

Presentations

21. Hura G, Structural Studies of the SARS-CoV-2 RNA Transcription Complex, COVID19 seminar series - Lawrence Berkeley National Lab March 2021
22. Joachimiak A, Progress in Structural Characterization of SARS-CoV-2 Proteins, Critical Assessment of protein Structure Prediction 14, Conference, December 4, 2020
23. Hura G, Diagnostics and Therapeutic efforts of Task 5, Molecular Biophysics and Integrated Bioimaging Seminar Series December 2020
24. Joachimiak A, Structural Studies of SARS-CoV-2 Proteins and their Complexes, Rensselaer Polytechnic institute, November 20, 2020
25. Joachimiak A, Structural Studies of SARS-CoV-2 Proteins and their Complexes, NIH NIAID, SARS-CoV-2 Weekly Investigators Meeting, November 10, 2020
26. Joachimiak A, Structural Studies of SARS-CoV-2 Proteins and their Complexes, Florida Institute of Technology, October 29, 2020
27. Joachimiak A, DOE BERAC “COVID-19 Research Update” on NVBL COVID-19 Task 5 and related research on October 23, 2020
28. Joachimiak A, Crystallography of SARS-CoV-2 Non-structural Proteins, American Crystallographic Association, August 4, 2020
29. Joachimiak A, Task 5 NVBL presentation, Structure-Based Protein Design for Diagnostics, June 30, 2020

Task 6: Next-Generation Rapid Testing (Phase 2 – Next Gen Task 1)

Publications

30. Moehling, T, Choi, G, Dugan, L, Salit, M, Meagher, R. LAMP Diagnostics at the Point-of-Care: Emerging Trends and Perspectives for the Developer Community”, 2020, *Expert Review of Molecular Diagnostics*, 21:1, 43-61, DOI: 10.1080/14737159.2021.1873769
31. Joint invention disclosure has been submitted for the COVID Whistle

Budget Summary

The 2020 CARES Act provided a total of \$6,370k (\$3,920k Phase 1; \$2,450k Phase 2) to nine laboratories in the NVBL. In addition to the nine funded laboratories, NREL was an active participant in the NVBL COVID Testing Team throughout all processes and BNL was active in proposal development and review processes.

Laboratory	Budget
Ames	\$125,000
ANL	\$685,000
LBNL	\$825,000
LLNL	\$730,000
LANL	\$1,340,000
ORNL	\$585,000
PNNL	\$790,000
SNL	\$1,140,000
SLAC	\$150,000
TOTAL	\$6,370,000

